2012

Turbine Base Pressure Active Control Through Trailing Edge Blowing

Bayindir Huseyin Saracoglu
Wright State University

Repository Citation

Saracoglu, Bayindir Huseyin, "Turbine Base Pressure Active Control Through Trailing Edge Blowing" (2012). *Browse all Theses and Dissertations*. 611.
https://corescholar.libraries.wright.edu/etd_all/611

TURBINE BASE PRESSURE ACTIVE CONTROL THROUGH TRAILING EDGE BLOWING

A dissertation submitted in partial fulfillment of the
requirements for the degree of
Doctor of Philosophy

By

BAYINDIR HUSEYIN SARACOGLU
Bs. M.E., Bogazici University
Ms. M.E., Bogazici University
Research Master, von Karman Institute for Fluid Dynamics

2012
Wright State University

WRIGHT STATE UNIVERSITY

GRADUATE SCHOOL

July 23, 2012

I HEREBY RECOMMEND THAT THE DISSERTATION PREPARED UNDER MY SUPERVISION BY Bayindir Huseyin Saracoglu ENTITLED Turbine Base Pressure Active Control through Trailing Edge Blowing BE ACCEPTED IN PARTIAL FULFILLMENT OF THE REQUIREMENTS FOR THE DEGREE OF Doctor of Philosophy.

George P. Huang, Ph.D.
Dissertation Director

Ramana Grandhi, Ph.D.
Director, Ph.D. in Engineering Program

Andrew Hsu, Ph.D.
Dean of Graduate School

Committee on
Final Examination

George P. Huang, Ph.D.

Guillermo Paniagua, Ph.D.

Joseph Shang, Ph.D.

Mitch Wolff, Ph.D.

Paul I. King, Ph.D.

ABSTRACT

Saracoglu, Bayindir Huseyin. Ph.D., Engineering Ph.D Program, Wright State University, 2012. *Turbine Base Pressure Active Control Through Trailing Edge Blowing*.

The desire for high performance and low fuel consumption aero-engines has been pushing the limits of the turbomachinery and leading cutting-edge engine designs to fulfill the demand. The number of stages is reduced to achieve the same pressure ratios over lighter turbines. The extreme expansion requirements result in transonic-supersonic flow fields. Transonic and supersonic turbines are exposed to the shock waves that appear at the trailing edge of the airfoils, generating substantial efficiency deduction due to the interaction with the boundary layer. Furthermore, pressure fluctuations created by the shocks result in unsteady forcing on downstream components and eventually cause high cycle fatigue. Component failure may lead reduced service life and further damage on the engine. A novel proposal to control the resulting fish tail shock waves consists on, pulsating coolant blowing through the trailing edge of the airfoils. The changes in the base region topology and fish tail shock wave were numerically investigated for a wide range of purge flow at simplified blunt and circular trailing edge geometries. An optimum purge rate which increases the base pressure and significantly reduces the trailing edge shock wave intensity was found. The effects of pulsating base pressure on the shock properties and the base region was investigated in detail to understand the mechanisms driving the flow field under unsteady bleed.

A linear cascade representative of modern turbine bladings was specifically designed and constructed. The test matrix comprised four Mach numbers, from subsonic to supersonic regimes (0.8, 0.95, 1.1 and 1.2) together with two engine representative Reynolds numbers (4 and 6 x 10^6) at various blowing rates. The blade loading, the downstream pressure distributions and the unsteady wall temperature measurements allowed understanding the effects on each leg of the shock structure. Minimum shock intensities were achieved using pulsating cooling. A substantial increase in base pressure and significant reduction in trailing edge loss were observed for low coolant blowing rate.

Analysis of the high frequency Schlieren pictures revealed the modulation of the shock waves with the coolant pulsation. The Strouhal number of the vortex shedding was analyzed for all of the conditions. Finally, the statistical analyses of the results showed that the effects of the state of cooling and free stream conditions were statistically significant on the flow properties.

Table of Contents

List of Figures

List of Tables

Nomenclature

a	Speed of sound
A	Nondimensionalized speed of sound
C	Chord length
C_1	Source array
C_2	Source array
C_{pb}	Base pressure coefficient
d	Trailing edge thickess
E	Eccentricity
f	Frequency
F	Flux array
g	Pitch-wise coordinate
I	Shock intensity
k	Turbulent kinetic energy
L	Length scale
m	Mass flow
M	Mach number
N_{holes}	Number of holes on the rotating disk
Nu	Nusselt number
O	Calibration line offset
P	Pressure
r	Refinement ratio for the computational grid
Re	Reynolds Number
S	Curve length, Calibration line slope
N	Number of grid points
St	Strouhal number
t	Time variable
T	Temperature, period of oscillation

u	Flow speed
U	Nondimensionalized flow speed
v	Flow velocity
V	Voltage
W	Field variable array
x	Horizontal space variable
y	Vertical space variable
Y	Shock border in Schlieren pictures
y^+	Dimensionless wall coordinate

Greek

α	Shock angle
α	Mean shock angle
β	Flow angle
γ	Ratio of heat capacities
δ	Trailing edge wedge angle, uncertainty
ε	Suction side curvature, difference
ζ_{pb}	Base pressure loss
Δ	Difference
ρ	Density
ω	Specific dissipation
ω_{disk}	Angular speed of rotating disk
ϕ	Flow variable

Subscripts

0	Stagnation property
1	Inlet plane
2	Outlet plane
b	Base region property
c	Coolant property, geometrical center

f	Free stream property
is	Isentropic
max	Maximum
mer	Mercury thermometer
min	Minimum
pk	Peak value
pk-pk	Peak-to-peak value
ref	Reference value
w	Wall

Superscripts

*	No blowing value, single pitch length
`	RMS variation
in	Inner shock border
out	Outer shock border

Abbreviations

CFD	Computational fluid dynamics
DC	Direct current
Exp	Experimental
FFT	Fast Fourier transforms
LES	Large eddy simulation
PSD	Power spectrum density
RANS	Reynolds averaged Navier-Stokes
RMS	Root mean square
SST	Shear stress transform
TE	Trailing edge
UAV	Unmanned aerial vehicle
URANS	Unsteady Reynolds averaged Navier-Stokes
VSA	Vibration suppression algorithm

Acknowledgements

I would like to thank my co-advisors Prof. Guillermo Paniagua and Prof. George Huang for their endless assistance and guidance in realization of this thesis. It is hard to overstate my gratitude to them. I also appreciate Prof. Joseph Shang, Prof. Mitch Wolff and Prof. Paul I. King for serving in my examination committee.

I would like to thank the students at the von Karman Institute for their personal and technical support throughout this doctoral research, including Dr. Tolga Yasa, Marcos Gonzalez, Dr. Flora Tomasoni, Jaime Sanchez Serrano, Dominick Christoffels, Sergio Lavagnoli, Victor Fernandez, Ceyhun Sahin and Laura Villafane. I would like to acknowledge the collaboration with University of Florence on this project and I would like to extend my gratitude to Prof. Francesco Martelli, Dr. Simone Salvadori, and Dr. Chiara Bernardini for their support. I also appreciate the entire technical and administrative staff of the von Karman Institute and Wright State University, including Pierre Londers, Terence Boeyen, Alysoun Taylor-Hall, Paula Esken, and Carla Vaughn.

I would also like to express my gratitude to my extended family and all friends for always being there for me and supporting me from various time zones on earth, including Prof. Esref Kizilkaya, Prof. Mehmet Saracoglu, Prof. Bekir S. Cebeci, Prof. Selim Nalbant, Prof. Melih Ozel, Prof. Atilla Gungor, Prof. Osman Rodop, Prof. Nadir Yildirim, Prof. Ali Kocailik, Prof. Huseyin Baloglu, Ozan Cetinaslan, Dr. Yavuz Tokmak, Adal Tunga, Levent Ozkan, Dr. Kurtulus B. Oner and Dr. Beni Cukurel. I wish to express my sincere thanks to Prof. Hasan Bedir for keeping the faith on my determination to pursue a career on scientific research since the very first moment I entered his office at Bogazici University and giving me the opportunity to work with him. Finally, I am also grateful to United States Air Force Office of Scientific Research whose financial support has allowed me to work on this frontier research subject.

Last but not least, I would like to thank my family, Tugan, Saynur and Baybars Saracoglu, for their unconditional support and understanding. They are the most caring and loving people to me.

1

Introduction

1.1 Background

The need for high performance and compact aero engines is driving the industry. The internal flow field through the passages of modern turbomachinery suffers harsh conditions. Extreme temperatures, well above the metal melting point, are reached at the combustion chamber outlet. Intensive cooling methods are exploited to preserve the material integrity. Shock waves appear at the trailing edge of transonic turbine airfoils. The shock wave interaction in turbines lead shock induced flow separation and fatigue problems. The performance penalties induced by aforementioned interactions caused by the severe flow conditions are often mitigated by various flow control techniques.

Flow control, in general terms, can be defined as the methods employed to change the global flow pattern without acting in a comparable scale. Those methods can be divided into two main groups: active and passive flow control. Active flow control makes use of flow bleed, steady and unsteady injection, synthetic jets, plasma discharge, moving surfaces etc. to modify the flow field. Whereas, passive flow control techniques include minor geometrical modifications or utilize the pressure gradients inherently existing in the flow field to apply suction or purge.

The geometrical passive control has generally been achieved by placement of dimples on the surfaces and minor modifications on the base line geometries. Otmanns et al. [1] and Hergt et al. [2-4] applied vortex generators on the lateral surfaces of compressor cascades to control the secondary flows and eventually inhibit the corner separation over the blade surface. Santner et al. [5] and Lengani et al. [6] suppressed the boundary layer separation in turbine transition ducts by low profile vortex generator wedges. On the other hand, Carroll et al. [7] tested various surface dimples downstream of a leading edge cooling hole to reduce the unsteadiness of the jet and thus an expected increase in the adiabatic effectiveness. Lake et al. [8] investigated dimples and grooves over a low pressure turbine (LPT) airfoil suction surfaces to prevent separation. Similarly, Bohl and Volino [9] reduced boundary layer separation by using arrays of cylindrical elements with various heights on the suction side of LPT blade. Rodriguez [10] and Gai and Sharma [11] investigated several spanwise protrusion geometries at the trailing edge of airfoils to control vortex shedding and consequently reduce the base drag. Three dimensional trailing edge configurations were observed to increase the base pressure.

Flow suction or purge through ducts and cavities owing to pressure gradient are another practice in passive flow control. Zhou et al. [12] successfully reduced the flow separation by bleeding the pressure side flow to suction side in a compressor cascade. El-Gendi et al. [13] numerically simulated pressure side bleed and suction side purge immediate upstream of a turbine vane trailing edge. The wake unsteadiness was significantly reduced and base pressure was increased by the method. Lin et al. [14] investigated passive control of shock wave/boundary layer interaction through surface cavity suction and blowing derived by shock wave pressure gradient.

Active bleed and injection have been applied over various locations on the cascade surfaces to enhance the flow characteristics. Trailing edge blowing in turbine airfoil has been studied to reduce the losses [15-23]. Substantial base pressure increase along with reduction in the losses was observed for moderate blowing rates. Base bleed was also utilized to modulate the trailing edge vortex shedding [23-25]. Existence and the frequency of the coherent structures were showed to be highly dependent on the ejection rate. Steady blowing near the end wall of compressor cascades diminished the secondary flow losses and suction side separation [26]. Zhou et al. [27] considerably minimized flow separation by simultaneous blowing near the leading edge and suction close to trailing edge of a compressor blade. Vortex generator jets with steady blowing on the suction surface were also used to reduce separation on compressor [28], high pressure

[29] and low pressure turbine cascades [30, 31]. However, the impact of pulsed vortex generators was found superior relative to the steady jets by various studies in the literature [32-37]. Experimental and numerical studies performed on LPT cascades showed that the separation on blades equipped with pulsed vortex generators on the suction side was almost completely disappeared [38-43].

Synthetic jets, as an active control method, have been frequently utilized to prevent the boundary layer separation in compressor and LPT cascades. Synthetic jets create a pulsating discharge with no net mass flow. Low momentum boundary layer flow is sucked during intake phase and injected back to enhance mixing. Several research groups [44-48] studied the synthetic jets located on the casing surfaces of compressor cascades. Performance improvements were observed through weakening the secondary flows and preventing blade suction side separation. The results obtained in LPT blades were analogous. Arrays of synthetic jets, located on the suction surface of high lift blades, mitigated flow separation by periodic suction and blowing to the boundary layer [49-54].

Dielectric plasma discharge (DBD) actuators have recently been implemented to turbomachinery applications for flow control purposes. The induced plasma locally energizes the flow and suppresses separation in both compressors and LPTs [55-58]. Secondary flows effects were also alleviated by end wall attached DBDs [59, 60]. The experiments on LPT blades were pointed 15% reduction in the tip gap losses with plasma actuator mounted at the blade tip [61]. Besides, the trailing edge located DBDs induced wake filling effect and mitigated the trailing edge losses in a LPT cascade [62].

1.2 Objectives of the work

The current manuscript describes the investigation on the control of trailing edge shock waves by altering the base pressure. This technology should play a major role in reducing the detrimental effects of the shock waves in supersonic flows in a wide range of applications. Transonic turbine vanes experience fish tail shocks due to the recompression of the supersonic flow with the wake. Trailing edge shock interaction generates pressure fluctuations that may result in low and high cycle fatigue problems. The current research proposes an unprecedented shock control strategy making use of unsteady trailing edge purge flow. Understanding the trailing edge cooling-shock interactions requires fundamental knowledge of the base flows. Construction of a detailed base pressure correlation in conjunction with the shock wave characterization is of utmost importance to predict the response of the shock system at different levels of cooling rate. Consequently, an optimum purge rate is to be sought for pulsating coolant that reduces the impact of the shocks, while providing enough injection to cool the vane.

The interaction of the periodically oscillating coolant with the base region and subsequently shock waves entails fundamental comprehension on the pulsating flows which can only be achieved by a meticulous experimental survey. Therefore, development of advanced measurement techniques and sophisticated processing tools bear ultimate importance on interpreting the major flow features.

1.3 Methodology of the research

In order to achieve the objectives previously stated, the research was divided into three major activities.

1. The first activity starts with identifying the simplest geometry similar to a turbine trailing edge to analyze the interaction of the continuous cooling with trailing edge attributes. Initially a blunt trailing edge was studied by Reynolds Averaged Navier-Stokes (RANS) simulations to understand the effect of continuous cooling. Pulsating cooling was then simulated over the same geometry by URANS computations. Finally the effects of pulsating cooling over a rounded trailing edge were investigated.
2. Secondly, the activities involved in the design of the experiment were accomplished in four steps. The relevant non-dimensional parameters for the experiments were selected. The test article, which shall show high performance with the range of test conditions, was designed by making use of RANS simulations and the in-house experimental knowhow. Following the selection of pulsating mechanism, the experimental analysis and modeling were completed to characterize the complete pulsating cooling system.

3. In the final stage of activities, the experiments aspiring to study the main flow features of interest, the base pressure, shock strength and vortex shedding, were accomplished. Unsteady characterization of the shock wave orientation was carried out by high speed Schlieren imaging. Finally, the impact of the trailing edge shock wave was quantified through heat transfer measurements.

1.4 Organization of dissertation

The thesis is composed of five chapters. Following this introductory Chapter 1, Chapter 2 reviews the experimental and numerical tools utilized to obtain and analyze the data. The comprehensive description of experimental setup and measurement techniques together with the explanation of the numerical tools used are presented in this section. The data reduction techniques used to process the measurements and CFD results are also in the scope of this chapter.

Chapter 3 provides the outcomes of the steady and unsteady numerical simulations performed on simplified blunt and circular trailing edge geometries exposed to supersonic flows. The changes in downstream flow features (base pressure, shock properties and vortex shedding) were tabulated for steady and unsteady coolant blowing. The relationship between the trailing edge purge and the shock wave attributes are explained to find the optimum cooling parameters.

Chapter 4 describes the experimental and numerical results obtained over a linear cascade test section with steady and unsteady coolant ejection exposed to a range of Mach and Reynolds numbers. The airfoil loadings together with downstream pressure distributions were extracted for all test conditions to identify the changes on the strength of trailing edge shocks by cooling. The unsteady change in shock wave orientation was quantified from the Schlieren images. A base pressure and Strouhal number correlations are provided to characterize the steady and unsteady features of the base flows affected from the coolant blowing.

Chapter 5 finally outlines the results and states the main conclusion of the research.

2

Experimental and Numerical Tools

2.1 Isentropic compression tube test rig

2.1.1 Description of the facility

An isentropic compression tube facility at the von Karman Institute has been used to perform all experiments in this work (Fig. 2.1). Optical access permitted Schlieren and oil flow visualizations. The facility provides 100 to 800 ms of testing time [63-65]. The test duration varies exponentially with the test Reynolds number (Fig. 2.2).

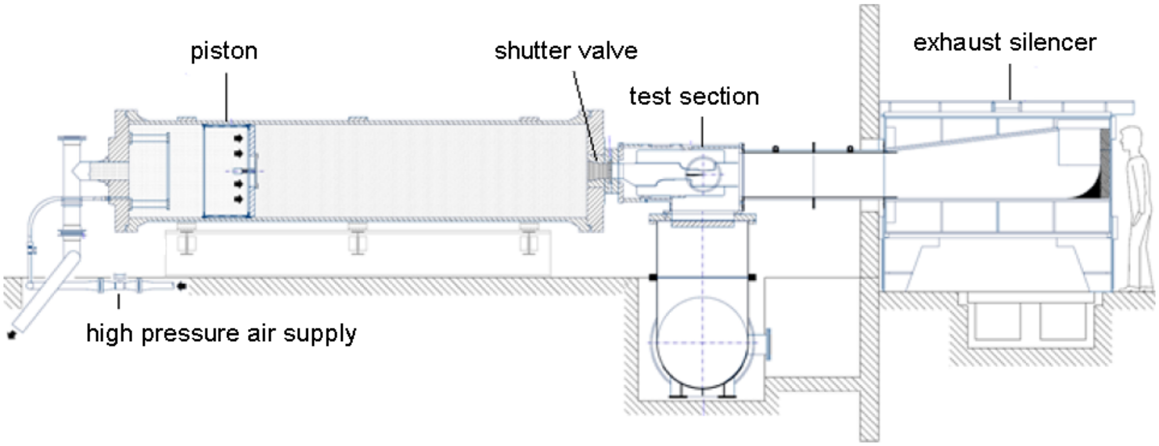

Fig. 2.1. The schematic of the experimental facility

The air inside the cylindrical vessel is compressed by a free piston driven by high pressure dry air (300 bars) until the desired upstream conditions are attained.

Subsequently, a shutter valve releases the air into the test section. The flow is vented axially to the atmosphere.

The test section accommodates two flow passages separated by an airfoil. The model and two contoured end-wall sections are staggered at 66 degrees. Transonic flow adaptation is achieved by a sudden expansion downstream of the trailing edge.

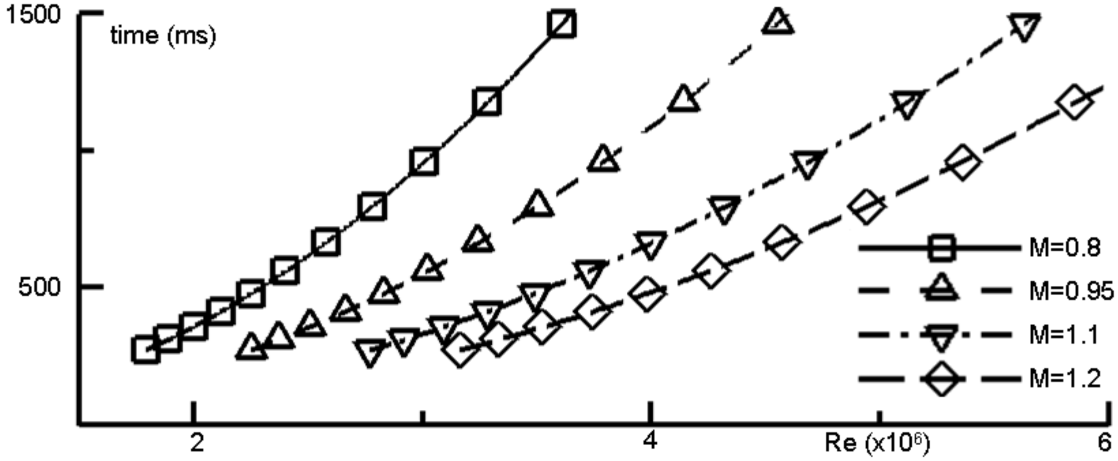

Fig. 2.2. Testing time changing for different test conditions (Reynolds and Mach number)

2.1.2 Similarity parameters to design the experiments

Achieving the similarity between the investigated flow field and the experimental-numerical simulations is crucial to attain valid conclusions. At subsonic, transonic, and low supersonic velocities, for the same test model, the dynamic similarity of the flow field is determined by two similarity parameters: Reynolds and Mach numbers.

In state of the art turbomachinery, single stage high pressure turbine nozzle guide vanes experience supersonic-transonic flows with Mach and Reynolds numbers (based on blade chord length) varying between 0.9 – 1.5 and 1 $x10^6$-10 $x10^6$, respectively, depending on the type and the application of the engine. Therefore, the experimental and numerical test campaigns were designed to match Mach and Reynolds numbers. Four Mach numbers (0.8, 0.95, 1.1 and 1.2) were tested along with two Reynolds numbers ($4x10^6$ and $6x10^6$). High pressure stages of the gas turbines are cooled by high pressure air extracted from the compressor where the pressure is at a comparable level with the high pressure turbine stage. In order to understand the aerodynamic interactions between the coolant stream and the main flow, their total pressure ratios should be considered as a similarity parameter. The range of coolant to inlet total pressures ratios changing between 0.5-1.25 were obtained during the experimental and numerical simulations.

2.2 Test section and blade model design

The airfoil model reproduces the velocity distribution encountered in a modern cooled turbine airfoil. The trailing edge diameter was maximized to increase the spatial and temporal resolution of the vortex shedding phenomena in the Schlieren flow visualizations. The rear part of the suction side was identical to the airfoil documented by Sieverding et al. [17], as shown in Fig. 2.3. The rest of the profile was fitted by high-order Bézier curves to ensure the continuity of the curvature and passage width, resulting in a smooth velocity evolution. The chord length of the final model geometry was 192 mm and span (the width of the test section) was 100mm.

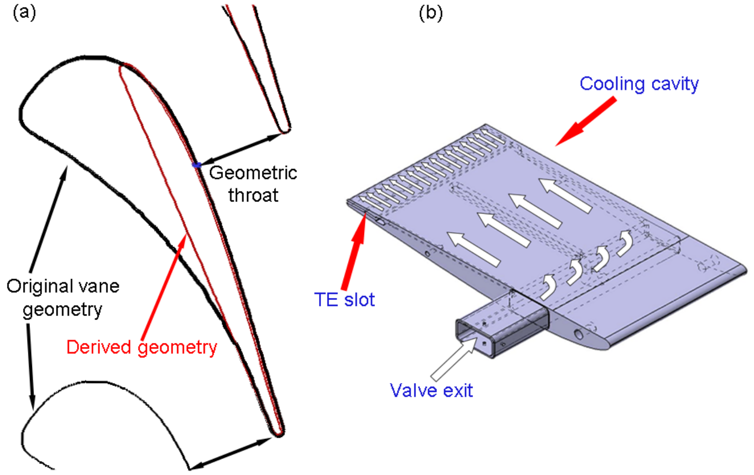

Fig. 2.3. a)The construction of the airfoil geometry b) Internally cooled airfoil

The aerodynamic performance of the cascade passage was tested for various downstream isentropic Mach numbers, ranging from 0.8 to 1.2. The flow field around the airfoil leading edge was investigated in detail to analyze incidence effects. No sign of separation was observed for the incidence angles of ±2 degrees.

The blade was manufactured by using selective laser sintering to have the cooling channel and the complex network of pneumatic pressure pipes and cabling lines in a single piece model with high precision.

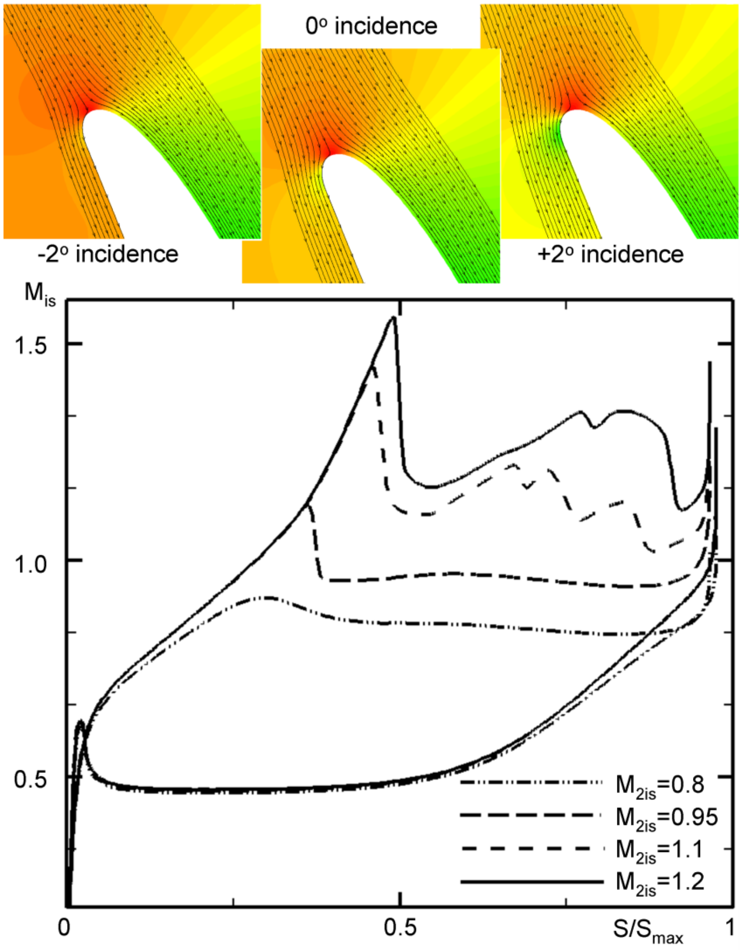

Fig. 2.4. The airfoil analysis for various incidences and flow conditions.

2.3 Unsteady cooling system

Pulsation in the coolant stream was provided by a perforated rotating disc. When the holes on the disc are facing the inlet and outlet ducts a flow pulse is generated. Detailed characterization of the rotating valve cooling system was performed upstream and downstream of the airfoil [66].

2.3.1 Experimental setup

A drawing of the blade model geometry is presented in Fig. 2.3-b. The cooling channel is carved inside, starting from a lateral inlet up to a 1.5 mm slot at the trailing edge. As stated before, the main interest here is to study the performance of a turbine blade with pulsating coolant stream ejected through the trailing edge. This investigation consequently requires a pulsating source to supply the coolant stream. A pulsating valve is proposed to fulfill such requirement. The pulsating valve is a device capable of creating a pulsating mass flow from a continuous one. The device works in such a way that a perforated disk attached to an engine rotates between two lids, each of which is connected to a pipe, an inlet upstream of the disk supplies compressed air and an outlet after it delivers the pulsating stream. The holes drilled in the disk connect inlet and outlet pipes periodically and create the pulses. The frequency of the pulsation depends on the number of holes and the rotational speed of the disk, according to Eq. (2.1). The main elements and pictures of the valve are presented in Fig. 2.5.

$$f_c = \frac{\omega_{disk}}{60} \times N_{holes} \tag{2.1}$$

where ω_{disk} is the rotational speed of the disk in rpm and N_{holes} is the number of holes perforated on the disk. In this case a disk with 4 holes and an engine rotating up to 3000 rpm is being used, i.e. 200 Hz pulsation frequency. In order to test the ability of the valve to produce pulsating flow, a campaign of measurements was carried out. The valve was separately examined, simply connecting its inlet to a source of compressed air and keeping its outlet open. This kind of setup allows measuring directly the jet ejected to the atmosphere. One of the most important limitations when measuring pulsating flow is the frequency response of the instrumentation. For the frequency ranges considered here (around 200 Hz), hot-wires provide sufficient band-width but they lack the ability to detect backflow, a phenomenon that could occur in this case due to the unsteady nature of the problem. On the other hand, pneumatic pressure probes could not reach the required frequency range, depending on the selected configuration. Furthermore, due to the non-linear relationship between pressure and flow rate they will likely lead to non-negligible errors even for the average value of a pulsating flow [67]. To avoid this pitfall, pressure measurements at all locations were also recorded with high-frequency response probes, based on piezo-resistive technology.

Finally, for the study of the complete trailing edge pulsating flow system, the blade model was attached to the valve outlet. For this purpose, an adaptor was designed to procure a smooth transition between the circular shape of the valve outlet pipe and the rectangular inlet of the blade's cooling channel. A picture of the adaptor together with the blade model is presented on the top right part of Fig. 2.5. Due to the small height of the coolant channel at the trailing edge, only hot-wire was considered well suited at this location. An L-shaped hot-wire probe was used, to ensure minimum flow obstruction and avoid vibration when the probe is exposed to pulsating flow.

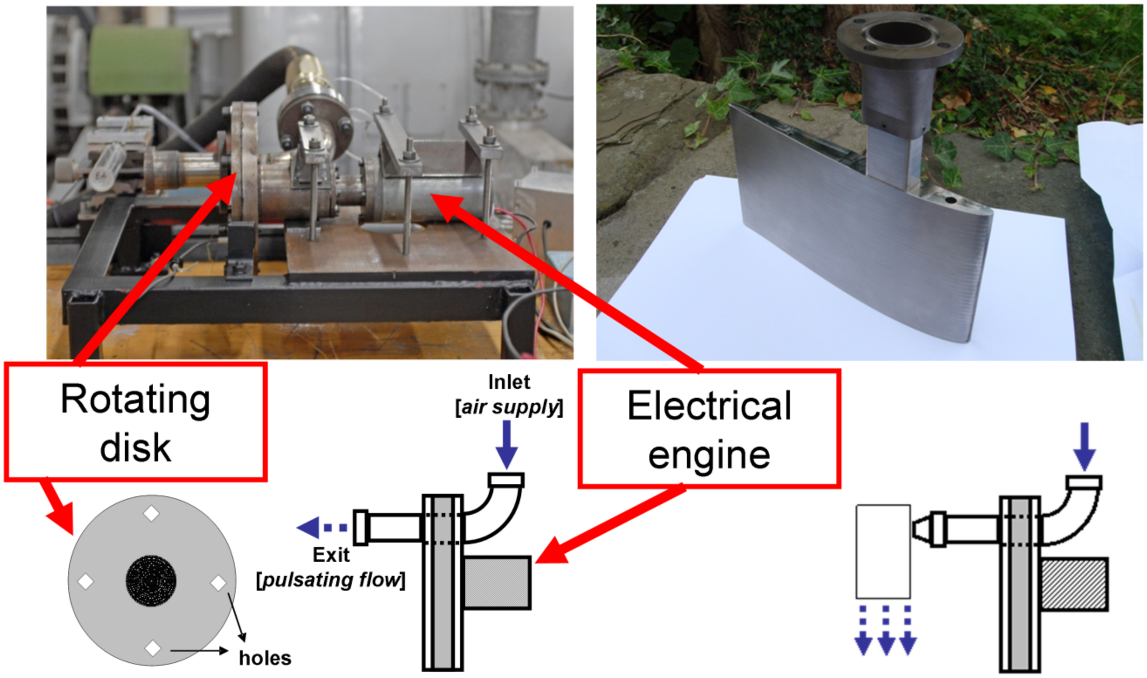

Fig. 2.5. Pictures and schematic view of the pulsating valve.

2.3.2 System modeling

Taking advantage of the extensive set of experimental data obtained to characterize the pulsating device and the complete trailing edge pulsating system allowed to propose and validate simple models for each component and for the complete system. Validated models permit to gain a better understanding of the investigated phenomena, extending the experimental conditions beyond the practical and physical limits imposed by the testing itself and at a fraction of its cost. A one-dimensional unsteady gas-dynamic model was used to calculate the flow in the pipes and inside the blade cavity. This code was developed to allow internal combustion engine research, subjected to the same unsteady pulsating conditions considered for the present application. The one-dimensional assumption is valid when the length to diameter (L=D) ratio of the pipe is large enough to consider fully developed flow. If the viscosity is neglected, the one dimensional governing equations for unsteady flow form a nonhomoentropic hyperbolic system, according to Eq. (2.2).

$$\frac{\partial W}{\partial t}+\frac{\partial F}{\partial t}+C=0 \tag{2.2}$$

where W is the array of field variable, F is the flux array, C is the source array, x is the spatial coordinate and t is the time. The system of equations is formed with mass, momentum and energy conservation. The model assumes that the boundaries behave like a quasi steady manner, and respond instantaneously to changes in incident conditions. The duct ends are solved, as proposed by Benson [68] using the method of characteristics. The method of characteristics uses the following Riemman invariants to solve the properties of the gas at the end of the ducts.

$$\lambda_{inlet}=A-\frac{\gamma-1}{2}\cdot U \quad \lambda_{outlet}=A+\frac{\gamma-1}{2}\cdot U \tag{2.3}$$

where A = a/a_{ref} and U = u/a_{ref}. When nonhomentropic flow is considered, an energy equation in addition to the wave characteristics given by Eq. (2.3) is required. This extra equation introduces an additional characteristic, called path line, as follows:

$$\frac{P}{P_{ref}}=\left(\frac{A}{a_A/a_{ref}}\right)^{\frac{2\gamma}{\gamma-1}} \tag{2.4}$$

Finally, Eq. (2.2) is solved using finite-difference schemes. Further details about the model can be found in Galindo et al. [69]. The modeling of the cooling system has been divided in different subsystems. The ultimate intent is to simulate the complete experimental setup, including piping; pulsating valve and blade cavity (see Fig. 2.6 for a detailed list of the elements and parameters considered). This model will be used to extend the experimental investigation beyond the limits of the current setup, mainly the upper frequency provided by the valve.

A validation model is required to tune valve and blade ejection losses, which depend on the actual characteristics of the setup and cannot be known a priori. A different approach was needed to model of the blade cavity due to the lack of experimental results at its inlet. In this case, the tuning was carried out in the frequency domain. The procedure consists of using two different pressure input signals, a step and a sinusoidal, and recording the responses of the model. With the first one the frequency response of the cavity (or its transfer function) is directly calculated first by numerical derivation of the temporal signals to transform the step into an impulse and then, moving to the frequency domain by applying the FFT of both input and output signals and dividing them. With the sinusoidal input a discharge coefficient for the trailing edge is adjusted, until the gain of the model calculated for the sinusoidal input and the respective gain calculated from the transfer function are equal. This process is detailed in Fig. 2.7. Fig. 2.7-a and Fig. 2.7-b show the input step and impulse, obtained by numerical derivation, used to calculate the transfer function, together with the corresponding model responses. The magnitude of the transfer function calculated is shown in Fig. 2.7-c.

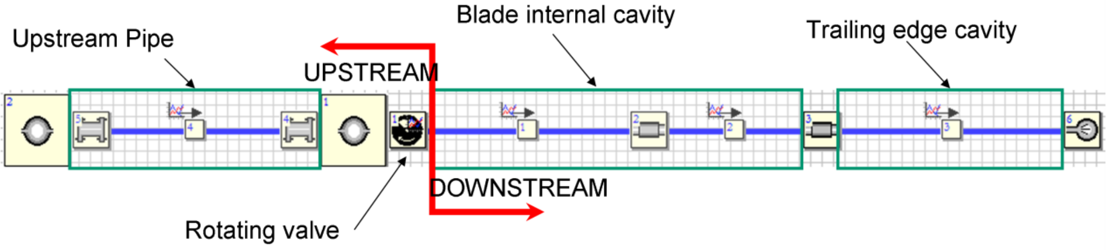

Fig. 2.6. Model used to study the complete trailing edge pulsating system.

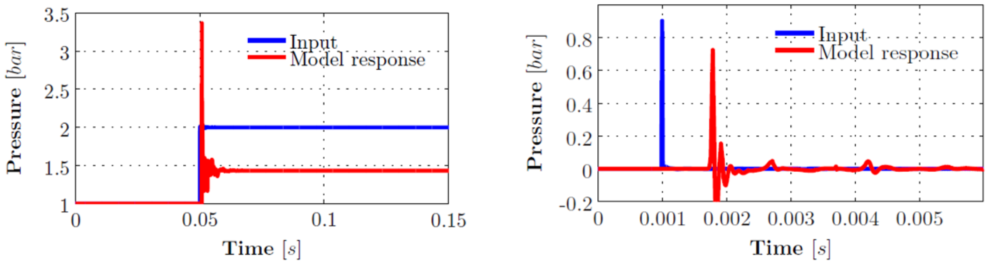

(a) Step test signals

(b) Impulse and response derivated from step test

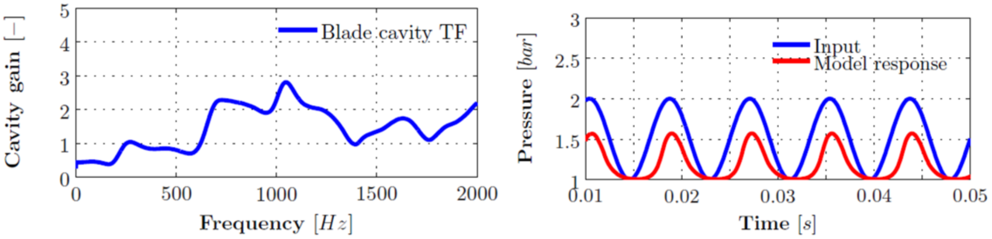

(c) Blade cavity transfer function magnitude

(d) Sample of sinusoidal signal used to tune the models

Fig. 2.7. Procedure to obtain the transfer function of the blade cavity.

Finally, Fig. 2.7-d shows one sample sinusoidal signal and the corresponding response after the tuning process. It is worth noting from the transfer function that no attenuation can be directly related to the blade cavity itself at frequencies higher than 600 Hz.

2.3.3 Characteristics of the rotating valve

A comprehensive characterization of the device selected to create pulsating flow was conducted. It was first analyzed in a separated setup to test its own performance and then connected to the blade model, in order to provide information about the complete trailing edge pulsating flow system.

The setup proposed for the pulsating flow experiments provides control over the frequency and amplitude of the pulses generated by changing the rotational speed of the valve and the upstream total pressure independently. The rotational speed can vary between 0 and 3000 rpm simply increasing the voltage of the DC power supply from 0 to 24 V. This simple method was found appropriate for the valve characterization because it produces low electric noise compared to more sophisticated electronic motor control circuits. This kind of systems relies on high frequency semiconductors and generally become significant sources of noise, which might deteriorate the quality of the measurements. Voltage motor control has, however, an important disadvantage: it does not provide feedback control of the velocity and hence it is not able to detect or compensate the effects of external perturbations. Even the change in the upstream total pressure is a perturbation (the higher the pressure the stronger the fluid pushes the disk in the axial direction), it has been proved that it does not act as a source of perturbation for the pressure range used during the experiments.

The upstream total pressure determines the amplitude of the pulses. Its value can be modified by connecting to a compressed air source which is manually operated by a butterfly valve.

2.3.4 Experimental results – Pulsating valve characterization

For the pulsating valve characterization, the combinations of rotational speed and upstream pressure were selected. Four different rotational speeds and ten upstream pressures were used. Four samples of the mass flow obtained at increasing rotational speed and upstream total pressure are presented in Fig. 2.8.

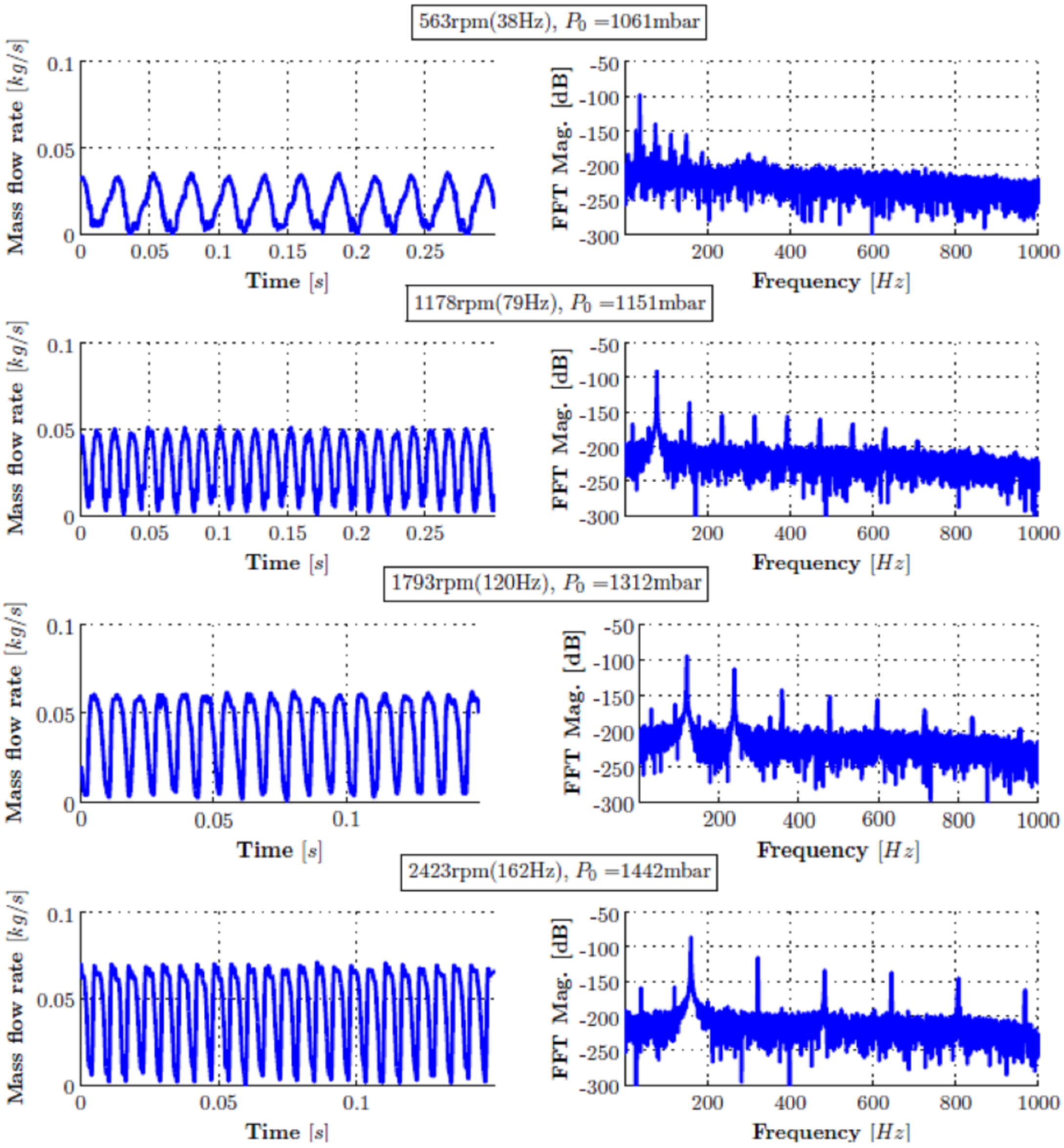

Fig. 2.8. Pulsating valve mass flow experimentally obtained at different conditions.

These plots reveal a clear pulsating jet at valve outlet, the amplitude of the pulses increasing with increasing upstream total pressure (P_0). The shape of the signals corresponds to the diamond-shaped holes passing in front of the circular inlet and outlet pipes, yielding a sharp triangular waveform. Mass flow spectra clearly show a fundamental frequency corresponding to the hole passing frequency and its harmonics but in most plots lower frequencies are also observable. These frequency content is noticeable with different magnitudes at 1/4, 1/2 and 3/4 of the fundamental frequency.

To get a better understanding of the influence of rotational speed and upstream total pressure, peak-to-peak mass flow values are shown in Fig. 2.9. The plot contains an average of each value for at least 125 periods, taking into account that the sampling time was 3.27 seconds for all measurements and the maximum period (and hence minimum frequency) was around 25 ms as a result of 600 rpm. Peak-to-peak values were computed subtracting maxima and minima. They show an increasing trend, even when the curves do not fall in one line, differences are not significant taking into account the averaging process used to obtain this plot.

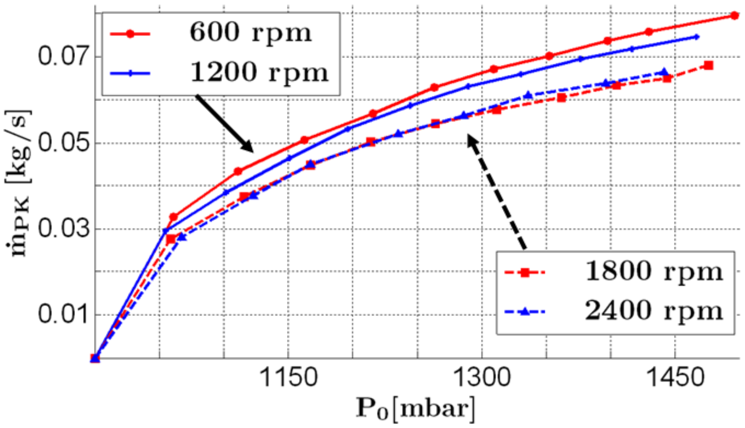

Fig. 2.9. Peak to peak mass flow at valve outlet vs. upstream total pressure.

Owing to the rpm counter, it was easy to explain the origin of fractional frequencies, which were related to mechanical imperfections in the machining of the holes. Little differences in the shape or size of the holes and misalignment of the disk create a unique fingerprint for each hole, generating a periodic disturbance at their passing frequencies, one fourth, one half and three quarters of the fundamental one. The signal provided by the rpm counter yields a high voltage level when a hole is facing the sensor (which is a ferromagnetic detector) and a low level when the sensor sees the metallic disk. Counting the number of pulses during a determined period of time gives the hole passing frequency and the rotational speed of the engine. Fig. 2.10 shows an example, comparing the jet mass flow and the corresponding rpm signal. A theoretical square wave, which would be the one provided by the sensor if a perfectly machined disk could be used, is also presented. Even though both signals seem quite similar in a time plot their frequency content reveals important differences. The presence of such mechanical imperfections affect the flow and it is also distinguishable in the mass flow FFT plots.

2.3.4 Experimental results – Blade model trailing edge ejection

The outlet of the pulsating generator was connected to the coolant channel of the blade for the wind tunnel tests. The coolant channel geometry is limited by its trailing edge thickness, which has been scaled up to the maximum to ensure an adequate spatial and temporal resolution. As it was mentioned before, this value was found to be 1.5mm, the greatest which fitted inside the wind tunnel maintaining similarity with the representative turbine airfoil.

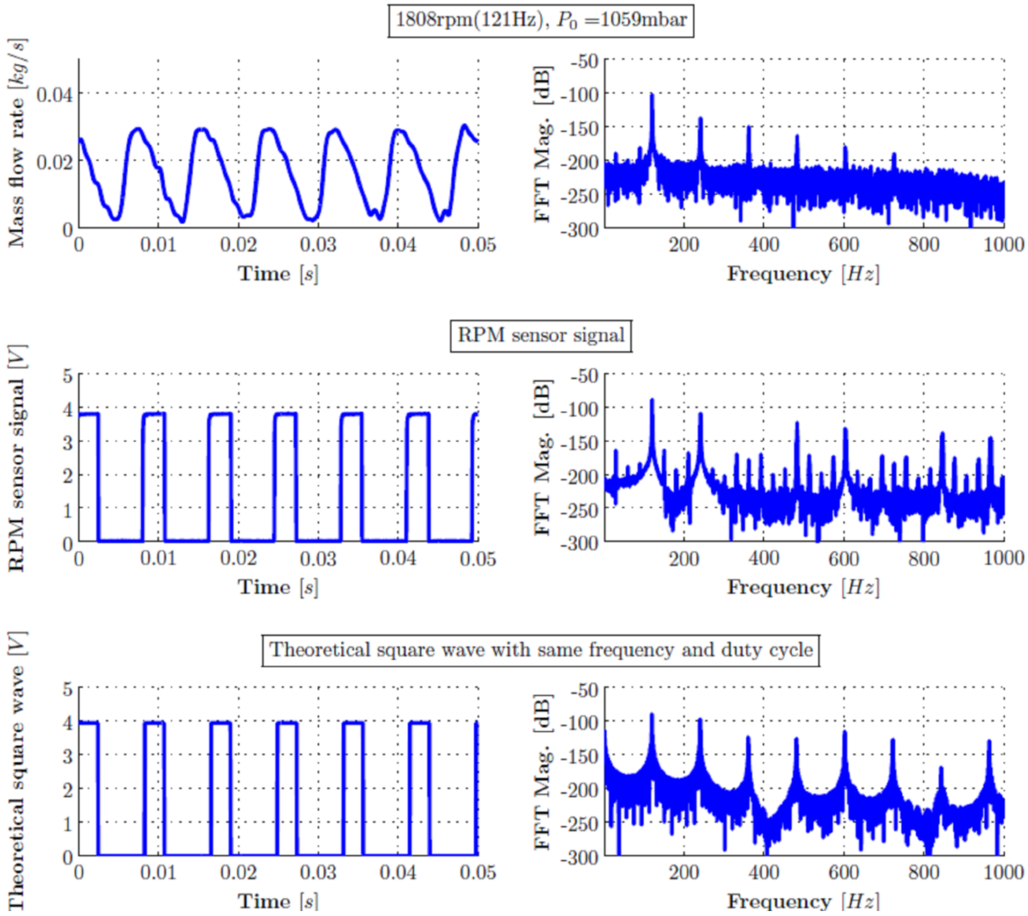

Fig. 2.10. Temporal and frequency analysis of mass flow and disk rotation signals.

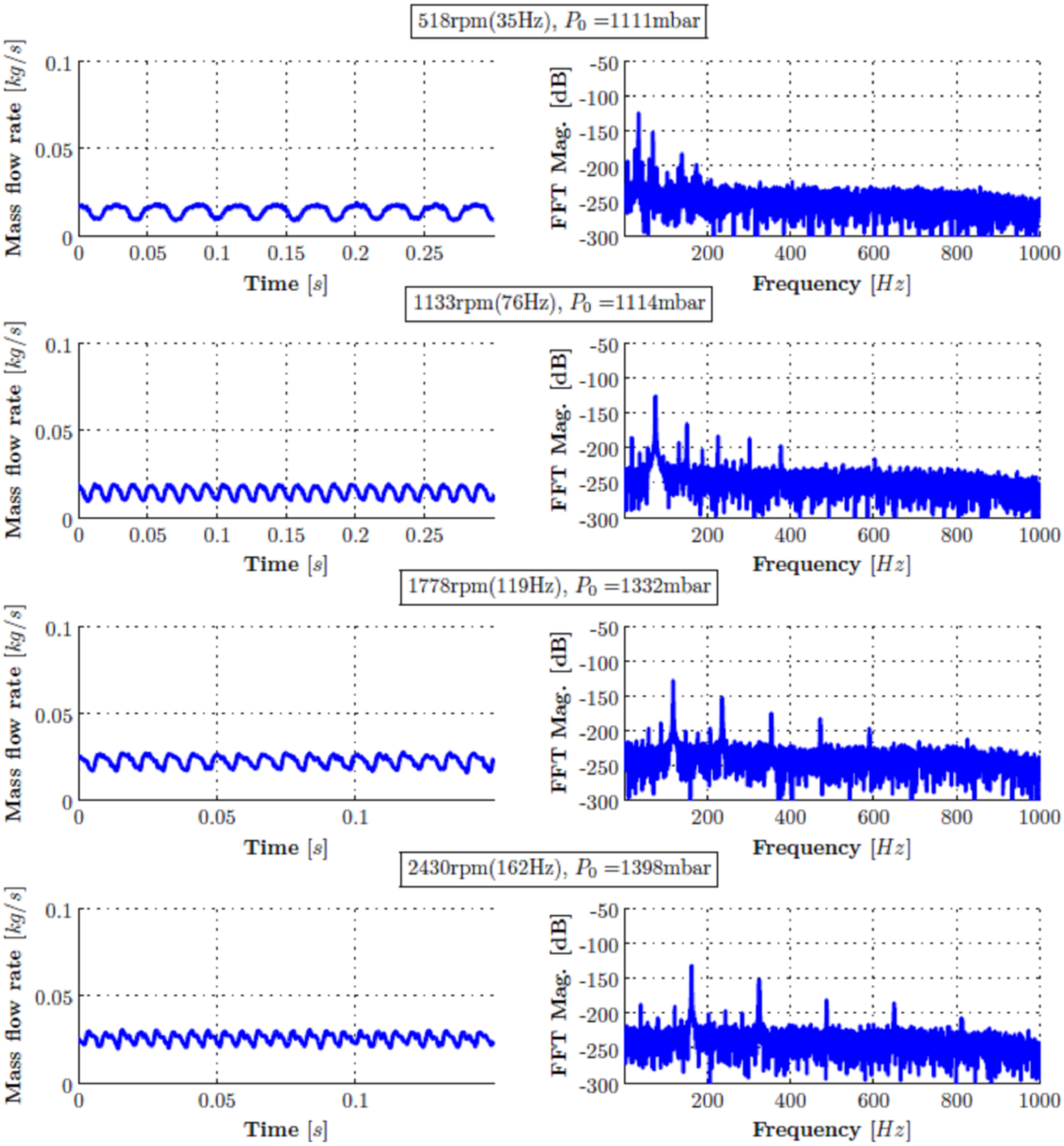

Fig. 2.11. Blade ejection mass flow experimentally obtained at different conditions.

An investigation of the trailing edge pulsating flow was therefore convenient before proceeding to the wind tunnel tests, where the coolant flow will be ejected into the main stream making more difficult the access to the trailing edge region with hot-wires or any other intrusive measurement techniques. Outside the wind tunnel, on the contrary, it was easy to obtain detailed velocity measurements. Due to the small dimensions of the trailing edge only hot-wire was considered to be sufficiently non-intrusive. To ensure that the ejected flow was little disturbed by the presence of the probe, an L-shaped single wire was used. With this arrangement the probe stem was completely out of the flow, only the prongs and wire were exposed.

Results for similar conditions to the ones used before for the pulsating valve characterization are presented in Fig. 2.11. As predicted with the modeled transfer function, the smaller dimensions of the coolant channel had a great impact on the shape of the pulsating flow for the frequencies considered in the experiments, creating a smoothening effect which reduces their amplitude. Note how higher frequency harmonics (over 600 Hz) were, in fact, amplified, resulting in noisy signals.

A comprehensive summary of the peak-to-peak values obtained is presented in Fig. 2.12. It is interesting to remark that the lowest rotational speeds were the only ones providing an increasing peak-to-peak mass flow value with increasing upstream total pressure. The blade ejection results present an increasing trend for the maximum values, separated in two groups, the smaller values of maximum mass flow corresponding to the higher rotational speeds (Fig. 2.13).

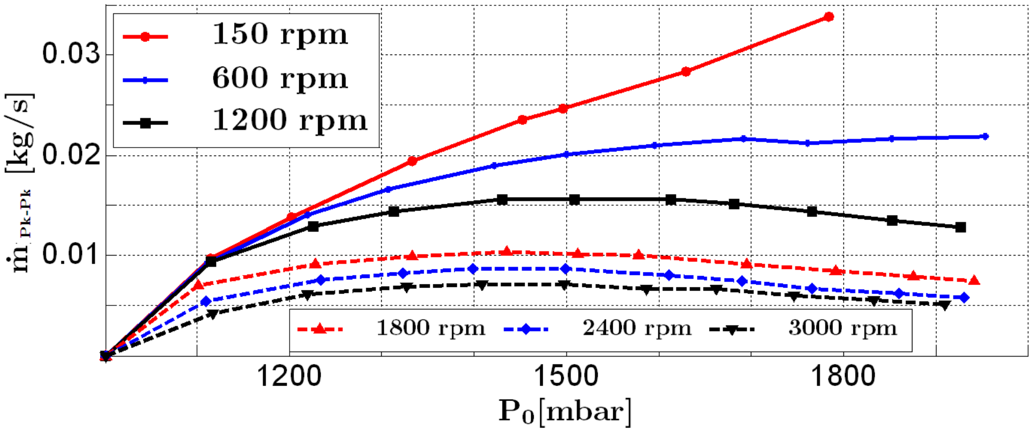

Fig. 2.12. Peak-to-peak mass flow at blade trailing edge outlet vs. upstream total pressure

This phenomenon was thought to be related to different sources. First, it was attributed to the filtering process. After the signals were acquired, a low-pass filter was applied to remove noise. If the cut-off frequency of the filter was fixed the filtered signal contained a limited number of harmonics, which depended on the fundamental frequency of each signal. In this case, fundamental frequencies changed from less than 20Hz up to 200Hz, and consequently for a cut-off frequency of 1kHz, the number of harmonics captured changed from 5 up to 50. To avoid such inconvenience, a dynamic filter was implemented. This kind of filter first calculates the fundamental frequency of the signal and then defines the cut-off frequency accordingly, allowing a fixed number of harmonics to be represented. After using the dynamic filtering, no significant change was observed in the location of the maxima. It was also realized how the uncertainty of the measurements played an important role in achieving accurate distributions of the mass flow characteristics. But the uncertainty analysis carried out revealed no major contributions to explain differences among low and high rotational speeds. The way in which the plots were created was also a source of uncertainty since all signals record a fixed period of time and hence the number of points used to compute the average maxima and minima depends on the frequency, being higher for higher frequencies. After changing the averaging routine, however, no change was detected.

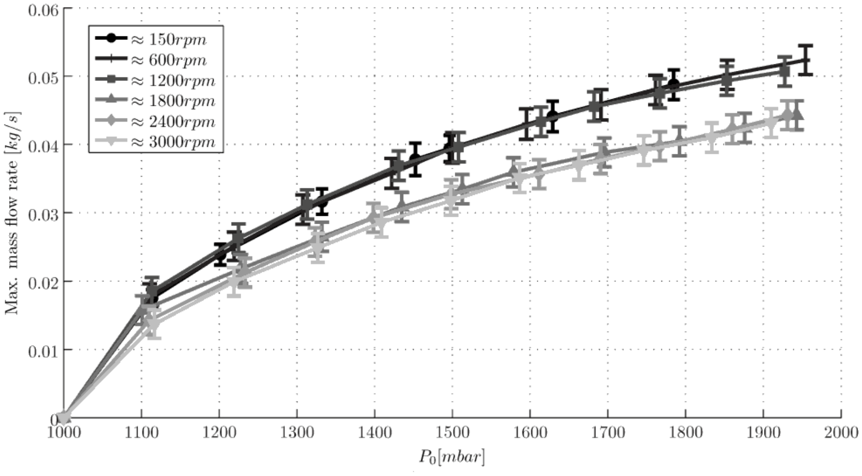

Fig. 2.13. Maximum mass flow at blade trailing edge outlet vs. upstream total pressure. Error bars represent repeatability estimations based on ensemble average.

At this point, it was decided to use phase-locked averaging (PLA) to investigate the periodicity of the mass flow waves. PLA or ensemble average took advantage of the availability of an accurate record of the angular position of the disk at any moment provided by the rpm counter to compute an average period using a determined number of periods from the original signals. After applying PLA the signals were reduced to just one period (either a complete disk rotation or a hole-passing event) which was used to compute maximum, minimum, average and peak-to-peak values. Using one complete disk rotation as a period led to a high level of periodicity. Fig. 2.14, for instance, presents the original mass flow signal for one case compared to the ensemble average of eight disk rotations. In the bottom plot the original signal has been split in 8 rotations and superimposed to the ensemble average period calculated with those rotations. If the sections of the signal to be used for the ensemble average were plotted, like in this case, for a fixed time, a direct estimation of the degree of repeatability is obtained. With the complete set of results after the averaging procedure it was possible to obtain new plots. Maxima and mean values were presented in Fig. 2.13, including error bars indicating the resulting repeatability calculated for eight disk rotations. From this plot, it is clear that even considering repeatability, there is still difference between high and low velocities.

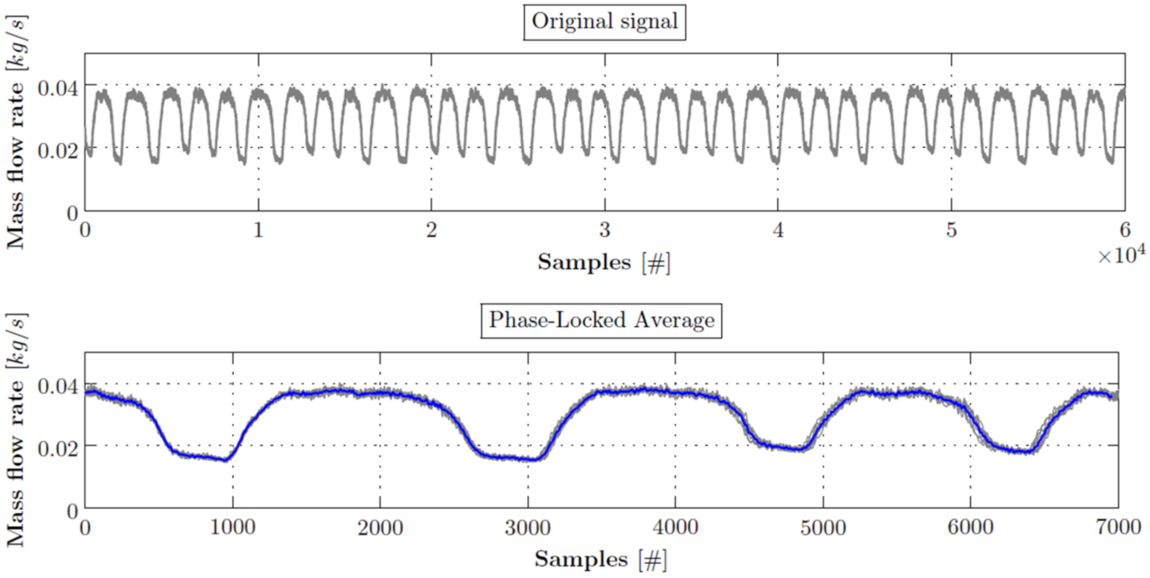

Fig. 2.14. Mass flow sample signal and superimposition of 8 rotations and PLA based on those rotations

2.3.4 Flow modeling of pulsating valve blade assembly

The pulsating valve model was tuned by means of the extensive set of experimental data recorded. The tuning process relied on adjusting the value of the discharge coefficient of the valve. Fig. 2.15 compares experimental data and results from the adjusted model, in terms of velocity at outlet and total pressure at inlet.

For the modeling of the complete trailing edge pulsating system, the coefficients previously found for the individual models of valve and blade were first tried. The blade presented no major problems in the complete system. The valve coefficient, on the contrary, had to be readjusted to fit the experimental data. This fact was obviously due to the change in pressure downstream of the valve. When the flow was not constricted by the blade coolant cavity, the downstream section of the valve was subjected to atmospheric conditions. The blade coolant cavity increases the pressure directly downstream of the valve, affecting its performance, particularly regarding leakage. The discharge coefficient needs to be adjusted to take into account these new working conditions. After the tuning process, modeled data fitted quite well with the experiments, as shown in Fig. 2.16.

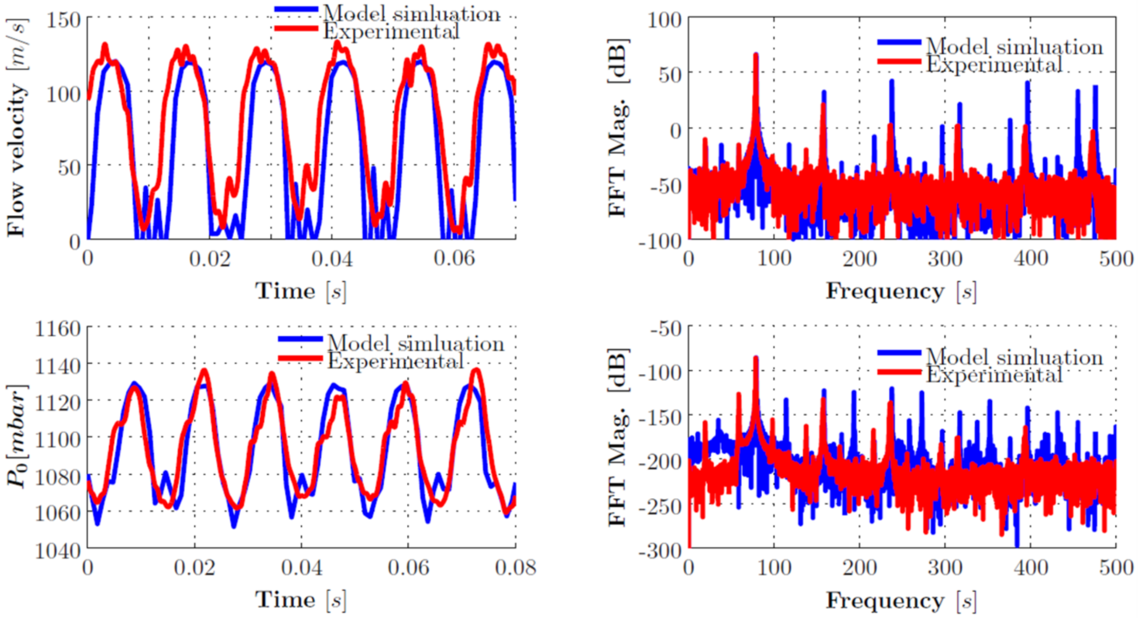

Fig. 2.15. Measured and modeled values of the pulsating valve, flow velocity at outlet (top) and total pressure at inlet (bottom).

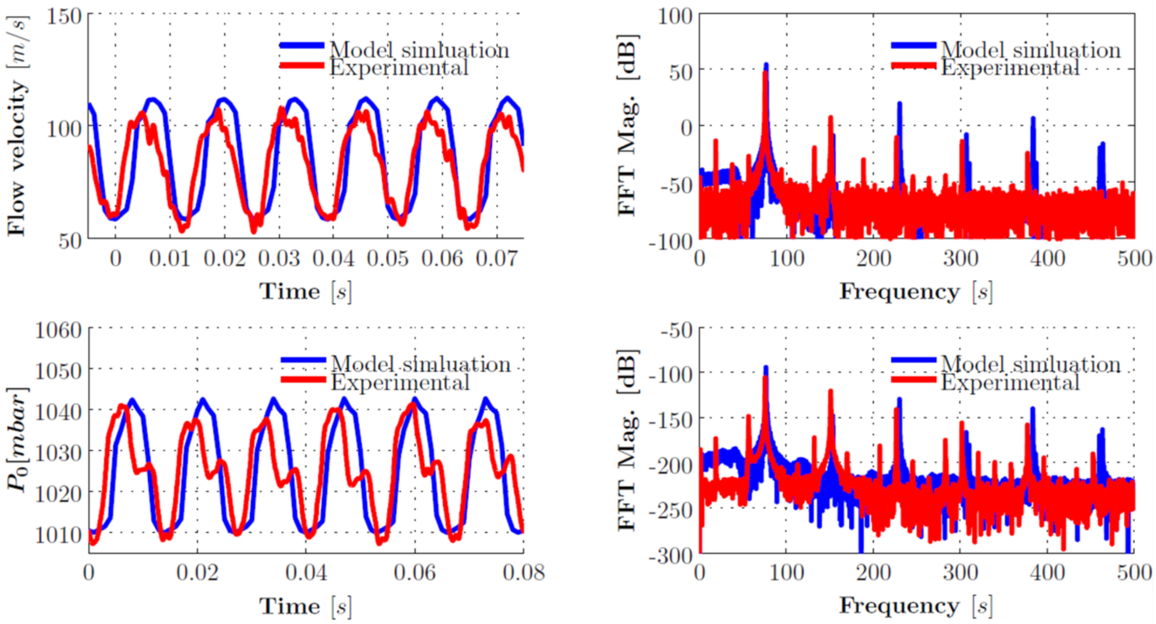

Fig. 2.16. Measured and modeled values of the complete trailing edge pulsating system, flow velocity at the trailing edge (top) and total pressure upstream of the pulsating generator (bottom).

2.4 Measurement techniques

2.4.1 Steady and unsteady pressure measurements

Measurements were performed at several locations along the test section. The inlet total pressure was measured with a Pitot probe located one chord upstream of the airfoil leading edge. The probe head was at 30% of the inlet channel height.

The model and the adjacent suction and pressure sides are equipped with pneumatic lines at mid-span. The first passage (in Fig. 2.17-b) contains 13 taps on the lower wall (pressure side) as well as 13 taps on the model suction side. Similarly, the second passage has 6 taps on the airfoil (pressure side) and 14 taps on the upper wall (suction side). Additionally, 5 piezoresistive sensors are installed on the model. The trailing edge was instrumented with two piezoresistive sensors and two pneumatic lines located at each side of the cooling slot.

The outlet pitch-wise pressure distribution was monitored by a row of pneumatic taps located at 25% of the chord downstream of the trailing edge plane, consisting of 12 taps over 80% of the pitch. All pneumatic lines were sampled with 1.1 bar ScaniValve sensors at a sampling rate of 300 Hz, whereas the piezoresistive sensors were recorded at 500 kHz. The measurements were averaged for a constant time interval when the stable operating conditions were achieved to attain the time-averaged quantities. Fig. 2.17-a displays the Mach number evolution in a typical experiment.

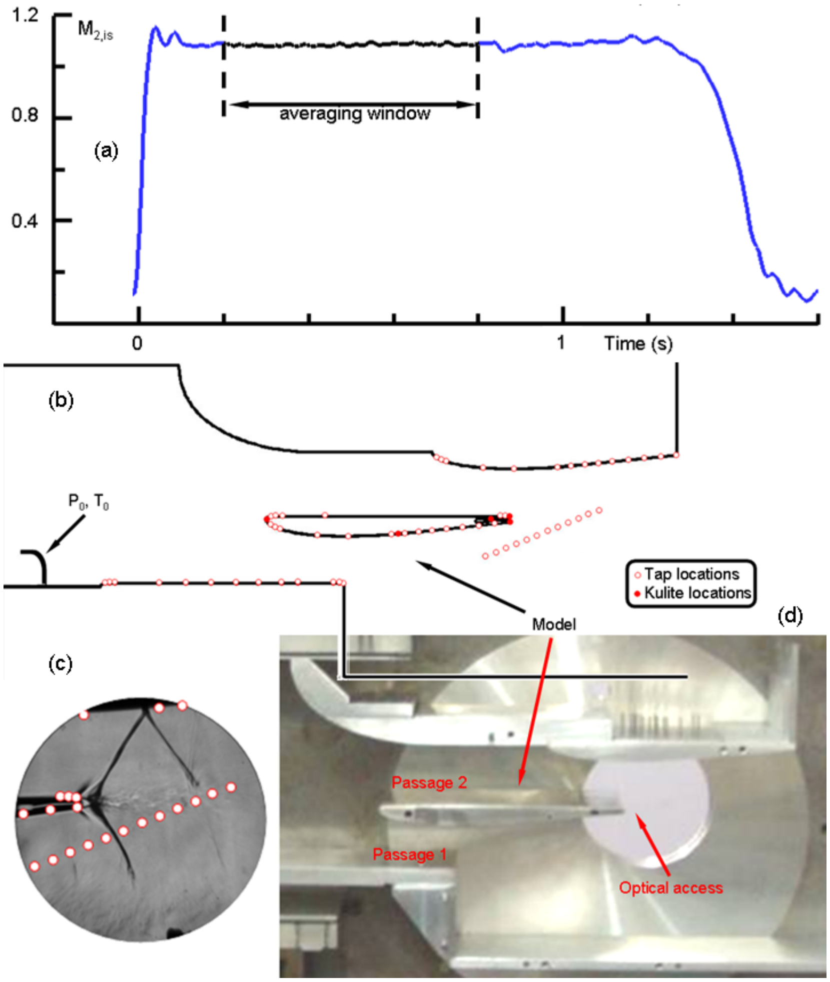

Fig. 2.17. a) Variation of downstream isentropic Mach number during a test; b) Schematic view of the test section with pressure measurement locations; c) Schlieren picture together with pressure sensor taps; d) Manufactured test set-up

2.4.2 Thermal measurement

Inlet fluctuations on the incoming stream were measured at one chord upstream of the cascade by a micro thermocouple with 25 μm junction thickness. Steady and unsteady surface temperature measurements were performed on the suction side contoured top wall of the test section to assess the disturbances on the boundary layer by using 11 nickel based thin film sensors fabricated by Tao Systems. The entire unsteady data acquisition was done at sampling frequency of 1 MHz. The part of the sampled data which falls into the constant main flow condition time interval was used for processing.

The wall temperature signals acquired by thin film sensors were decomposed into mean and fluctuating components. The mean value was used to calculate the heat flux by solving 1D heat conduction equation while substrate of the sensors considered as semi-infinite medium. Following this procedure, the heat transfer coefficient h was calculated by using the wall and the gas temperatures. Finally, Nusselt numbers for each sensor were calculated. The root mean square (RMS) of the temperature was extracted from the fluctuating component of signal to measure the level of unsteadiness in wall temperature on each gauge locations.

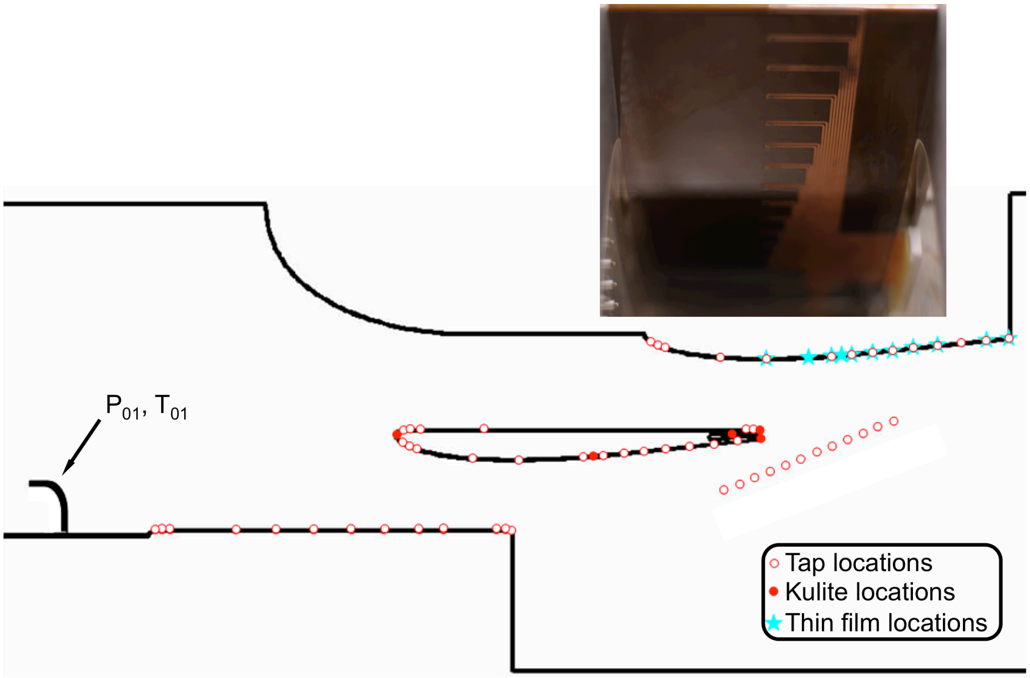

Fig. 2.18. Pressure and temperature measurement locations

2.4.3 Schlieren flow visualizations

High speed Schlieren flow visualizations were performed with the Z-type Schlieren setup [70]. The 800x600 pixel resolution pictures were acquired at a rate of 3200 Hz by a Phantom V9 high-speed camera. A digital image processing algorithm was developed in

Matlab® to analyze the images. Each single image was automatically rotated and cropped around the area of interest. A local background was created and subtracted from the image to compensate for illumination variations. The algorithm converted this image portion into a binary image, i.e. a logical array, and tagged its connected components providing a label matrix, where each object was identified with a positive integer number. The geometrical properties of the detected objects were obtained by measuring the characteristics of each labeled component in the label matrix. Eccentricity was used as criterion to select the one that corresponds to the compression wave among the detected items. The center and the orientation of the wave were then stored for further investigation. Spectral analysis of the Schlieren images allowed identifying the shock displacement frequency and angle variation amplitude. The impingement location of the shock wave on the adjacent suction surface was also extracted as complementary information for the blade loading measurements.

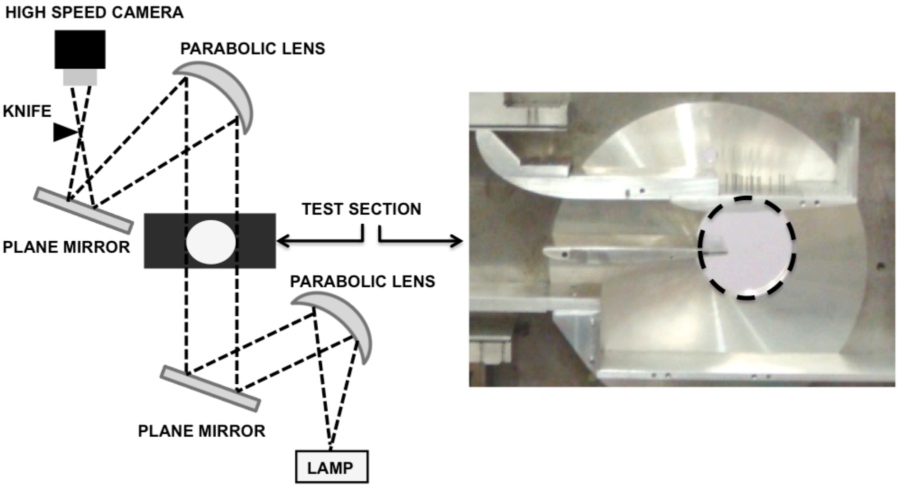

Fig. 2.19. Schematic of Schlieren setup and test section

2.4.3.1. Quantitative procession of Schlieren pictures

In order to correctly analyze Schlieren images, it is necessary to suppress the vibration-induced image shift by re-centering them. A devoted algorithm has been developed (Fig. 2.20) to bring every image to the same alignment with highest precision.

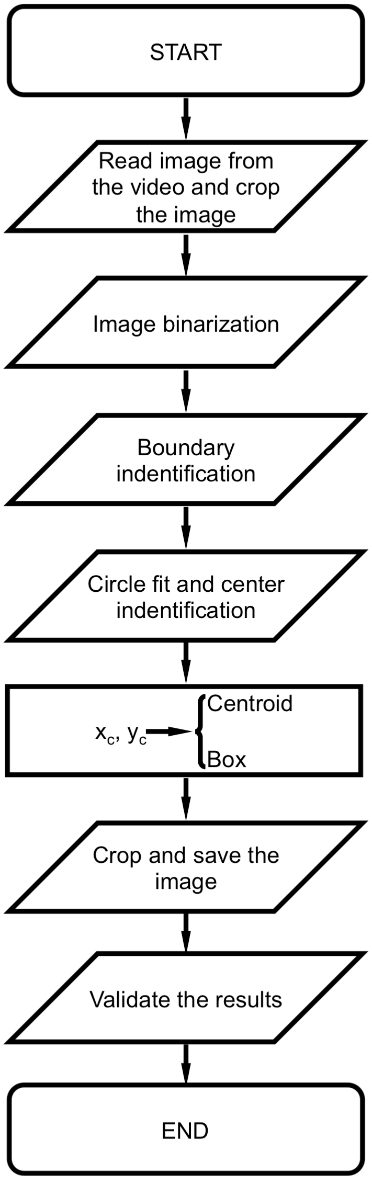

Fig. 2.20. Vibration suppression algorithm flowchart

In order to re-center each image read from the Schlieren video, an object that preserves its shape and size despites vibrations and illumination inhomogeneity needs to be chosen and used as reference target. In this study, two objects were suitable: the trailing edge cooling channel and the optical window. The latter was selected since its results were found to be more reliable and stable. The image is cropped around the bottom left optical window quadrant, which is the less sensitive image portion to light variation.

The image was then binarized with a modified global image threshold based on Otsu's method [71]. The threshold was in fact halved respect to the default value, so that the optical window was emphasized. The holes inside the binary image were filled, in order to obtain a unique continuous circle corresponding to the window itself.

The exterior boundary (Fig. 2.21-a) of the window is traced in the binary image via the *bwboundaries* function. A subset of points is selected for the fitting. These points correspond to the bottom left quadrant of the circle and are automatically found by the program.

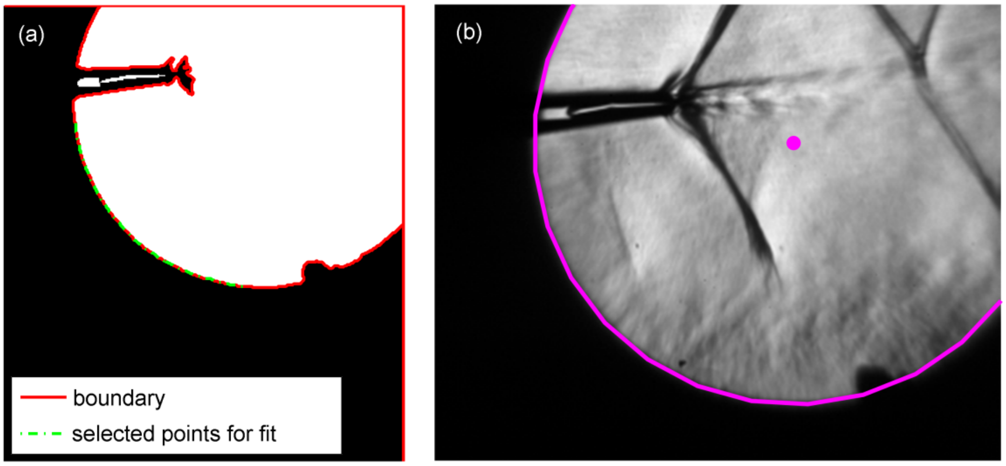

Fig. 2.21. (a) Binary image boundary selection, (b) Circle fit and centre identification

The points belonging to the circle boundary were fitted with Bucher's circle-fit function [72], which is based on the minimization of the sum of squared radial deviations. The method provides the center coordinate and the radius of the circle (Fig. 2.21-b). The program stores both the center coordinates (x_c,y_c) and the radius of the circle for further analysis. A crop-rectangle is built around the circle center. The original image is cropped by the width and height of the rectangle which are set at about 1.5 times the mean optical window diameter. Thus the new image is centered in (x_c,y_c), and saved.

The vibration suppression algorithm was validated by re-running the program on the new re-centered images (no initial crop applied) and comparing the center dispersions (x_c-x_m,y_c-x_m). Fig. 2.22-a and Fig. 2.22-b show the center coordinates dispersion and the center distance distribution, respectively. Both in the x and y direction the shift is reduced of about six times, from an average mean-center distance Δ of 2.5 pixels to a mean distance of 0.45 pixels.

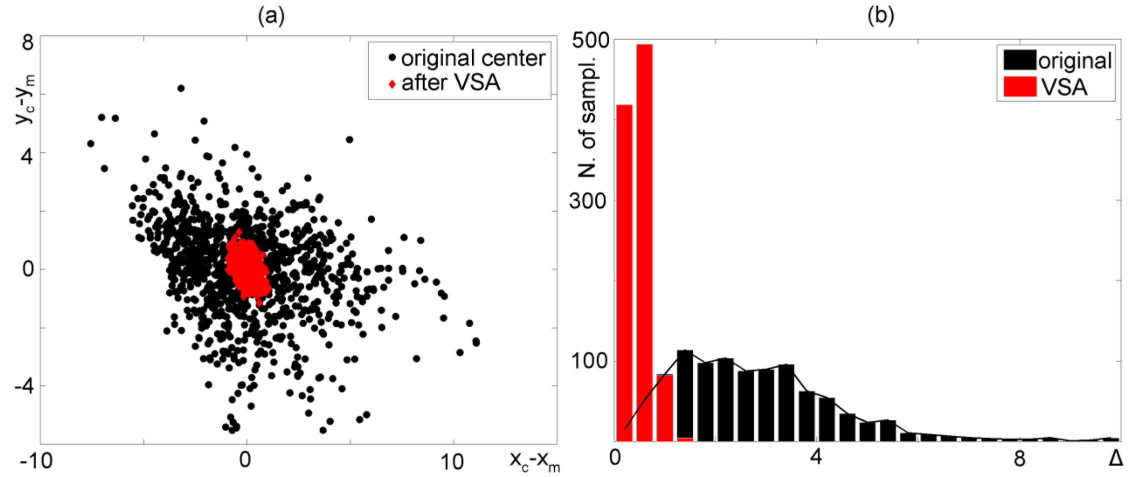

Fig. 2.22. (a)Image centre coordinate dispersion plot, (b) Mean centre distance distribution

Shock wave identification algorithm

Decision making algorithms find their application in variety of fields from cancer diagnosis [73] to airbag control [74]. These programs are typically tailored *ad hoc* on the specific problem, since the creation of a “computer-aided” decision procedure requires the transformation of the properties, belonging a particular phenomenon, into measurable quantities.

It is known in fact that even if an image may look confused, many objects are intersecting each other or small branches are interfering with the main path, an experienced person can still identify the principal target among the others. The main goal of this work was to translate the human brain “natural” correlations into mathematical operations in case of shock wave identification. When more scenarios were possible, mathematical, geometrical or logical criteria were found to allow the program to take the correct decision. A Digital Image Processing algorithm was therefore developed with Matlab® to automatically analyze the Schlieren images. The flow chart of the program is shown in Fig. 2.23 and detailed hereafter.

1. Each single image is read and cropped around the area of interest.

2. A local background is created and subtracted from the image to compensate for illumination variations which is computed row by row, by computing the average columns intensity. Then, the algorithm converts this image portion into a binary image, i.e. a logical array.
3. The program labels (*bwlabel*) the connected components providing a label matrix L, where each object is identified with a positive integer number, following the general procedure outlined in [75]:
   a) Run-length encode the input image.
   b) Scan the runs, assigning preliminary labels and recording label equivalences in a local equivalence table.
   c) Resolve the equivalence classes.
   d) Re-label the runs based on the resolved equivalence classes.
4. The properties of the detected objects are collected in the label matrix by measuring the characteristics of each labeled component. Both shape properties (e.g. area, centroid, eccentricity, equivalent diameter…) and pixel value measurements (e.g. maximum intensity, pixel values…) are provided by Matlab® built-in function *regionprops*.
5. In order to eliminate small bifurcations, minor waves or reflections, only the subset of pixels with the higher intensity is selected among those belonging to the identified objects (Fig. 2.24-a). Since per each row x_i, more columns $y_{i,j}^*$ may respect this condition, a mean bifurcation line is computed:

$$y_{m,i}^* = \frac{1}{n} \sum_{j=1}^{n} y_{i,j}^* \tag{2.5}$$

and, to exclude outliers, only the points $y_{i,j}^\#$ that lie within a distance ε from $y^*_{m,j}$ are chosen. The correct mean line is finally re-built row by row:

$$if \quad \left| y_{i,j}^* - y_{m,i}^* \right| \le \varepsilon \rightarrow y_{m,i} \tag{2.6}$$

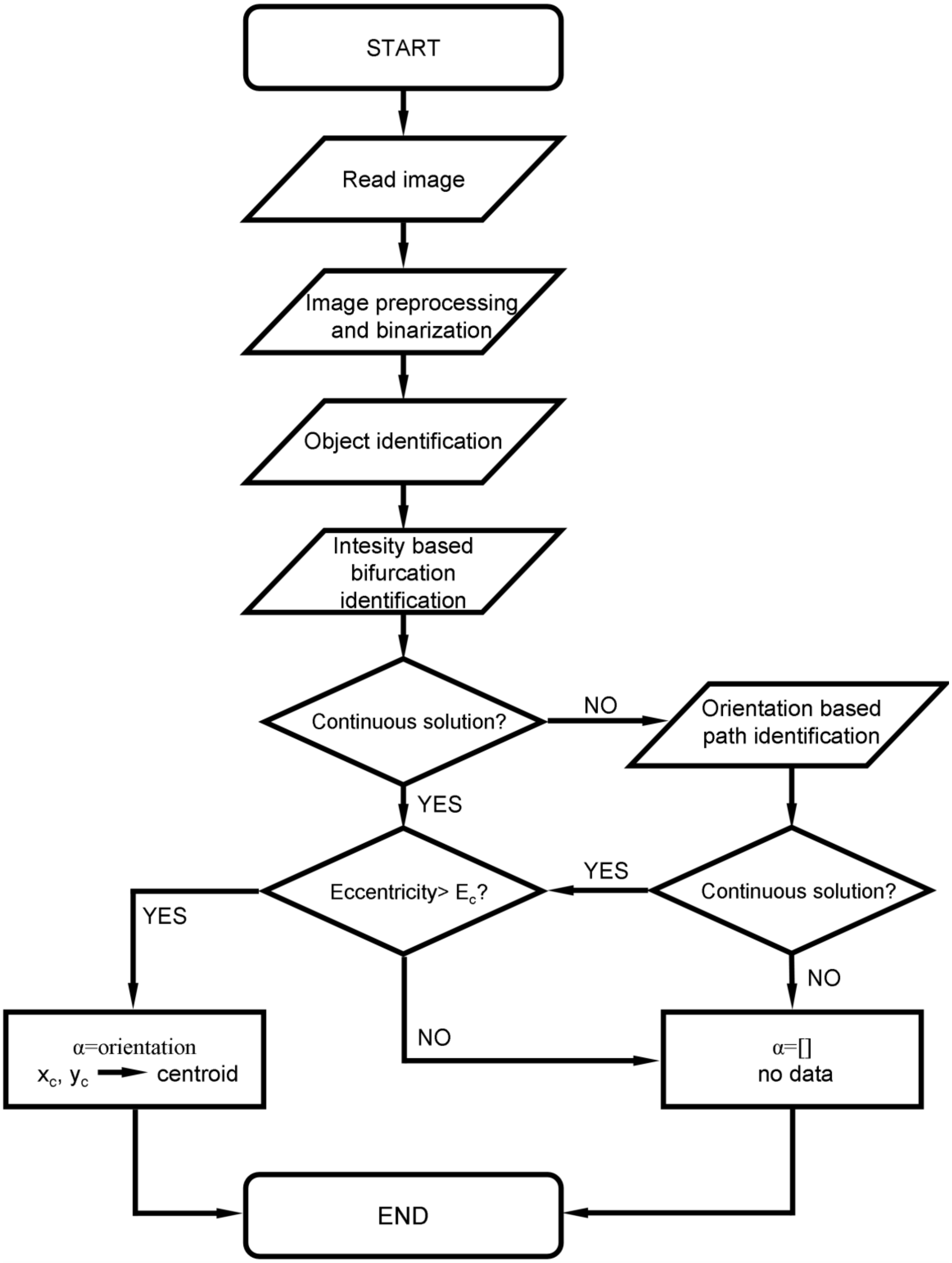

Fig. 2.23. Shock wave detection algorithm flow chart

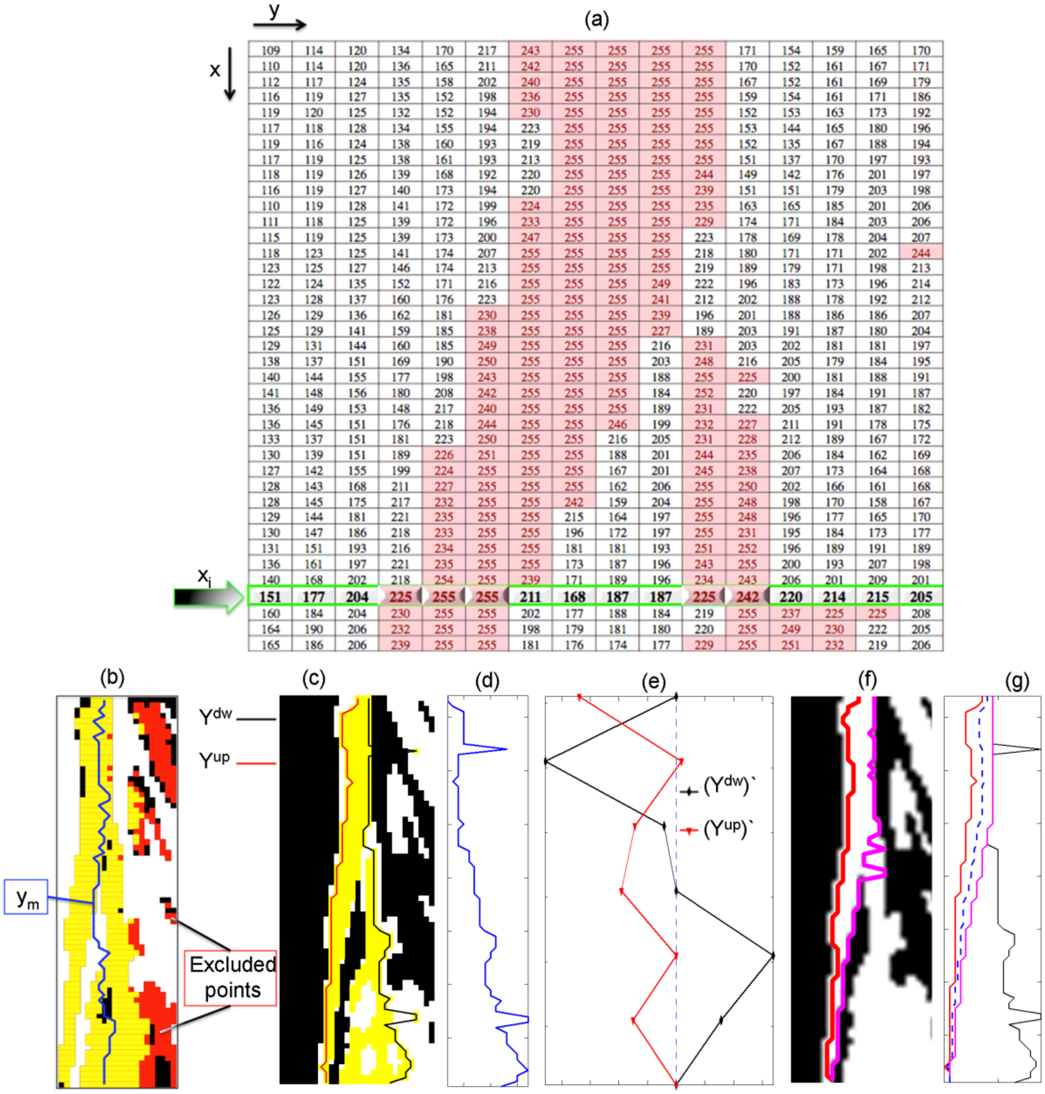

109	114	120	134	170	217	243	255	255	255	255	171	154	159	165	170
110	114	120	136	165	211	242	255	255	255	255	170	152	161	167	171
112	117	124	135	158	202	240	255	255	255	255	167	152	161	169	179
116	119	127	135	152	198	236	255	255	255	255	159	154	161	171	186
119	120	125	132	152	194	230	255	255	255	255	152	153	163	173	192
117	118	128	134	155	194	223	255	255	255	255	153	144	165	180	196
119	116	124	138	160	193	219	255	255	255	255	152	135	167	188	194
117	119	125	138	161	193	213	255	255	255	255	151	137	170	197	193
118	119	126	139	168	192	220	255	255	255	244	149	142	176	201	197
116	119	127	140	173	194	220	255	255	255	239	151	151	179	203	198
110	119	128	141	172	199	224	255	255	255	235	163	165	185	201	206
111	118	125	139	172	196	233	255	255	255	229	174	171	184	203	206
115	119	125	139	173	200	247	255	255	255	223	178	169	178	204	207
118	123	125	141	174	207	255	255	255	255	218	180	171	171	202	244
123	125	127	146	174	213	255	255	255	255	219	189	179	171	198	213
122	124	135	152	171	216	255	255	255	249	222	196	183	173	196	214
123	128	137	160	176	223	255	255	255	241	212	202	188	178	192	212
126	129	136	162	181	230	255	255	255	239	196	201	188	186	186	207
125	129	141	159	185	238	255	255	255	227	189	203	191	187	180	204
129	131	144	160	185	249	255	255	255	216	231	203	202	181	181	197
138	137	151	169	190	250	255	255	255	203	248	216	205	179	184	195
140	144	155	177	198	243	255	255	255	188	255	225	200	181	188	191
141	148	156	180	208	242	255	255	255	184	252	220	197	184	191	187
136	149	153	148	217	240	255	255	255	189	231	222	205	193	187	182
136	145	151	176	218	244	255	255	246	199	232	227	211	191	178	175
133	137	151	181	223	250	255	255	216	205	231	228	212	189	167	172
130	139	151	189	226	251	255	255	188	201	244	235	206	184	162	169
127	142	155	199	224	255	255	255	167	201	245	238	207	173	164	168
128	143	168	211	227	255	255	255	162	206	255	250	202	166	161	168
128	145	175	217	232	255	255	242	159	204	255	248	198	170	158	167
129	144	181	221	235	255	255	215	164	197	255	248	196	177	165	170
130	147	186	218	233	255	255	196	172	197	255	231	195	184	173	177
131	151	193	216	234	255	255	181	181	193	251	252	196	189	191	189
136	161	197	221	235	255	255	173	187	196	243	255	200	193	207	198
140	168	202	218	254	255	239	171	189	196	234	243	206	201	209	201
151	**177**	**204**	**225**	**255**	**255**	**211**	**168**	**187**	**187**	**225**	**242**	**220**	**214**	**215**	**205**
160	184	204	230	255	255	202	177	188	184	219	255	237	225	225	208
164	190	206	232	255	255	198	179	181	180	220	255	249	230	222	205
165	186	206	239	255	255	181	176	174	177	229	255	251	232	219	206

Fig. 2.24. Intensity based main bifurcation identification: the image as a matrix (a), outliers exclusion (b), solution continuity evaluation: Y^{up} and Y^{dw} (c), their difference ΔY (d), piecewise derivative of Y^{up} and Y^{dw} (10 points per piece) (e), shock boundary identification (f) and final shock direction (g)

Per each coordinate x_i the upstream and downstream border coordinates (Y^{up} and Y^{dw}, Fig. 2.24-c) are selected from the intensity-identified cloud of points (x_i, $y_{i,j}^{\#}$). The continuity of the bifurcation line y_m is verified by evaluating the normalized difference between the two border lines (Fig. 2.24-d):

$$\Delta Y_i = \left| Y_i^{up} - Y_i^{dw} \right| \tag{2.7}$$

$$d\Delta Y = \left(max(\Delta Y) - min(\Delta Y) \right) / mean(\Delta Y) < \varepsilon_b \tag{2.8}$$

a) If the normalized distance difference $d\Delta Y$ is lower than a threshold value (e.g. 1.5 pixels), the coordinates cloud (x_i, $y_{i,j}^{\#}$) is passed to the main program, where it is transformed into a binary image, identified as an object and measured.

b) If $d\Delta Y > \varepsilon_b$ the orientation-based path identification module is called.

6. The two lines Y^{up} and Y^{dw} are filtered with a low pass filter in order to exclude the higher and sharper peaks. Their piecewise derivative is then computed (Fig. 2.24-e) by solving the least square problem:

$$m_k = V_k \left(y_{k,j} \right)^{-1} \tag{2.9}$$

where k indicates the k^{th} piece of points.

The line with the minimal derivative variation (absolute value difference and number of sign inversions) is indicated as the correct shock wave outer border. In the example of Fig. 2.24-e, the upstream line Y^{up} is therefore the one that represents the wave border Y_S^{out}. Finally the inner border of the bifurcation is computed (Fig. 2.24-f) as it follows:

a) per each row x_i, starting from the selected outer border $Y_{S,i}^{out}$ and going toward the image centre, the difference between two successive points among $y_{i,j}^{\#}$ is computed:

$$\Delta y_i = \left| y_{i,j}^{\#} - y_{i,j-1}^{\#} \right| \tag{2.10}$$

b) the last point that separates from the previous one of less than 1.5 pixels is selected as the inner border of the shock $Y_{S,i}^{in}$.

The coordinate of the points lying within Y_S^{in} and Y_S^{out} are passed to the main program, where they are transformed into a binary image, identified as an object and measured.

7. Eccentricity is used as ultimate criterion to select, among the detected items, the one that corresponds to the compression wave or to verify that the selected object is compatible with a shock wave. If the eccentricity is bigger than the threshold

imposed, the centre and orientation of the wave are computed and stored for further analysis, otherwise no data are saved.

8. The program loops over all the Schlieren images, providing the time-resolved shock wave angle and centre coordinate.

2.6 Numerical modeling of simplified geometry for parametrical study

2.6.1 Numerical tools and computational domain for steady state analysis

Numerous applications of Reynolds-averaged Navier-Stokes equations (RANS) with k-ε turbulence models for predicting high Reynolds number turbulent flows and viscous-inviscid interactions have been documented in the literature [76-78]. The flow field around a trailing edge section with a set of different cooling ejections can be reproduced using a validated computational solver and a computational domain appropriately meshed. In this section, the solver validation and the grid selection are described.

2.6.1.1 Solver validation

The numerical validation has been performed on a backward facing step due to the similarity with the trailing edge flow. The topology of the Prandtl-Meyer expansion fan, boundary layer detachment forming a shear layer between the supersonic flow and the subsonic recirculation region, wake lip and reattachment shock waves are analogous for both geometries. The experimental results obtained by Smith [79] on M=2.5 stream flowing over a supersonic rearward facing step were used for the validation of RANS solver. The geometry used in Smith's experiments had a 0.0113 m step, and 0.1016 m upstream section for the incoming boundary layer to develop. The downstream part was kept 0.3048 m long to capture well the supersonic flow features. The domain was enclosed with a slip wall 0.1588 m above the step. The pressure inlet and outlet boundary conditions were set to 127553 Pa and 7750 Pa respectively to match the experimental conditions at M=2.5 and $Re=78.74\times10^6/m$. The inlet total temperature was 344 K. In the calculation, the fluid domain was meshed using triangles with a non uniform rectangular boundary layer mesh close to the wall. To solve the laminar sublayer, $y^+<1$ was kept for the incoming turbulent boundary layer. The resulting 2D mesh consisted of 30,000 grid points.

The methodology validation was performed using the commercial CFD package ANSYS 14 (Fluent). The fluid was considered as an ideal gas and the equation was solved explicitly using the density based solver due to the high compressibility effects. A second order upwind differencing was used in the space domain. The turbulence of this high Reynolds number flow is modeled using two equation realizable k-ε model. The enhanced wall treatment with pressure gradient effects was selected to account for compressibility and pressure gradient. Pressure inlet and non-reflective outlet boundary conditions were imposed. The walls were considered adiabatic with the non-slip velocity condition. Convergence was assumed when the absolute residual for all variables became less than 0.001. Fig. 2.25 shows the good agreement between the experimental and numerical traces of the shadowgraph images. All the relevant flow patterns were reproduced in the numerical calculations with accuracy, namely the expansion fan, shear layer, separation shock and reattachment shock.

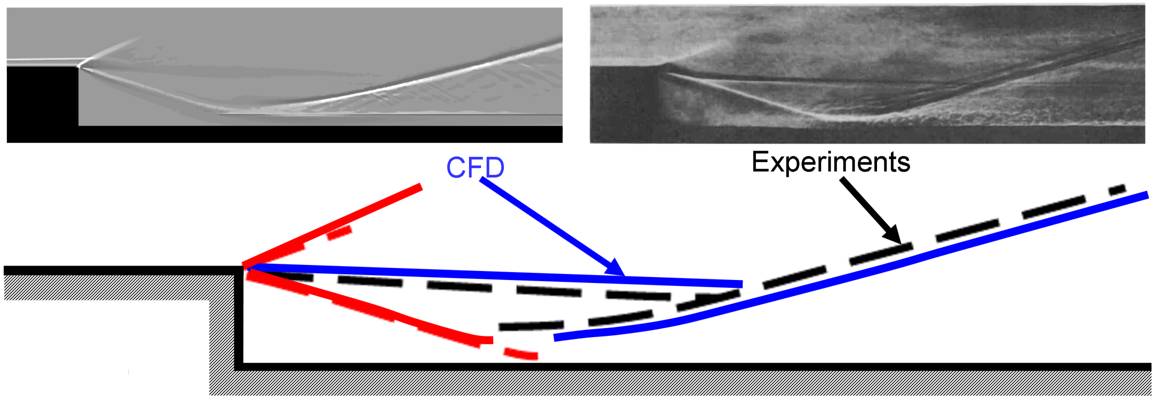

Fig. 2.25. Comparison of main flow features extracted from shadowgraph images of the experimental results of Smith (dashed) and FLUENT solver (solid) for M=2.5.

2.6.1.2 Computational grid and operating conditions

The test model consists of a flat plate with a blunt trailing edge with a cooling slot placed at the center of the trailing edge. Fig. 2.26 displays the computational domain and enlarged view of the grid around the cooling channel. The grid is highly resolved on the boundaries, corners and the wake.

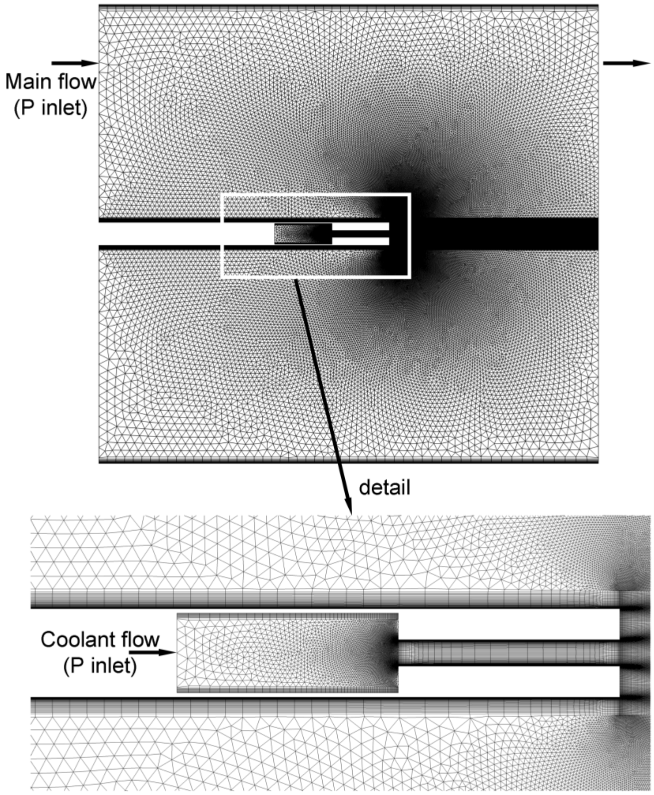

Fig. 2.26. Computational domain of mesh at trailing edge and cooling slot region.

The computational domain had a length of 21.75d (d is the trailing edge thickness equal to 0.02m) and 20d wide. The cooling channel duct length and width were 2.5d and 0.3d respectively. The coolant air was fed by a larger cavity, with a width 3 times larger than the cooling channel to ensure low subsonic conditions. The computational domain was meshed with 140,539 nodes considering two distinct zones. The structured non uniform rectangular mesh close to the solid boundaries, namely the surface of the flat plate, the trailing edge, and the cooling channel were refined to resolve the boundary layer. The resulting y^+ values were lower than 1 on the trailing edge. The outer grid was meshed with unstructured triangles with a growth factor rate of 1.1 and keeping a maximum size of 0.05d. At the main flow inlet, uniform total and static pressures were imposed equal to 368470 and 10000 Pa respectively. A stagnation temperature of 365 K was imposed to obtain 1.5 inlet Mach number. The Reynolds number at the inlet was 9.4×10^6. The coolant pressure was varied between 17% and 211% of the free stream, with the coolant temperature kept at 300 K.

2.6.1.3 Grid independence

A thorough study of the grid sensitivity was carried out to ensure the time averaged unsteady Reynolds Averaged Navier Stokes (URANS) solutions were grid-independent for a particular meshing scheme. This task was conducted on a configuration with subsonic coolant jet where the coolant pressure was 19% of main flow total pressure.

Three meshes were used (N_1, N_2, N_3), resulting in a refinement ratio $r=(N_{coarsen}/N_{refine})^{0.5}$ close to 1.5, where N is the number of cells with same growth rate and y^+ values with $N_1>N_2>N_3$. To evaluate the grid sensitivity the base pressure was calculated through area weighted average criteria (ϕ). The difference in the variable ϕ between two grids is denoted by $\varepsilon_{xy}= \phi_x-\phi_y$. Using the method proposed by Richardson [80], an apparent refinement ratio (p) and an extrapolated parameter of study were obtained, 2.66 and 61484 Pa respectively, according to Stern et al. [81]. The grid convergence study is summarized in Table 2.1. The base pressure showed a monotonic behavior with a negligible uncertainty for the grid N_1. According to the results, the grid N_2 represented a relative error lower than 2 %. Hence, the grid N_2 was selected as an efficient grid to perform the following numerical simulations. The time step was adapted to each condition, ranging from 0.5 to $5\text{x}10^{-6}$ s. Convergence was achieved after 6 to 20 thousand time steps which required 180 to 600 computational hours in a 6-core Intel i7 2.8 GHz with 8 GB RAM.

Table 2.1. Grid independence and relative error study results.

Grid	Number of Nodes	ϕ	r	ε	Error (%)
N_1	271,146	61812	1.39	-650	0.05
N_2	140,539	61162	1.25	-2393	1.12
N_3	88,848	58769			4.9

2.6.1.4 Numerical procedure to analyze shock waves

Shadowgraphs have been utilized to detect the gradients since the 17th century [70]. Schlieren techniques have been powerful experimental tools to detect the supersonic flow structures with sharp density gradients, such as shock waves and expansion fans. Other methodologies, like background oriented Schlieren or calibrated color schlieren, have been applied to provide a quantitative understanding of the flow field [70, 82-84]. The density gradient fields of the numerical results have similarly been post-processed. Fig. 2.27 depicts the methodology to obtain a comparative evolution of the shock wave properties for different cooling conditions. First of all, the density gradient field was split into the axial and normal components (∂ρ/∂x and ∂ρ/∂y). Secondly, the gradient data was sampled on the horizontal measurement lines to track the flow features. Data along each horizontal line (i,…,v,…,x…)was treated by a Matlab routine to determine the maximum and minimum values of density gradient components along the horizontal and vertical directions. Those maximum and minimum, respectively displayed in step 3, designate the location of the trailing edge shocks at each height. The mean level of compression across the shock wave was evaluated based on the modulus of the density gradient. On the fourth step, the trailing edge shock wave was reconstructed by using the least square fit on the coordinates of the extreme gradient values. Hence, the inclination angle, position of the shock wave together with the intensity was obtained for each cooling condition.

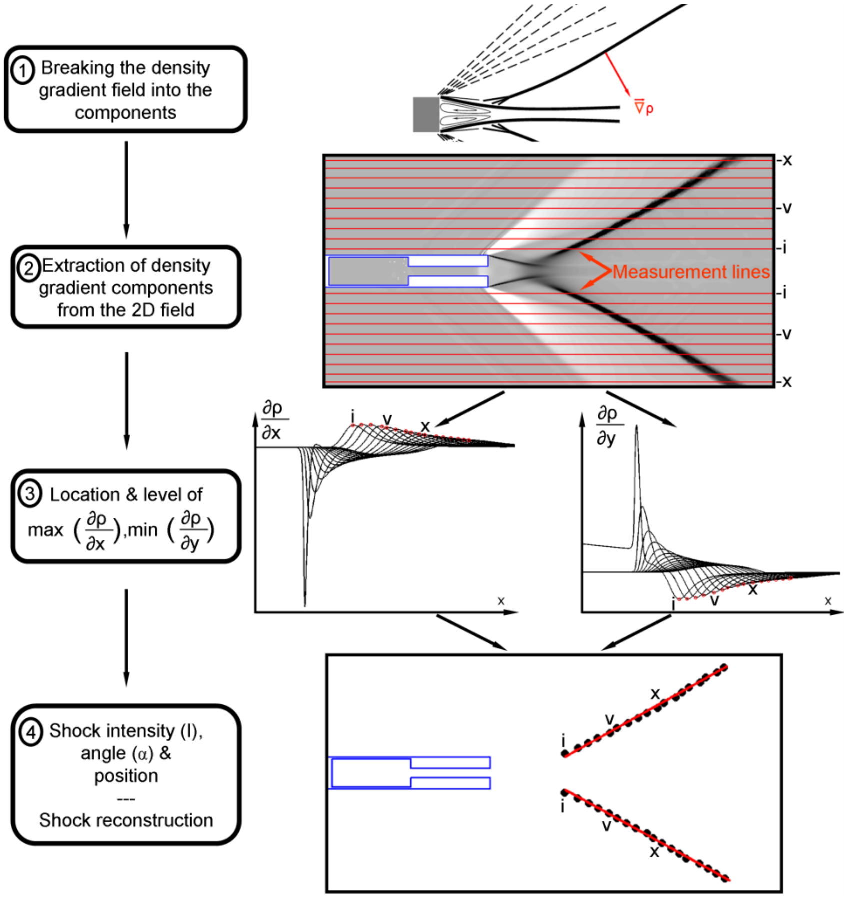

Fig. 2.27. Post-processing procedure for shock identification.

2.6.2 Numerical tools and computational domain for transient analysis

In order to study the flow behavior at the trailing edge, a simplified two-dimensional geometry has been modeled representing the rear part of an airfoil trailing edge. The computational domain is illustrated in Fig. 2.28-a and Fig. 2.28-c, with a rectangular shape 22.5dx20d, where d is the trailing edge thickness. The length of the flat part from the inlet to the trailing edge is 12.65d while the coolant inlet section is 0.9d. The coolant channel is made up of a 2.5d long settling chamber and following a contraction 0.3d, on each side, a 2.5d long 0.3d wide section up to the coolant exit (Fig. 2.28). The outlet section is 20d downstream of coolant exit section.

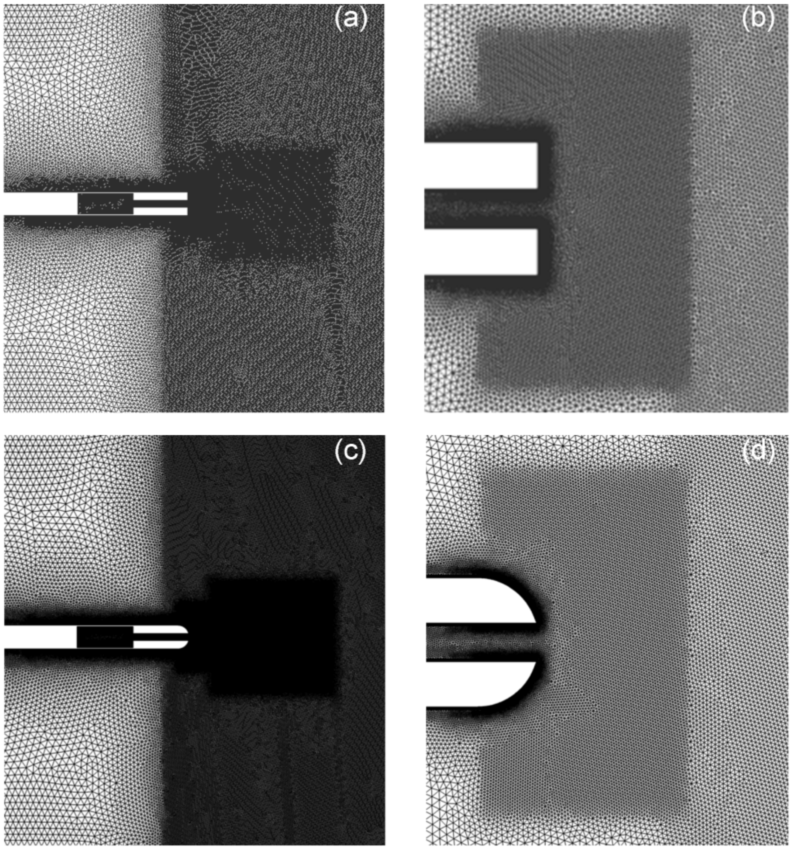

Fig. 2.28. Meshes used for unsteady simulations: (a) rectangular trailing edge section, (b) in detail (c) rounded trailing edge section (d) in detail

A 2D hybrid unstructured grid has been generated: 20 prismatic layers have been used for the boundary layer evaluation and a refined mesh has been created in the wake/shock region to better represent the shock system and the base region (Fig. 2.28-b and Fig. 2.28-d). The simulations were carried out with University of Florence's in-house HybFlow URANS solver, which was previously validated for steady and unsteady applications in transonic turbines [85, 86]. The spatial discretization is performed by means of a compressible finite volume method with up-winding for the convective terms of the Navier-Stokes equations. The upwind approach is the Roe's approximated solver of the Riemann problem [87], where the solution is reconstructed at cell interfaces by means of a least-square method. Turbulence is modeled using the standard k−ω model developed by Wilcox [88]. The inlet total temperature was set at 365K and the wall temperature at 250K, which has been chosen according to experimental data. Supersonic inlet conditions have been implemented in the solver. Inlet Mach numbers of 1.2 and 1.5 has been considered. Steady calculations on blunt and rounded geometry have been performed without coolant and at five different blowing rates. The unsteady analysis has been performed considering a time step of 3×10^{-6}s which corresponds to a sampling frequency of 333kHz. First, continuous blowing has been tested at six blowing ratios. Then sinusoidal boundary condition on mass-flow has been enforced for the rounded geometry at coolant inlet section. Two frequencies have been tested, 200 Hz and 1000 Hz, as well as two amplitudes have been adopted for each frequency, in order to give a total mass-flow variation of 40% and 80% of the mean level. The average coolant mass-flow is maintained unaltered for all the cases.

2.7 Numerical modelling of the periodic airfoil model

2.7.1 Description of the solver

The commercial solver ANSYS FLUENT was used for all the simulations. The 2D version solved the governing equations using a co-located grid, i.e. all the flow parameters were stored in the cell-centers. Regarding the spatial discretization, a second order upwind scheme was selected for the present numerical campaign. A second order temporal discretization was used to obtain the time-accurate unsteady solutions. Gradients were reconstructed using a second order accurate method based on cell volumes. Turbulence was modeled using the two-equation SST model by Menter [89]. Calculations were performed using a parallelized approach on multiple computer nodes.

2.7.2 Computational domain and parameters of the analysis

The numerical domain reproduced a single vane passage, as displayed in Fig. 2.29, considering periodic boundary conditions on the upper and lower ends of the domain. The inlet and outlet sections which were inclined according to the stagger angle of the linear cascade were located 0.5 and 0.75 chords away from the profile leading and trailing edges respectively. The computational mesh was prepared using the commercial tool Centaur. Special attention was paid to the resolution on the wall, the base and the wake regions. An O grid of 20 prismatic layers was realized around the blade. The resulting y+ value was maintained below 1 around the airfoil profile. The final mesh consisted of around 30,000 prismatic and 535,000 triangular elements. The imposed inlet total pressures, total temperatures, and flow angles corresponded to the experimental values. At the outlet, the measured average static pressure P_{s2} was imposed. All the walls were assumed to be isothermal at ambient temperature with no-slip boundary condition. To model the pulsating coolant, a user-defined function was implemented with a pressure shape, similar to the experimental conditions documented by Gonzalez et al. [66], as depicted in Fig. 2.11-left.

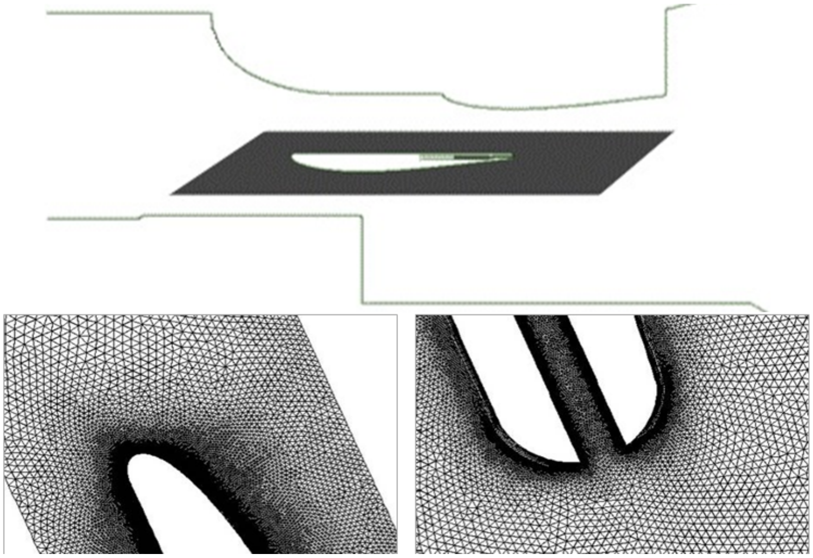

Fig. 2.29. Computational domain: as cropped from the test section (top) along with magnified views of the leading edge (bottom left) and trailing edge (bottom right).

In order to ensure a frequency resolution of 500 kHz, a time step of 1 μs was used. Time averaged data was obtained by calculating the mean of 4 consecutive periods, after verifying that the level of dispersion was below a threshold. The analysis of the data with pulsating frequency (200 Hz) was accomplished using a time step ten times larger (10 μs), because the typical period to resolve is 100 times greater. The computational time required to achieve full convergence was 1344 CPU hours in two processors, dual core AMD Opteron with 4GB RAM.

2.8 Numerical modeling of the test section

2.8.1 Description of the solver

Unsteady numerical simulations of the test section were performed to understand the characteristics of the design by using CRADLE's SC/Tetra computational thermo-fluid analysis system based on finite volume method. The discritization of the governing equations was made by cell vertex finite volume formulation in the solver. The compressible flow solver made use of segregated pressure based solution algorithms [90]. The solver has second order accuracy in space and utilizes second order implicit temporal discritization for time derivatives. Further information about the solver is provided in the literature [91-93]. For current simulations, turbulence closure is maintained by high Reynolds number shear stress transport (SST) k-ω model. Pressure inlet and atmospheric pressure outlet boundary conditions are imposed at the inlet and the outlet of the test section respectively. The surfaces were treated as adiabatic, no-slip walls. The time step for the simulations was set to be $5x10^{-7}$ seconds corresponding to 2 MHz sampling frequency to capture the highest expected frequency of unsteadiness (trailing edge vortex shedding) in the test section.

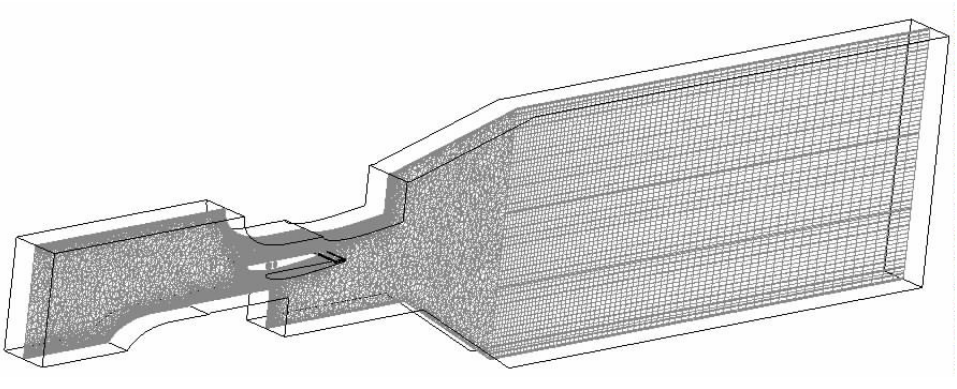

Fig. 2.30. Three-dimensional computational grid

A three dimensional computational mesh was created by using the hybrid mesh generator program that is included in the software suite. A set of five prismatic layers are placed on the solid surfaces to attain y+ values around 1 on the flow passage surfaces. The three dimensional computational domain shown in Fig. 2.30 and Fig. 2.31 is composed of approximately 16 million computational elements.

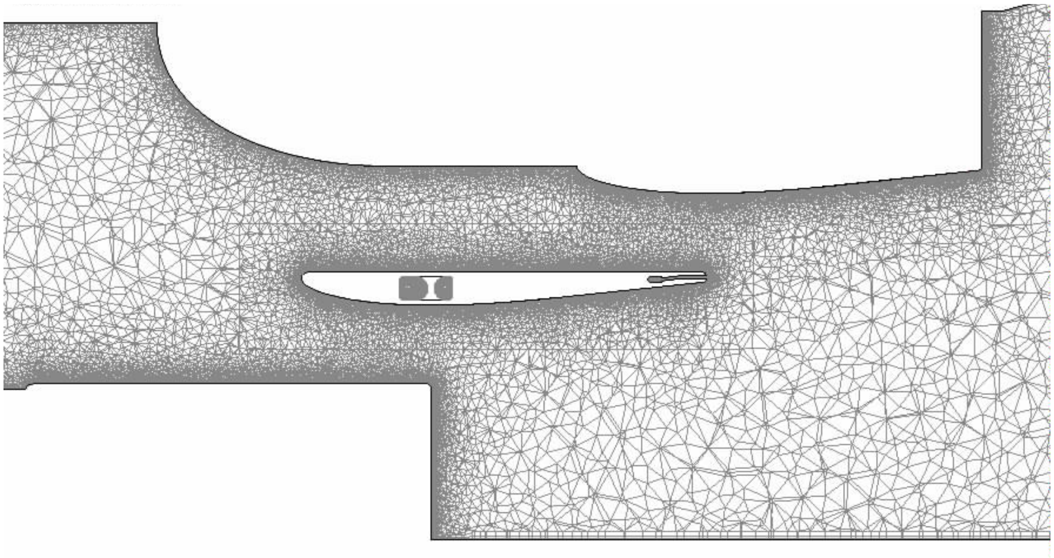

Fig. 2.31. Detailed, cross sectional view of the flow passages

3

General Aspects of the Trailing Edge Shocks and the Base Bleed Interactions in Supersonic Confined Flows

3.1. Introduction

Improvements in lifespan and efficiency of mechanical systems has steered research towards limiting detrimental aerostructural interactions and mitigating the losses. Such interactions become significantly severe when the internal flow velocities are beyond the speed of sound. Shock waves are formed at the trailing edge of the bodies submerged into the transonic and supersonic streams. The downstream propagation of trailing edge shocks causes undesired perturbations and reflections in the flow field. The subsequent unsteady forcing on solid components eventually leads to fatigue problems. The modulation of shock waves might alleviate such unfavorable consequences. Understanding the trailing edge flow field is essential to reveal the parameters affecting shock waves. Fig. 3.1 represents the flow topology at the trailing edge and downstream. Owing to Coanda effect, upstream boundary layers remain attached at the trailing edge corner, separate immediately downstream and consequently form shear layers. While simultaneously, the main flow accelerates through a Prandtl-Meyer expansion fan. The shear layers propagating from each side of the trailing edge relign downstream at the point of confluence and merge into the wake. Preceding this point, enclosed by the shear layers and the trailing edge, there is a dead air zone, where the low momentum and constant pressure flow recirculates. This area is often referred to as the base region, whose attributes are predominant on the free stream flow features, such as vortex shedding and compression waves. The compression in supersonic trailing edge flows is commonly observed in two stages. A weak and local compression wave, called separation or lip shock, is formed at the point of flow detachment in order to adapt the pressure gradient between the shearing flow and the downstream. Although the properties of the lip shock depends on both the trailing edge geometry and free stream flow conditions, it is usually embedded into the shear layer and consequently it may not be visible. Further on, at the confluence point, the flow changes its direction notably and therefore it is forced to compress originating a system of strong trailing edge shocks. The degree of compression, hence the strength of the shock waves, highly depend on the base region properties.

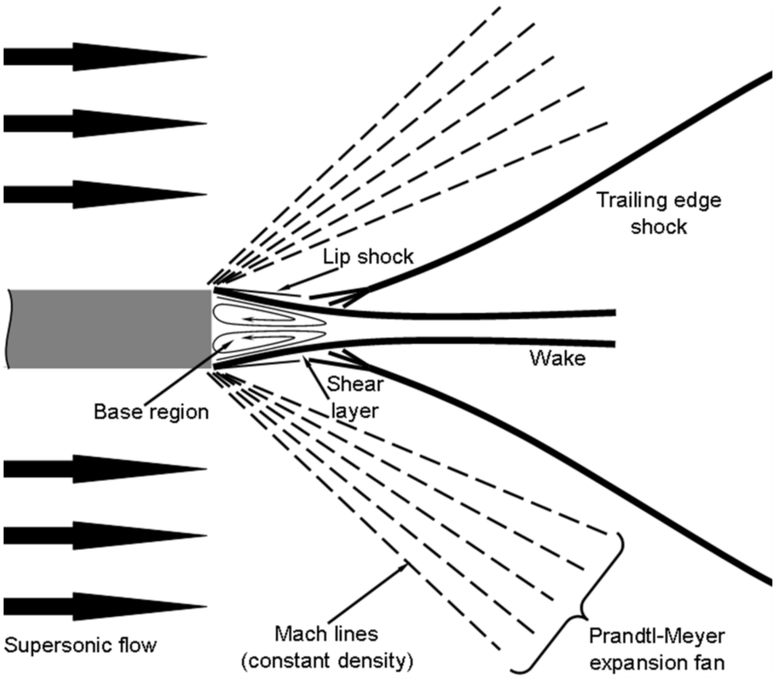

Fig. 3.1. Schematic representation of supersonic flow on a blunt trailing edge.

Several analytical, numerical and experimental studies have been dedicated to understand the characteristics of the base flows in multitude applications. Prior literature can be classified into four categories: characterization of the base pressure to reduce the base drag on wing sections and projectiles, the base pressure loss and trailing edge shocks in turbomachinery, the shock wave-boundary layer interaction, and the effects of trailing edge bleed on the base pressure and trailing edge flow.

Nash [94] reviewed the experiments on two-dimensional supersonic base flows and showed that the base pressure increases with increasing boundary layer momentum thickness. Consequently, the base drag force reduces. His later compilation recorded the effect of base pressure on the point of vortex street formation, which leads to an additional drag in subsonic speeds [95]. Moreover, a methodology was proposed to calculate the base pressure for free stream Mach numbers between 1.5 and 3, yet the relationship between the base pressure and recompression downstream remained unexplained. In conjunction with these studies, an extensive experimental work focusing on the base flows for a range of Mach number from 0.4 to 1.1 was conducted on blunt and circular trailing edges [96]. An abrupt fall in the base pressure, along with reduction in base unsteadiness, was observed as Mach numbers approached to unity. Hence the base drag increases rapidly near sonic speeds. The measurements conducted on the circular trailing edge showed comparable levels of base pressures beyond the sonic speeds. A similar analysis made for high supersonic range also showed that the trailing edge shock structure remained unchanged while the corners of a blunt trailing edge was gradually smoothened [97]. On the other hand, the point of separation moved upstream resulting in higher lip shock angles as the radius of the edge rounding was increased. Furthermore, the base pressure reduced monotonically as the Mach number increased from 2 to 4.5 for a wide range of Reynolds numbers (10^5 to $2x10^6$). Kawai and Fujii recently showed the same trend for a wider range of Mach numbers (0.5-4) through LES/RANS hybrid simulations over a circular cylinder with a blunt trailing edge. The study proved the three and two dimensional base flows exhibit similar features [98]. Following the sharp decrease in the base pressure at sonic velocities, a monotonic reduction was observed from M=1.5 till M=4. Similarly, Sieveding et al. observed conforming trends on measurements made on a flat plate with rounded trailing edge at Mach 1.0 to 2.3 [99].

Base pressure losses, along with the trailing edge flow topology, has been thoroughly investigated in turbomachinery applications, since trailing edge losses contribute up to 33% - 50% of total profile loss [100, 101]. The related losses can be split into: loss due to mixing in the wake, the pressure deficit at the base region, entropy generation across the separation shocks, and the trailing edge-shock wave interactions. As widely investigated for the drag problem in propulsion, wake mixing creates a significant efficiency reduction in thick trailing edge blades. Nonetheless, the most serious consequence of transonic flow in turbines is the shock system at the trailing edge [101]. Impingement of the trailing edge shock on the neighboring blade and the adjacent blade row perturbs the boundary layer, promotes the formation of a separation bubble and eventually flow separation on the suction surface [101, 102]. Paniagua et al. [102] numerically and experimentally investigated an uncooled transonic high pressure turbine stage, when the mean exit Mach number was increased from 1.07 to 1.24 (i.e. stronger trailing edge shocks), the turbine efficiency was reduced 5%. The trailing edge shock waves cause performance abatement and additionally high-cycle fatigue problems when interacting with downstream components.

The shock wave-boundary layer interactions and their control has also been another relevant area of research. Kornilov [103] worked on the separation length at M=3 for various Reynolds numbers, channel widths and shock strengths. The length of the separation upstream of the shock impingement location increased with increasing shock strength and decreasing Reynolds number. Tindell and Willis [104] tested in a M=2.5 wind tunnel a variable intensity shock wave and air injection at the point of separation to increase supersonic aircraft inlet performance. Separation was inhibited by blowing 1.5%-2% of the mainstream flow at three to seven boundary layer thicknesses upstream of the impingement location. Lin et al. numerically studied three passive control devices, at low supersonic flow regime, based on upstream blowing and downstream bleeding of the shock impact region. Investigations showed that the devices were ineffective in improving boundary layer profile [14]. Young et al. [105] used microjets, as an active control mechanism at the fore body of a supersonic UAV engine inlet, and reduced the engine inlet distortion by 35% with a 1.5% injection.

Auxiliary flow purging to main stream is frequently utilized in turbomachinery, as well. High pressure turbine blades, suffering from very high temperature flows, are internally cooled and substantial amount of coolant is ejected from the trailing edge towards the transonic-supersonic main stream. Several researchers [15-19, 24, 106-108] investigated the effects of trailing edge blowing on the performance of external aerodynamics. Sieverding performed detailed pressure measurements and Schlieren flow visualizations at the rounded trailing edge of a cooled flat plate [20]. The Schlieren images revealed that the trailing edge shocks became steeper with increased cooling. Cascade tests with high density coolants (CO_2 and Freon) resulted in augmented base pressure. Raffel and Kost [21], using pressure and PIV measurements, identified a significant reduction in the shock wave strength at 0.8% coolant blowing.

The current numerical research efforts aim to document a detailed analysis of the flow field around the isolated blunt trailing edge section with coolant ejection. The computational simulations facilitate the analysis of the trailing edge shock waves whose properties are significantly distorted by intrusive measurement techniques. An advanced analysis tool is proposed to track the variation of fluid properties along the flow path and in particular on the base pressure, trailing edge shock strength, orientation and shear layers. Various trailing edge flow topologies are summarized.

3.2. Blunt trailing edge

3.2.1. Steady approach

3.2.1.1. Analysis conditions and non-dimensional parameters

The main stream flow condition has been kept constant for all simulations while the coolant inlet total pressure was varied to change the coolant mass flow rate. In such analyses a certain number of other relevant non-dimensional parameters can be used to characterize the flow field. However, in this study, free stream to coolant density ratio (ρ_c/ρ_f) was used to parameterize the amount of blowing due to its common utilization in the cooling literature. Similarly to Bernsdorf et al. [109] the density value of the coolant was computed at the cavity plenum and the main flow density was evaluated at the location where coolant is ejected, namely at the base region. Nonetheless, the relationships between other cooling parameters, which were used in relevant research, are compared in Fig. 3.2. The figure shows the monotonic relationship between cooling massflow (m_c), cooling inlet pressure (P_{0c}/P_{01}), maximum Mach number at coolant jet exit (M_c), and the density ratio.

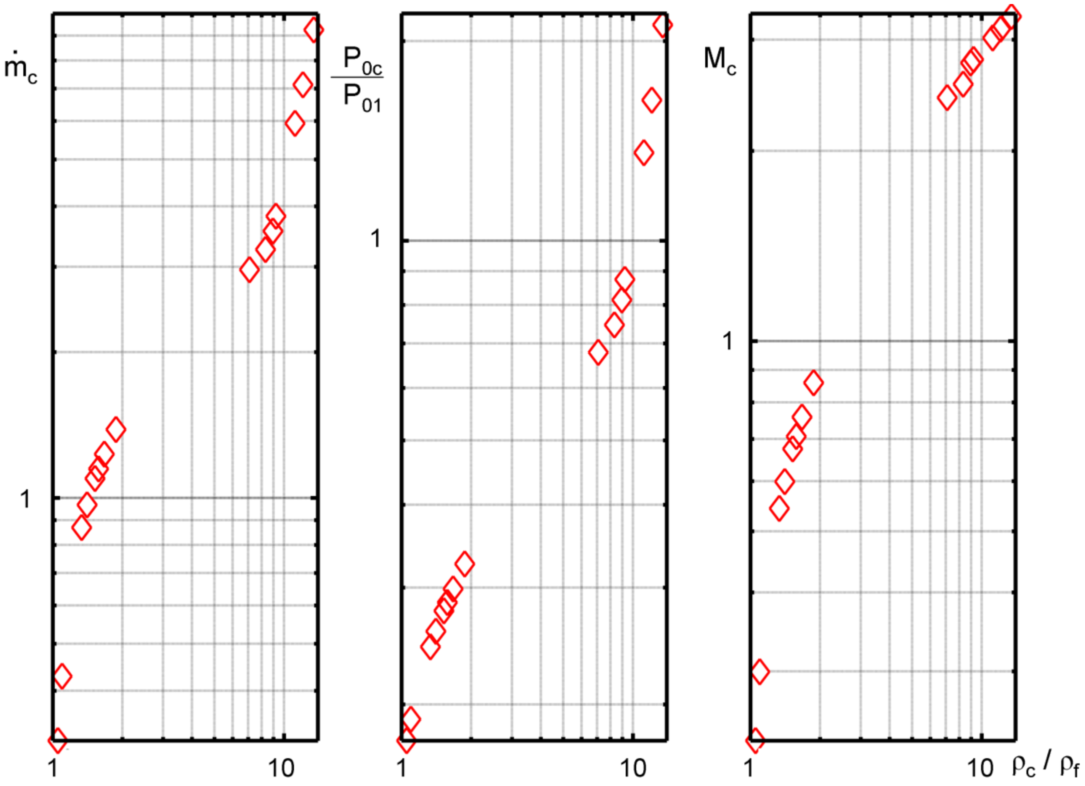

Fig. 3.2. The variation of coolant mass flow rate, coolant to main stream pressure ratios, and coolant Mach number with respect to density ratios.

3.1.1.2. Base pressure

The effect of trailing edge purge flow on the base pressure level was evaluated for a wide range of cooling rates. The base pressure values were calculated by area-weighted averaging of the static pressure very close to the trailing edge surface, at the third grid line from the surface. The extracted base pressure values were non-dimesionalized by the no blowing base pressure and represented in Fig. 3.3 in function of the density ratio.

In region b of Fig. 3.3, the base pressure levels increased with low coolant mass flows also observed previously by Sieverding [20] and Raffel and Kost [21]. Cooling air with relatively low momentum content pushed the main recirculating structure downstream, diffused into the base region and created a second set of smaller circulation zone on both sides of the trailing edge. Consequently, the pressure in the base region was increased by the filling effect of the coolant jet. In Fig. 3.3, region c, a further increase in the coolant flow resulted in an inflection on base pressure behavior. While the momentum of the coolant jet gradually increased, the entrainment of fluid contained in the dead air zone was enhanced. Thus, evacuation of the fluid from the base region diminished the pressure. Following the velocities beyond the sonic line in the coolant jet, the dissection of the base region into two isolated zones became more apparent. The base pressure continued to decrease until the coolant jet Mach number reaches 2.5, corresponding to $\rho_c/\rho_f = 8.3$. Along region d in Fig. 3.3, the expansion in the jet was enhanced substantially such that the jet shear layer compressed the recirculating region on both sides and consequently the base pressure increased.

Fig. 3.3. Base pressure correlation in function of the density ratio.

The current analysis showed that flow properties, similar to the base pressure levels, exhibited different absolute values on each half of the domain although the trends for both sides were similar. Thus, the properties representing the top and the bottom half were designated distinctively. The base pressure values on each side of the trailing edge diverged between the density ratios of 1.1 and 7.1 due to the jet deflection, probably caused by Coanda effect. Such instability has been previously documented on jet discharge and diverging flows in symmetric channel studies in the literature [110-115]. Discharging flow deflected on either side beyond a critical Reynolds number (17×10^3) and reestablished symmetry above large jet Reynolds numbers (2×10^5) as observed by Allery et al. [110]. Such phenomena have not been previously observed in turbomachinery, because of the existence of a pressure gradient between both sides of the trailing edge.

3.2.1.3. Flow topology

The trailing edge flow field, similarly to the base pressure, was highly affected by the cooling rate. Fig. 3.4 shows the flow streamlines and vorticity in the trailing edge region. The undisturbed base flow, without trailing edge blowing (Fig. 3.4-a), contained two counter rotating recirculation bubbles neatly enclosed by shear layers on each side of the trailing edge, spanning 1.7d downstream. When little coolant was ejected (Fig. 3.4-b) the dead air zone was partially penetrated by the low momentum cooling jet. The main recirculating vortex couple was pushed one trailing edge thickness downstream while reducing the height. Additionally, a new pair of vortices, which were well disconnected from each other by the coolant stream and attached to the trailing edge surface, started to grow. The cooling jet was entrained by the new recirculation pair and diffused into the base region. Accordingly, the shear layers on both side of the trailing edge were shifted outwards.

The downstream bubbles visible in Fig. 3.4-b disappeared as they are pushed by the higher momentum jet shown in Fig. 3.4-c. Moreover, the cooling jet started to entrain from the base region towards the wake. The recirculation region was reduced in size while being partially captured by the shear layer. This interaction leads to another recirculation when the coolant mass flow was further increased and the individualization of base regions on both sides of the coolant slot was complete. Consequently, two distinct base regions were observed in Fig. 3.4-d, containing a pair of relatively small counter rotating recirculating structures, developed on each side. Meanwhile, the coolant jet, achieved a supersonic regime and started to push these regions towards the shear layers on each side of the trailing edge due to a strong expansion at the jet outlet. The shear layers shrunk towards the centerline shortly after the boundary layers separated and thus created sharper corners close to the trailing edge. The increasing pressure gradient at the coolant ejection, i.e. mass flow rate, led to an overexpansion and thus coolant jet size started to grow comparable with the trailing edge thickness. The shear layers containing the high Mach number purge started to interact with the main flow shear layers and subsequently deformed the shape of the base region by moving them outward. An additional compression corner followed by an expansion was created on the main flow. Subsequently, the flow deflected once again at the confluence point located more than two trailing edges downstream and formed the wake. The base pressure was observed to be increasing in this range mainly due to the entrapment of the base flow on a small recirculation region and constantly compressed by the coolant jet shear layers.

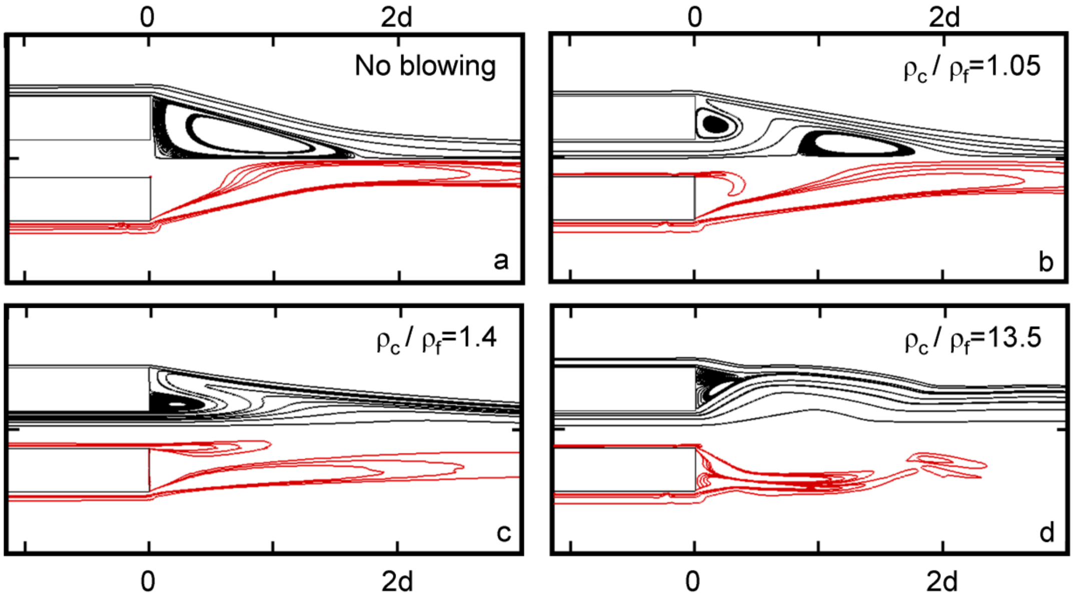

Fig. 3.4. Changes in base region flow topology shown by streamlines (top) and vorticity magnitude (bottom) a) no blowing b) $\rho_c/\rho_f = 1.05$ c) $\rho_c/\rho_f = 1.4$ d) $\rho_c/\rho_f = 13.5$

3.2.1.4. Shock wave properties

The characteristics of the trailing edge shock systems were investigated for a wide range of cooling rates. The shock wave properties obtained during the absence of blowing were used as reference case to normalize the trailing edge shock intensity and shock angle for all conditions.

Fig. 3.5 presents the changes in the trailing edge shock properties in function of density ratios, Fig. 3.5-I displays the shock intensity while Fig. 3.5-II the shock angle. Parallel to the elevation in base pressure levels, the properties of the shock wave were observed to be changing significantly for the little coolant mass flows (region b in Fig. 3.5). The compression across the trailing edge shock was reduced 87% from the no blowing value. The flattening of shear layer lowers the deflection of the flow on the wake and consequently the degree of compression reduces (as noted in Fig. 3.4-b). Moreover, the geometrical orientation changes in such a way that the shock became steeper (2.5 deg.) and the confluence point, where the shock wave was generated, was displaced 0.25d downstream.

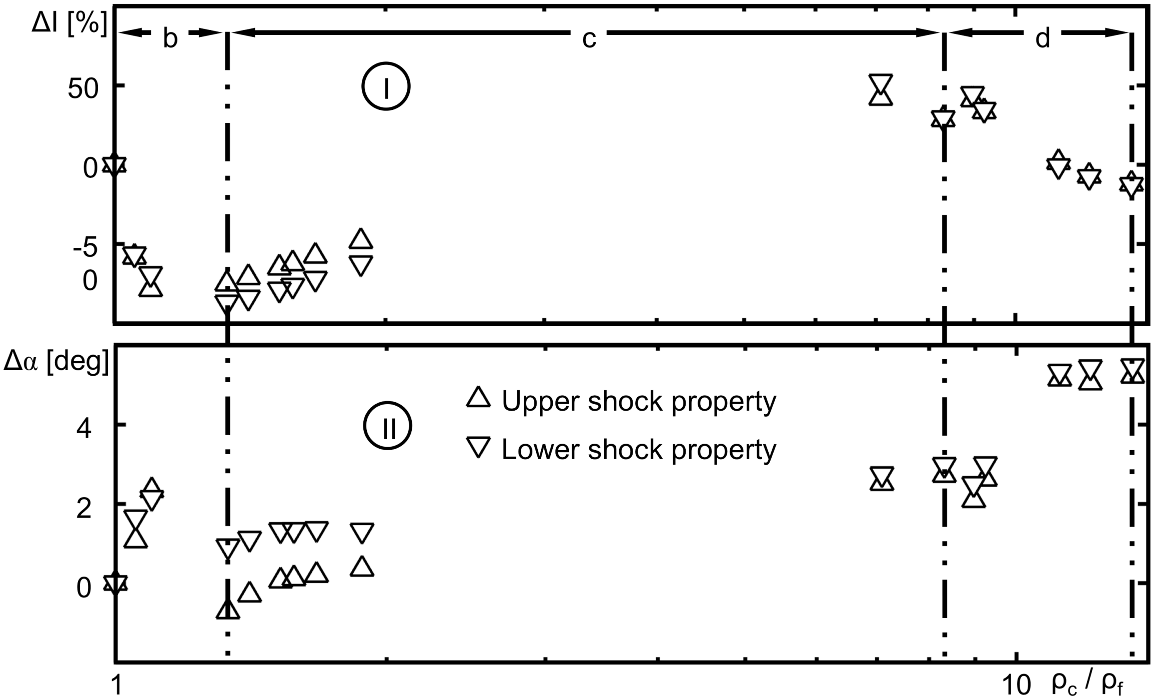

Fig. 3.5. Characterization of trailing edge shock waves: shock intensity (I) and angle variation (II) with respect to density ratio

The positive effect of base pressure augmentation was observed for a narrow range of low purge rates. The intensity of the shock started to increase following the decline in the base pressure (Fig. 3.5-c). Though, the shock intensity was still lower than the no blowing level. Flatter shear layer orientation, resulted in lower flow deflection and thus a milder compression was observed. Moreover, the location of the shock wave formation was displaced 2d and 1.5d upstream on the sides of the trailing edge with lower and higher base pressure respectively. The trailing edge shock wave strength exceeded 50% of the null blowing level when the density ratio was equal to 7.1. Shear layers were observed to be collapsing towards the base region and together with low compression corner angle resulted in a more abrupt flow deflection and consequently stronger shock waves. Further increase in density ratio, represented in region d of Fig. 3.5 resulted in a more normal shock wave (5 deg.) variation. The origin of the shock wave was gradually propagated from one trailing edge to 2.3d downstream. Moreover, the shock wave intensity was increased as high as 45% for the high coolant blowing regime.

In absence of coolant ejection or minimum purge, the oblique shock waves, which identically appeared on both sides, were observed to be forming at the point of confluence 2d downstream of the trailing edge as depicted in Fig. 3.6–I. Additionally, weak lip shocks appeared symmetrically right after the flow separation at the trailing edge. Fig. 3.6-III shows the properties of the secondary compression waves. The lip shock waves were observed to be 98% weaker and 10 degrees more oblique with respect to the main shock for the no blowing case. It originated 0.2d downstream of the trailing edge. For the lowest density ratio (ρ_c/ρ_f=1.05), a more normal lip shock with slightly higher relative intensity was observed. No separation shock was detected for the higher density ratios.

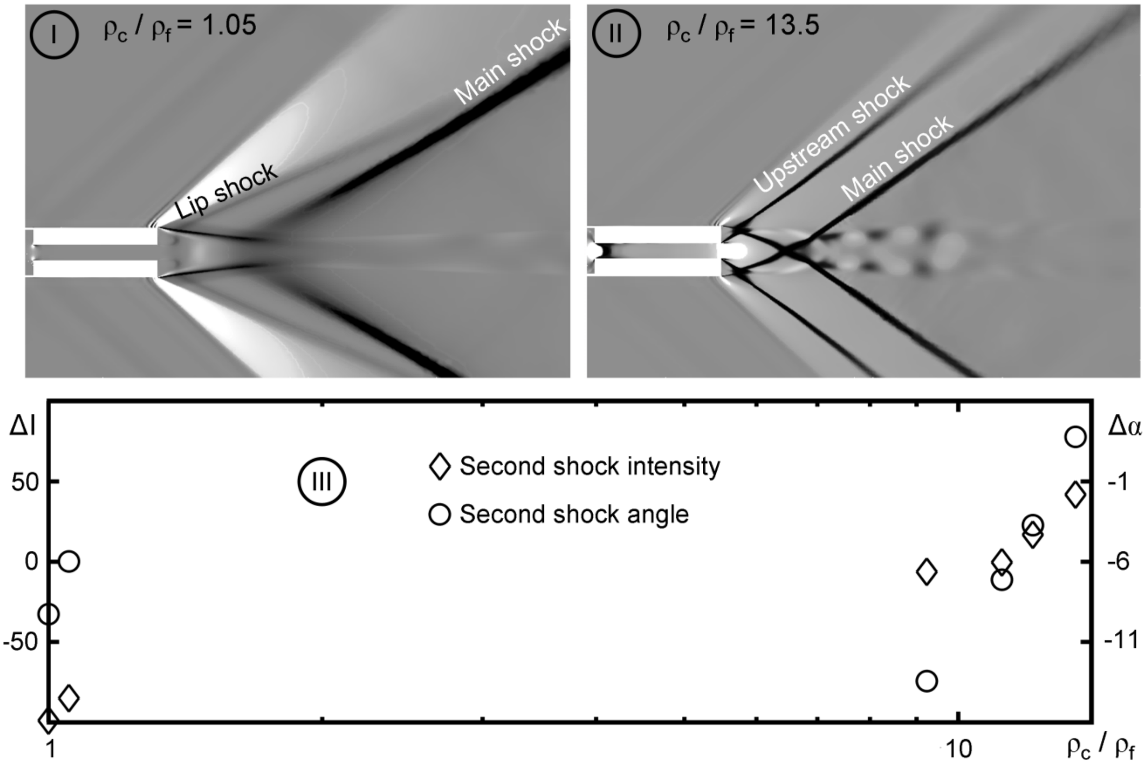

Fig. 3.6. I) Schlieren picture at ρ_c/ρ_f =1.05; II) Schlieren picture at ρ_c/ρ_f =13.5; III) Shock angle and intensity variation of secondary shocks in function of density ratio

Coolant jet Mach numbers exceeding the value of 2.5 (ρ_c/ρ_f = 8.3) led a distinctive trailing edge flow field. The growing coolant jet shear layers started to reshape the trailing edge shear layer. As a result, an additional compression corner was created shortly after the flow separation symmetrically on both sides of the trailing edge. This interaction resulted in a second pair of symmetric shock system, followed by a subsequent expansion, at 0.35d downstream of the trailing edge. Fig. 3.6-III reveals the strength and angle of the second shock system relative to the main trailing edge shock.

The compression across the upstream shock was similar, with limited downstream extension, to the main shock for lower density ratio but the strength increased with the purge rate. Eventually, the intensity of the secondary shock became higher that the main shock for ρ_c/ρ_f beyond 12.1. Consequently, the strength of the main shock reduces monotonically as most of the compression occurs on the upstream shock wave. Furthermore, the inclination of the first shock wave, which is initially 13 degree more oblique than the main shock, increases gradually until both shocks became parallel for the highest blowing. Whereas, the trailing edge shock keeps the position and inclination more or less steady for this range.

The previous analysis revealed a direct relationship between the shock properties and the base pressure. Fig. 3.7 presents the linear function between the shock intensity and the nondimensional base pressure. The highest base pressure resulted in the weakest trailing edge shock for the tested free stream conditions. Consequently, an active flow control technique serving to increase the base pressure will also contribute to reduce the trailing edge shock wave's intensity.

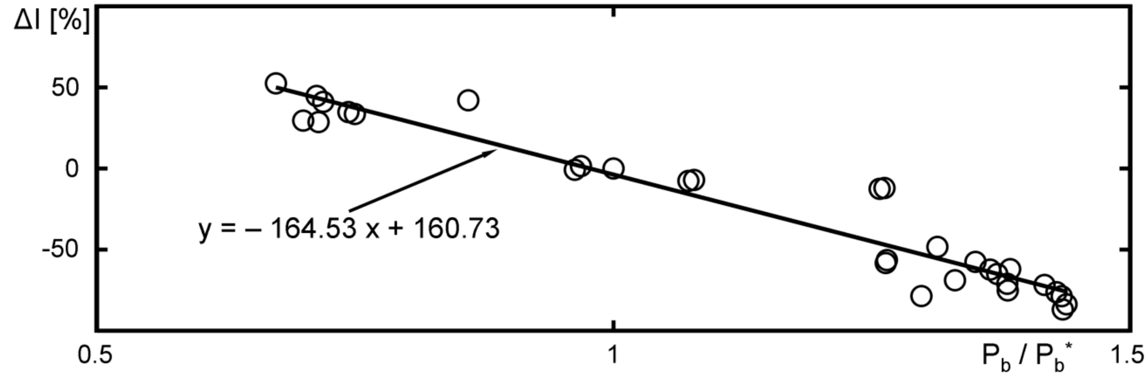

Fig. 3.7. Relative shock intensity variation in function of non-dimensional base pressure

3.2.2. Unsteady approach

The unsteady approach was used to extract the time-varying flow features and unsteadiness on the shock wave in the presence of the pulsating cooling. The time series of flow properties downstream of the trailing edge were extracted to resolve the coherent structures in the wake. The unsteady changes in the base pressure and shock wave were calculated. The sinusoidal pulsations with +/-40% amplitude were imposed around the steady cooling level which results in reduced shock wave intensities. The frequency of the pulsations was set to be 10 kHz, which significantly exceeds the vortex shedding frequencies of no cooling case (7292 Hz). Fig. 3.8 shows an instant from the unsteady flow field with the vortex shedding and oscillating shock structures.

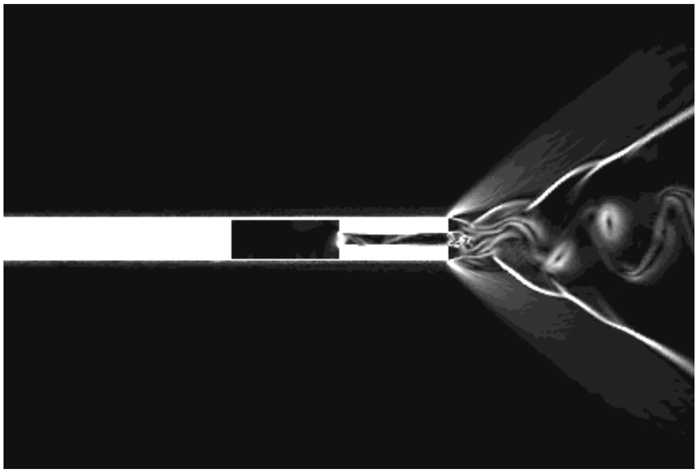

Fig. 3.8. Flow field of trailing edge exposed to pulsating cooling (density gradients).

It has been observed that the pulsating coolant resulted in reduced the mean base pressure, from the continuous blowing value, with 6% oscillations (Fig. 3.9). Fig. 3.10 shows the unsteady variation of the shocks intensities measured along the lines 2 to 5 trailing edge thickness above the top surface of the simplified geometry. The strength of the shock wave was affected the most in the near vicinity of the trailing edge. Further away, the amplitude of oscillations was significantly reduced.

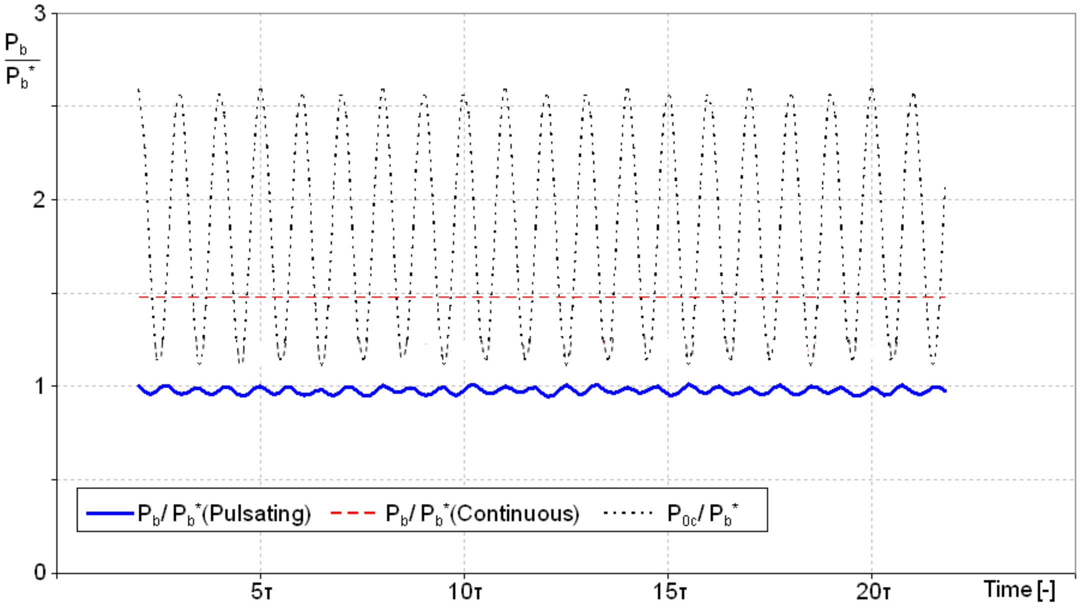

Fig. 3.9. Base pressure variation on blunt trailing edge for pulsating and continuous cooling cases along with coolant pulses.

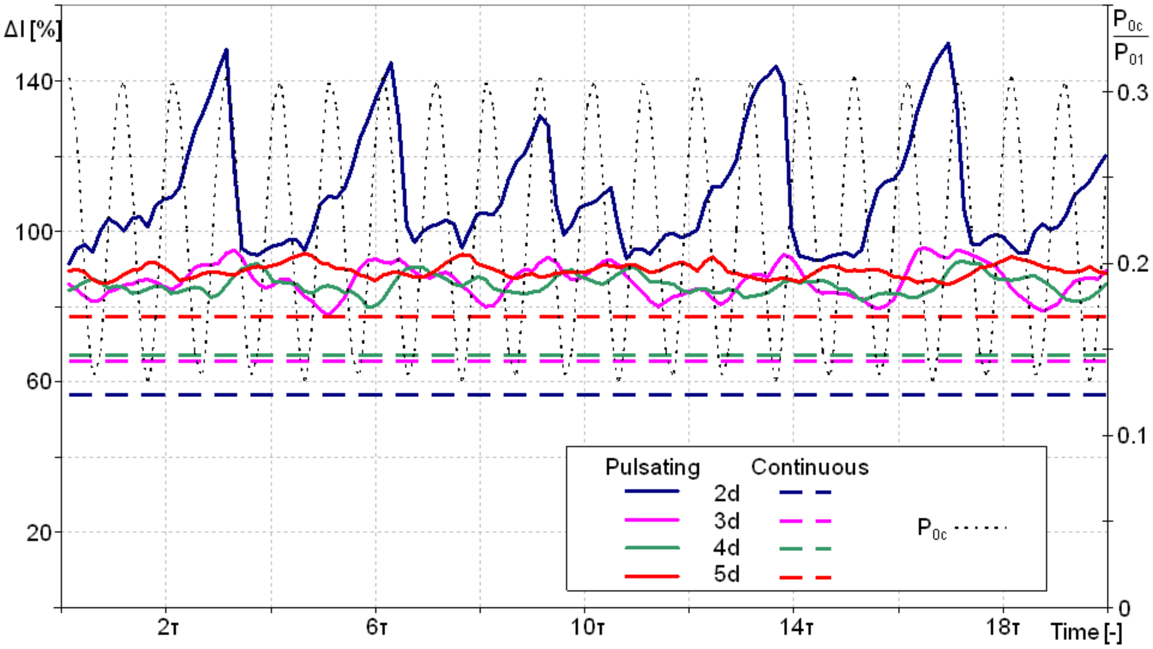

Fig. 3.10. Shock intensity variation on blunt trailing edge for pulsating and continuous cooling cases along with coolant pulses.

The variation in the shock inclination was also extracted from the numerical schlieren on both horizontal and vertical directions (Fig. 3.11). Both of the results showed similar trends. The shock was observed to be oscillating between 31 to 36 degrees with a fundamental frequency of 2.6kHz, similar to intensity variation.

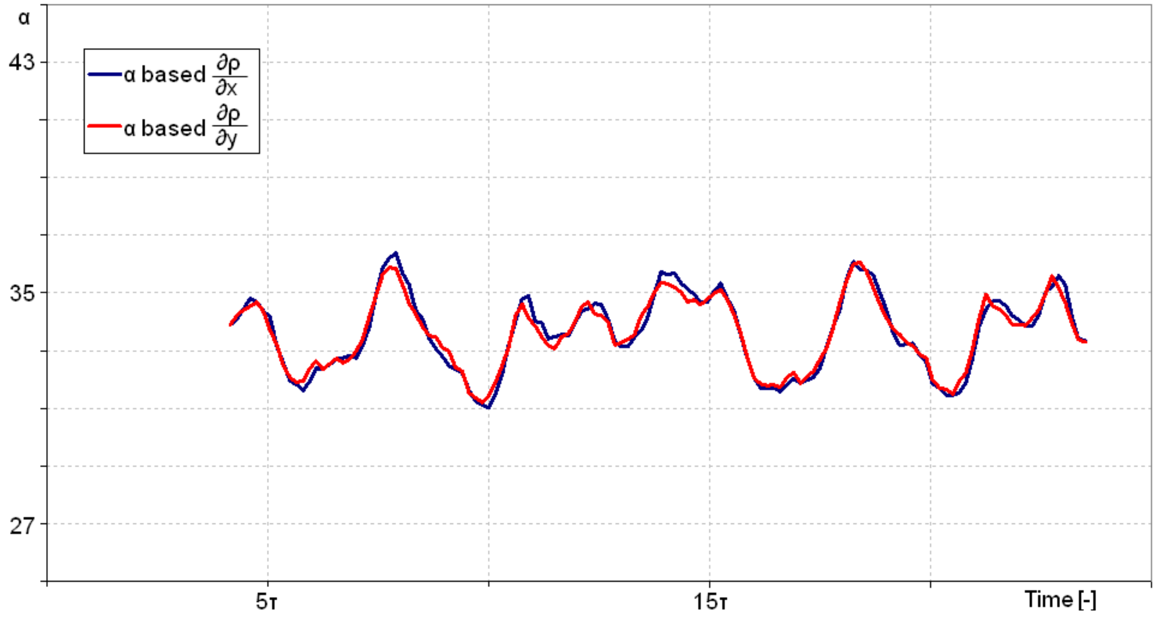

Fig. 3.11. Shock angle variation on blunt trailing edge for pulsating cooling.

The spectral analysis of the flow downstream of the trailing edge was made on the pressure signal extracted from 6 different points as depicted in Fig. 3.12. The detected frequencies are summarized in Table 3.1.

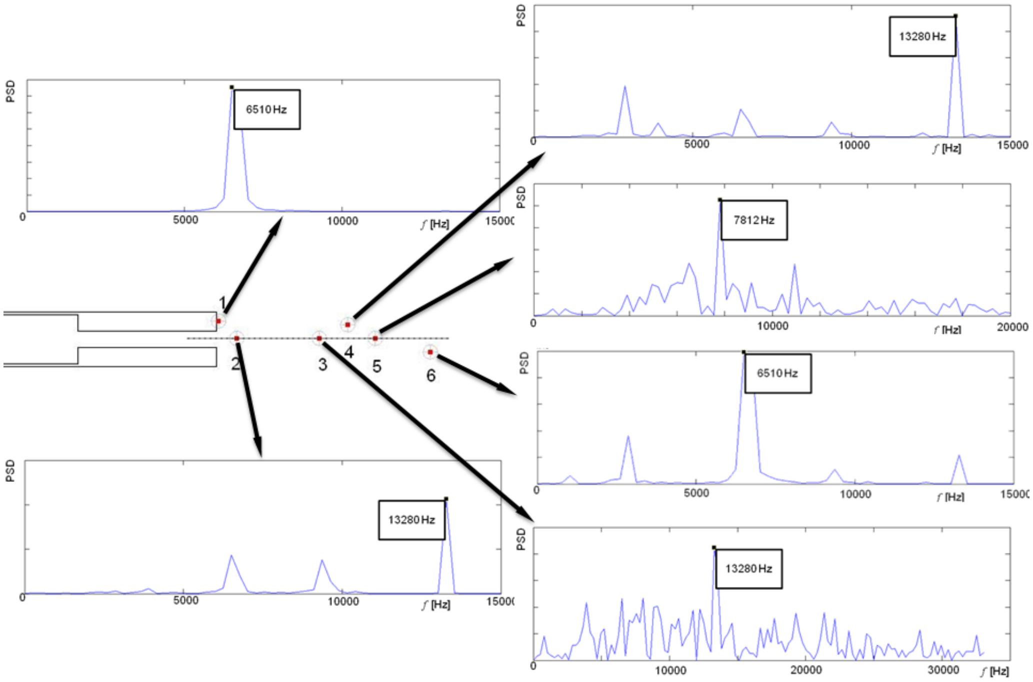

Fig. 3.12. The spectral analysis of the base and wake flow.

The spectral analysis detected several dominant frequencies on the wake and the shock wave property variations, implying a complex shedding pattern with multiple modes. However, the frequency of 6510 Hz was detected at various amplitudes in each spectrum. Moreover, the spectra lacked the pulsating frequency (10 kHz) which might be due to attenuation of high pulsation frequency in the cooling channel and consequently affecting the wake at other frequencies.

Table 3.1. Main frequencies in the flow field of blunt trailing edge with pulsating cooling

	1^{st} frequency		*2^{nd} frequency*		*3^{rd} frequency*	
	f[Hz]	*St*	*f[Hz]*	*St*	*f[Hz]*	*St*
Point 1	*6510*	*0.227*	*-*	*-*	*-*	*-*
Point 2	*13280*	*0.462*	*6510*	*0.227*	*9375*	*0.326*
Point 3	*13280*	*0.462*	*6510*	*0.227*	*8073*	*0.281*
Point 4	*13280*	*0.462*	*2865*	*0.100*	*6510*	*0.227*
Point 5	*7812*	*0.272*	*10940*	*0.381*	*6510*	*0.227*
Point 6	*6510*	*0.227*	*2865*	*0.100*	*13280*	*0.462*
Δl	*2604*	*0.091*	*6771*	*0.236*	*9375*	*0.326*
$\Delta\alpha$	*2604*	*0.091*	*6771*	*0.236*	*-*	*-*

3.3. Circular trailing edge

3.3.1. Steady approach

Following the analysis carried out on the simplest blunt trailing edge geometry, circular trailing edge model, which can be resembled with the turbine airfoil trailing edge, was numerically tested. For the free stream M=1.5 simulations, the steady analysis covered coolant blowing rates in the lower range of density ratios (no blowing, 1.09, 1.18, 1.39, and 1.76) where the highest reduction in shock intensity was observed for blunt trailing edge. To understand the effect of the cooling on the trailing edge shock waves formed at different Mach number, the analysis covered the simulations of the no blowing and density ratio of 1.6 for M=1.2 which were later tested experimentally.

The circular trailing edge exhibits very similar flow field to the blunt configuration. Fig. 3.13 depicts the main flow features of the trailing edge flow at M=1.5 stream in absence of flow discharge. The expansion fan is observed over the circular part of the trailing edge followed by shear layers enclosing the base region. The weak lip shocks are created right upstream of the flow separation. At the point of confluence where the wake is formed, the main trailing edge shock waves are created.

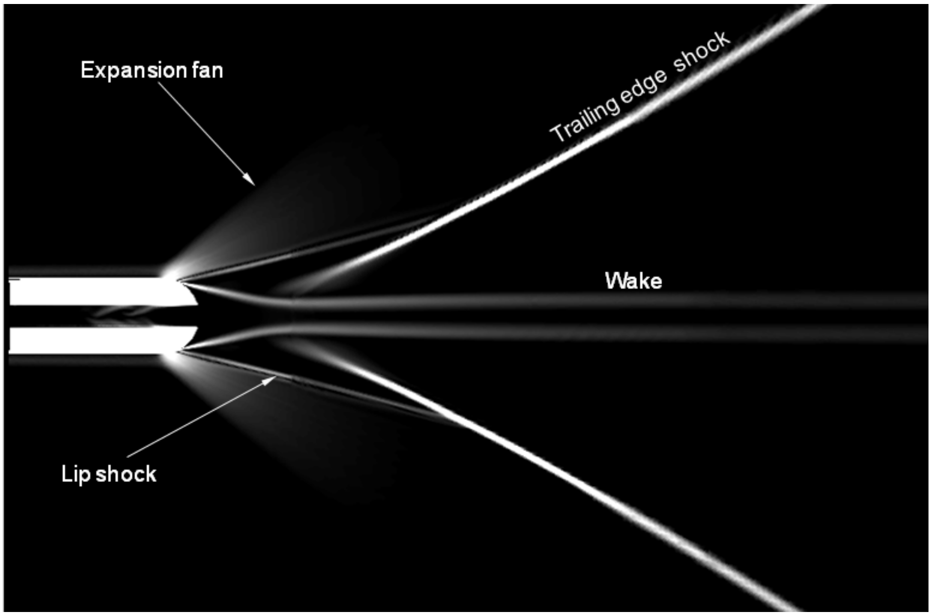

Fig. 3.13. Circular trailing edge flow field exposed M=1.5 flow without blowing.

The introduction of the trailing edge discharge results in certain modifications in the base region and downstream flow field (Fig. 3.14 and Fig. 3.15). There is a strong similarity with the blunt trailing edge flow field evolution by increasing discharge rate. As the coolant was introduced, the recirculation bubbles moved downstream and reduced the shear layer inclination (Fig. 3.14-a). Meanwhile the cooling penetrated into the base region and increased the base pressure. Further increase in the purge rate pushed the bubbles further downstream, the size of the structures was reduced and a second set of recirculation was created close to the trailing edge surfaces on both sides (Fig. 3.14-b). The downstream recirculation was completely disappeared with increased cooling (Fig. 3.14-c and Fig. 3.14-d), similar to the blunt trailing edge (Fig. 3.4-c). The shear layers were further flattened leading weaker compression on the wake. Fig. 3.14-d shows creation of vortex couples on both sides of the trailing edge with increased discharge as observed in blunt trailing edge.

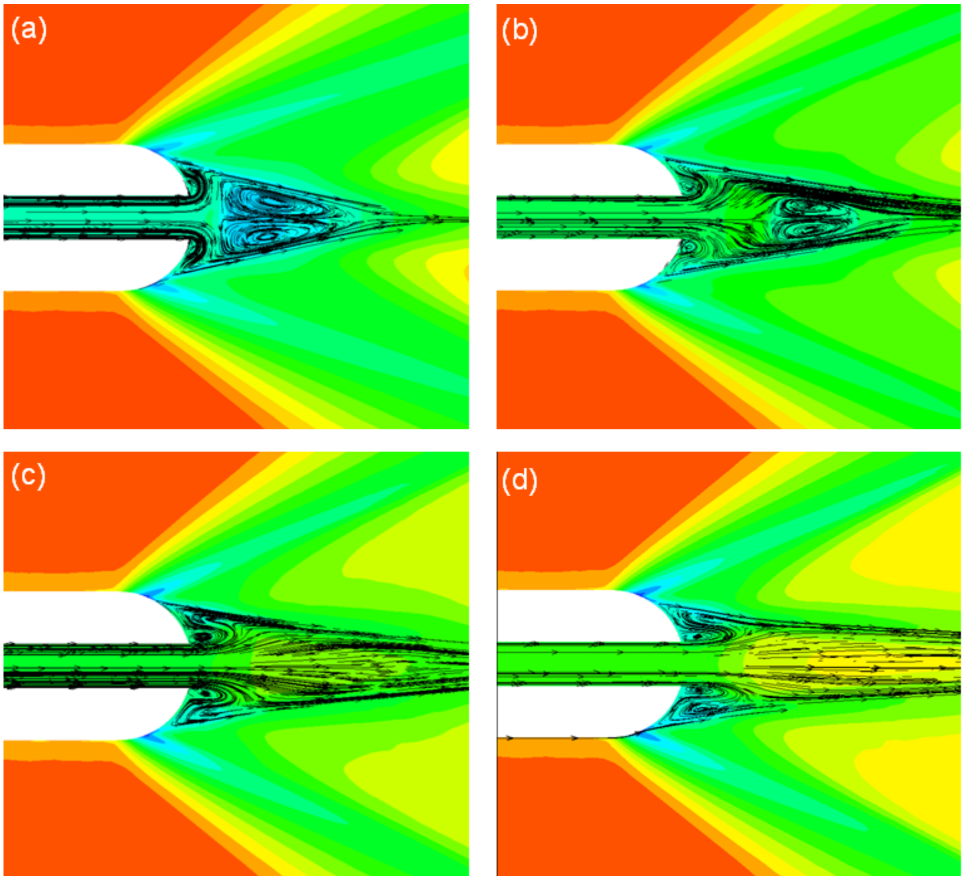

Fig. 3.14. Streamlines on top of the pressure contours (a) ρ_c/ρ_f=1.09 (b) ρ_c/ρ_f=1.18 (c) ρ_c/ρ_f=1.39 (d) ρ_c/ρ_f=1.76

The numerical Schlieren images revealed the effect of the coolant rate on the shock wave structures (Fig. 3.15). For the lower amount of cooling, the shear layers were observed to be flattened and lip shock angle was increased (Fig. 3.15-a and Fig. 3.15-b). Moreover, the further increase in cooling mass flow resulted in a significant reduction in the shear layer angle (Fig. 3.15-c and Fig. 3.15-d). The trailing edge shock waves moved upstream and the lip shocks merged into the main shocks.

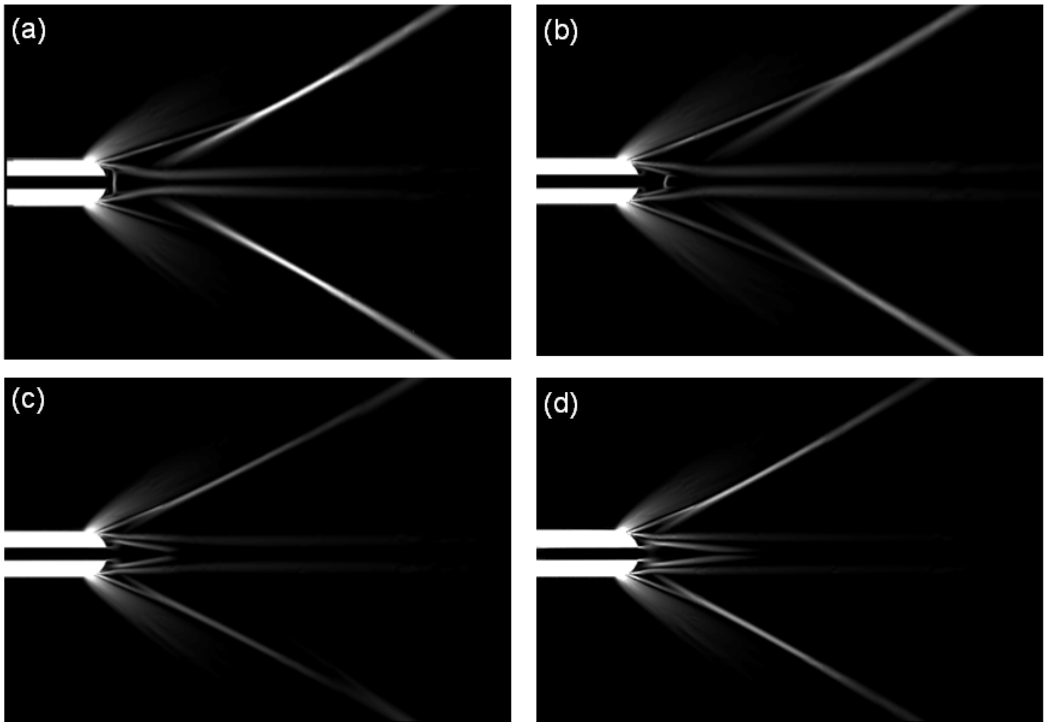

Fig. 3.15. Density gradient contours (a) $\rho_c/\rho_f = 1.09$ (b) $\rho_c/\rho_f = 1.18$ (c) $\rho_c/\rho_f = 1.39$ (d) $\rho_c/\rho_f = 1.76$

Following the analysis on the blunt and circular trailing edge geometries exposed to the high free stream Mach number flow, the cooling effects on the shock waves and trailing edge flow has been simulated at lower Mach number (M=1.2) for no blowing and mild discharge (ρ_c/ρ_f=1.6) which felt in the cooling range resulting in significant reduction in shock intensity. The same methodology used in other test cases was applied to understand the cooling effects at the low Mach number. The purge at low rates also resulted in a considerable reduction (86.7%) in shock intensity, as noticed in M=1.5 cases, with 18.5% increase on base pressure. The summary of the steady characterization of the shock intensity variation for all geometries and Mach numbers are given in Fig. 3.16. The reduction on the shock wave strength has been attained regardless of the trailing edge geometry and the Mach number with moderate cooling rates. The base pressure augmentation and the shear layer flattening induced by the trailing edge cooling at such rates emanated reduced compression at the trailing edge and hence alleviated the impact of the shock waves.

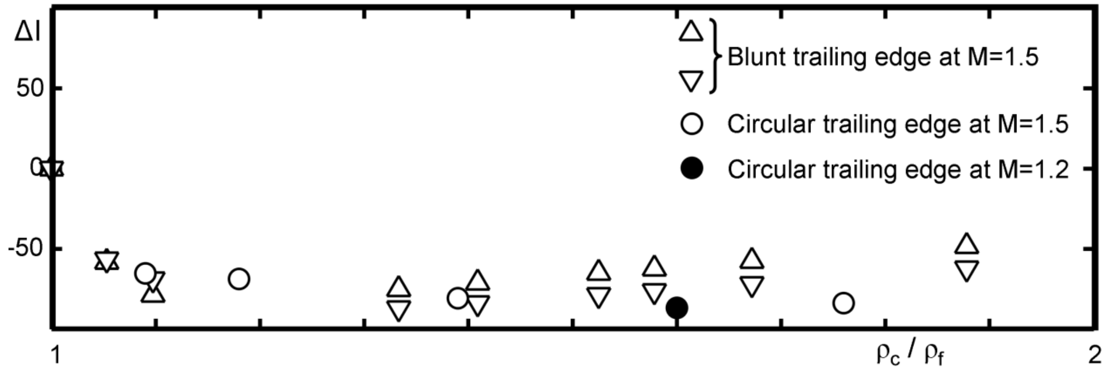

Fig. 3.16. Shock intensity variation on square and circular trailing edge at M=1.5 and 1.2.

3.3.2. Unsteady approach

3.3.2.1. Continuous cooling

The unsteady analysis of the circular simplified trailing edge geometry was performed to understand the wake unsteadiness, the effects of continuous and eventually the pulsating cooling. The simulations were performed at M=1.2 free stream condition. The continuous cooling was provided at the same rate of the steady analysis ($\rho_c/\rho_f=1.6$). The unsteady pressure data was extracted at the same locations on the wake to resolve the vortex shedding from the trailing edge. The shock wave properties were also unsteadily extracted.

An increase of 18% in base pressure was observed from the no blowing value with less than 1% unsteady variation. The increase in the base pressure is resulted in an average decrease in the shock intensity by 44%. When the FFT analysis was carried out on the 6 measurement points, a common frequency of 7292 Hz was found to be the most dominant peak in the spectrum. By taking into account the other variables (trailing edge thickness and flow velocity), the corresponding Strouhal number was found to be 0.317. The same peak was also captured in the shock intensity frequency spectrum, showing that the wake unsteadiness induces small amplitude oscillations on the shock waves. A snapshot of the flow field is shown in Fig. 3.17. The wake oscillations were created in the form of a weak vortical structures which started to appear 2d downstream of the trailing edge as depicted. This might be due to the breakdown of the base region and dilatation of the confluence point downstream by the low amount of cooling. The trailing edge shock formed 0.5d downstream with lambda structure.

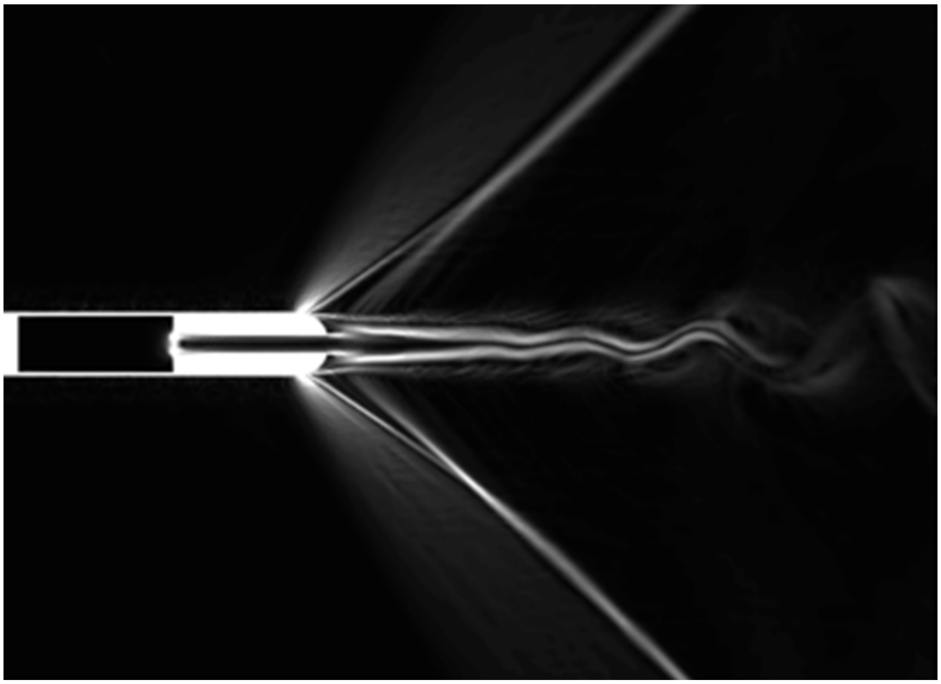

Fig. 3.17. Density gradient contours for M=1.2 main flow with ρ_c/ρ_f=1.6 cooling

3.3.2.2. Pulsating cooling

The sine wave oscillations were added to the mean level of continuous cooling. The amplitude of the oscillations was set to be 40% and 80% with a pulsation frequency of 200 and 1000 Hz around the mean value. The attributes of the flow parameters were analyzed for these 4 test conditions to comprehend the consequences of the pulsation parameters, i.e. frequency and the amplitude.

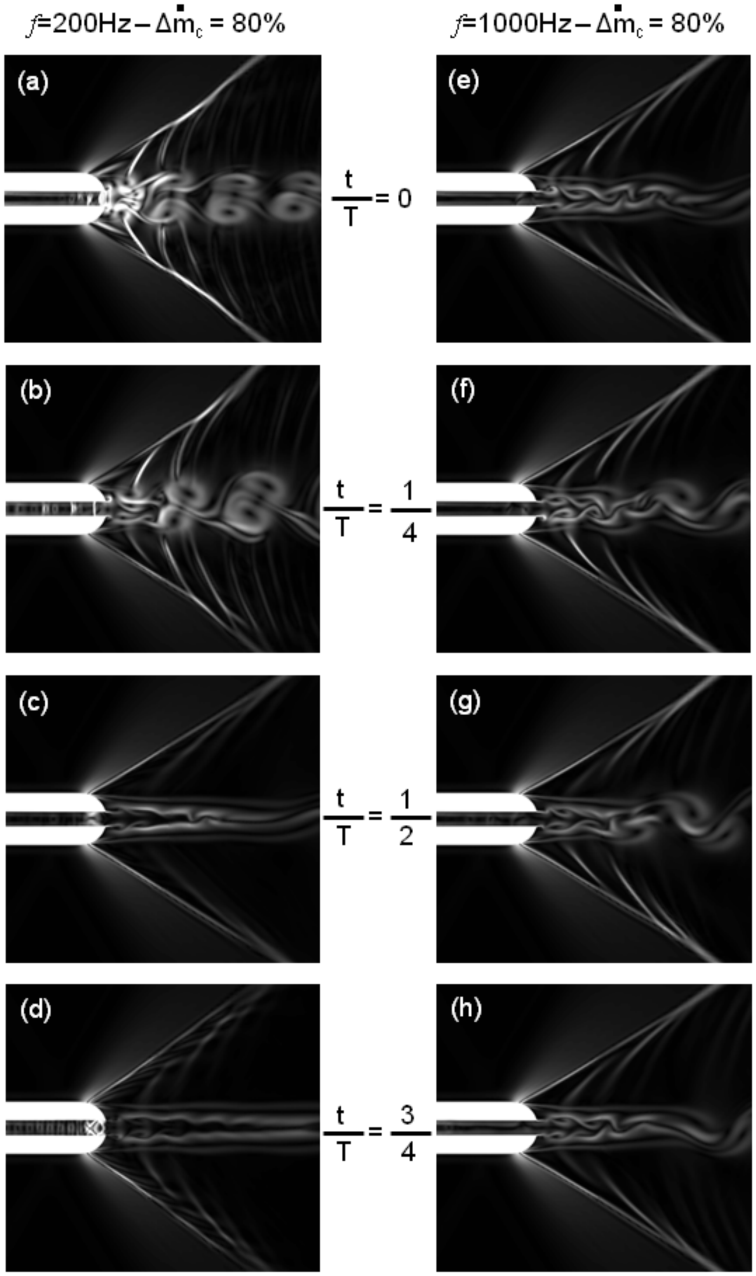

Fig. 3.18. Density gradient contours at every quarter of pulsation periods

The detailed trailing edge flow field at every quarter of a pulsation period (T) is presented in Fig. 3.18. The first (t/T=0) and the third (t/T=0.5) instants correspond to the maximum and minimum mass flow at the cooling channel exit, respectively. On the first half of the pulsation period, vortex structures shed from the trailing edge. The patterns of shedding were different from von Karman vortex shedding, as observed by Gostelow et al. [116]. At the peak blowing, the vortices were shed as symmetric pairs and then they started to shed alternately. At this instant, the propagated vortices tended to grow whereas the size of the propagating vortices kept their size on the maximum blowing. The decrease phase of the cooling (Fig. 3.18-b) had destabilizing effect on the wake unsteadiness whereas the increase phase had a stabilizing effect as observed for both pulsation frequencies (Fig. 3.18-c, d, g and h). The vortex shedding tended to disappear on the minimum and following increase phase for both frequencies. Therefore, the dominant parameter affecting the wake can be said the mass flow variation rather than the absolute value of cooling. This behavior was also detected in the unsteady pressure traces which were recorded at three locations in the wake along with the coolant outlet mass flow, as depicted in Fig. 3.19.

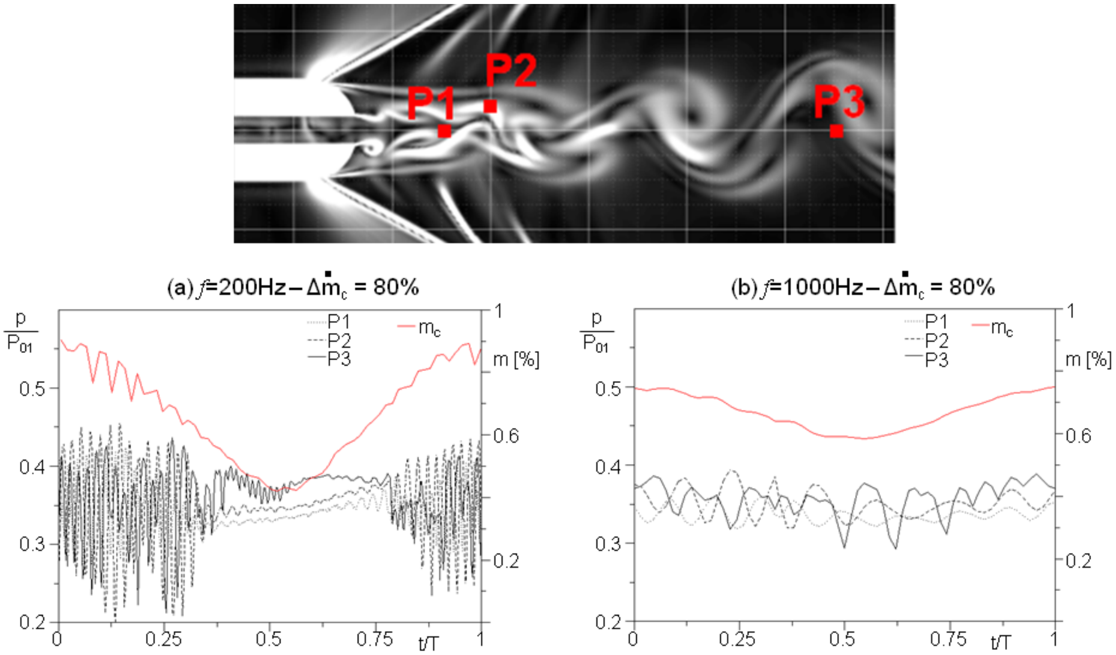

Fig. 3.19. The unsteady pressure at the wake

For the 200Hz blowing the mass-flow oscillations had larger amplitude and the vortex shedding was almost suppressed during the minimum coolant ejection. The vortex formation was indeed more evident in the lowest frequency case. The simulations confirmed that at high frequency the range of variation in mass-flow was attenuated at the coolant exit.

The base pressure and the shock intensity traces were also investigated to figure out the impact of coolant pulsations (Fig. 3.20). High amplitude base pressure fluctuations observed for the low frequency case (Fig. 3.20-a) were caused by the strong vortex shedding arising between *t/T ~ 0.75* and *t/T ~ 0.3* (Fig. 3.18 – a to d and Fig. 3.19-a). The large variation in coolant mass-flow resulted in a time interval of more stable base pressure in the remaining part of the period. Nevertheless, no linear relationship between the base pressure and the purge rate has been noticed for the pulsation cooling scheme. The base pressure (Fig. 3.20-a) and the shock intensity (Fig. 3.20-c&d) was observed to be ahead of the mass flow fluctuations, as in this case base pressure started to increase before the coolant mass-flow started to augment. The higher pulsation frequency also inhibited the base pressure deviations from the mean value. Only small fluctuations were observed which are in accordance to the mild vortex shedding formation (Fig. 3.18 – e to h. and Fig. 3.19 – b). The time-averaged base pressure levels showed that higher frequencies result in lower base pressures (4.5% of no blowing base pressure). Increase in the pulsation amplitude led to 4.5% higher base pressure for both frequencies. Hence, pulsating coolant with specific frequency and amplitude could provide a base pressure variation similar to the one obtained by continuous cooling at higher mass-flow. Since base pressure loss is inversely proportional with the base pressure level, lower pulsating frequencies with high amplitudes might result in lower base pressure losses.

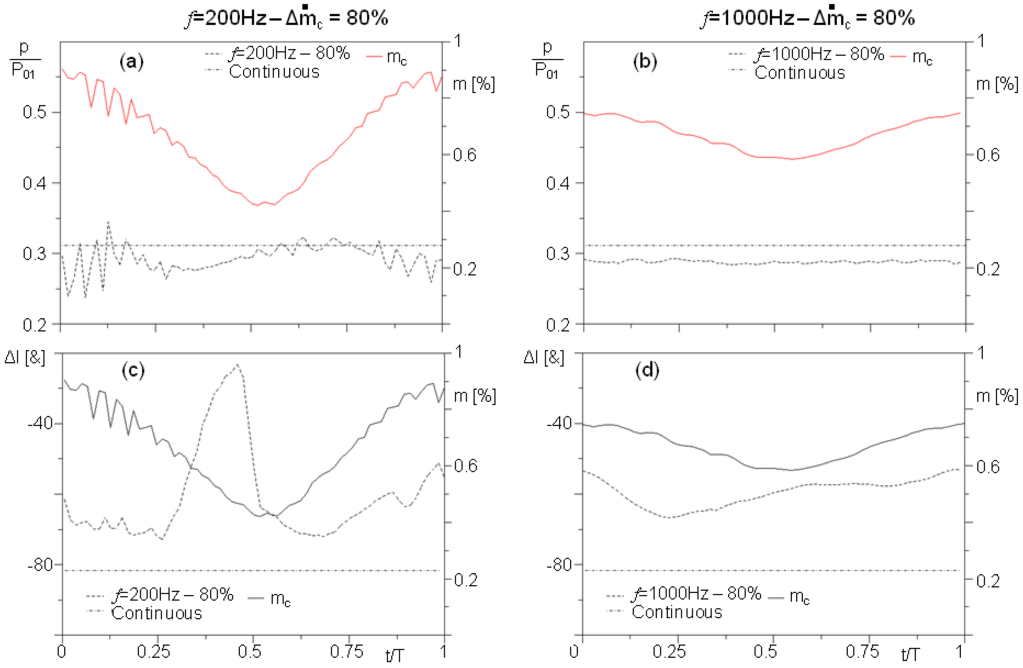

Fig. 3.20. The base pressure and the shock intensity variations over a period of pulsation

Fig. 3.20-c&d reveals the dependency of the shock intensity variation in time on coolant pulses. Higher pulsation frequency resulted in lower variation in the shock intensity. The instantaneous strength of shock was not driven by the instantaneous mass-

flow as observed in the continuous cooling. For the 200 Hz coolant pulses with 80% amplitude (Fig. 3.20-c), the shock intensity has reduced by only about 23% at the instant of minimum mass-flow (~ 0.45%). Hence, the shock at this blowing rate was stronger than the shock at higher blowing rate. The shock intensity variation with pulsating discharge did not follow the correlation between the shock intensity and continuous cooling. The steady cooling mass-flow rate of ~ 0.45% resulted in relatively lower shock intensity than with higher mass-flow rates. Therefore, the way pulsation affects the shock cannot indeed be explained only by the absolute level of coolant ejected rate. The flow field was rather dictated by the gradient of coolant mass-flow at the slot exit. For both frequencies, the shock intensity reaches its minimum at half of the mass-flow descending slope, while it is highest around the position of minimum blowing. Furthermore, time-averaged analysis of the shock properties showed that the high frequency and high amplitude pulsations resulted in lowest average shock intensity (-60%). Yet, the minimum time averaged shock wave intensity was observed for the continuous cooling (-82%). The shock angle variation reduces, from the maximum 13.3^{o} observed for pulsations at 200 Hz with 80% amplitude, with increasing pulsation frequency and decreasing amplitude. The effect of decreasing frequency is that of exalting shock modulation. Notwithstanding this variation, the pulsation always provides an average more inclined shock. However, the value of shock reduction with continuous coolant is never reached throughout all pulsating cases.

4

Shock Modulation on the Flow Passages

4.1. Introduction

Trailing edge shock interactions are one of the major sources of losses in supersonic airfoils. Additionally, vane shocks cause large pressure fluctuations that may result in low and high cycle fatigue problems. Previous research related to the present investigation may be classified in four topics: trailing edge shock wave interactions, base pressure losses, trailing edge vortex shedding, and effects of the coolant ejection.

The downstream flow field of nozzle guide vanes in modern high pressure turbines suffers fish tail shock structures [117]. The impingement of those compression waves on the downstream rotor row and rear suction side of the adjacent vane results in unsteady entropy generation. Quantification of unsteady loss and pressure variation in a transonic turbine was studied numerically and experimentally in the literature [102]. The increase in vane outlet Mach number from 1.07 to 1.24 reduced the overall turbine efficiency 5% and increased the unsteady forcing on the rotor crown 3.6%.

Regarding the base pressure losses, Gostelow et al. [118] analyzed computationally and experimentally the trailing edge structure and the related losses on a transonic turbine cascade. Substantial increase in the base pressure loss accompanied by an increase in wake mixing loss was reported for exit Mach number around unity. For the exit Mach number between 0.8 and 1.2, the base pressure coefficient diminished as low as 3.5 times of its value out of the transonic range. The wake mixing loses were doubled at sonic outlet flow. Uzol et al. [19, 119] documented the performance of different trailing edge geometries. Schobeiri and Pappu [120] found an optimal geometry and blowing ratio that minimize the mixing losses of cooled gas turbine blades. Their experimental and numerical studies demonstrated that the ejection velocities similar to the main flow velocity resulted in the minimum mixing losses regardless of the airfoil geometry. The losses were minimized by increasing the slot opening parallel to the demand for cooling rate. Sieverding et al. [99] determined an experimental correlation of the base pressure in function of the downstream static pressure, which allows accurate predictions of base pressure losses.

Concerning the vortex shedding, Rowe et al. [121] observed that a thick boundary layer upstream of the trailing edge reduced the shedding frequency, resulting in decreased base pressure losses. Increasing the boundary layer shape factor caused an inverse trend on the parameters. Sieverding and Heinemann [122] demonstrated the influence of the boundary layer state on both pressure and suction sides on the vortex shedding. They observed a change in the boundary layer state on both sides of the trailing edge from turbulent to laminar resulted in a reduction of Strouhal number. For the cases with mixed boundary layer states on both sides of the trailing edge, intermediate Strouhal numbers were observed. In such circumstances, a wider power distribution around the vortex shedding frequency was noticed on the spectra. Furthermore, the experiments made on a flat plate revealed the 3D behavior of the unsteady base flow and, the vortex street exhibited a 2D structure only in the midspan region [123]. Cicatelli and Sieverding [124] characterized experimentally the time averaged and unsteady pressure field in the base region.

Studies on the effect of coolant ejection on the vortex shedding were presented by Motallebi and Norbury [23] based on Schlieren images of the vortices shed from a blunt trailing edge at subsonic and supersonic conditions. The minimum base pressure levels were attained in the transonic range with highest Strouhal numbers. A certain rise in the base pressure was noticed corresponding to a moderate coolant flow rate by shifting the vortex formation location downstream. The disappearance of the trailing edge vortex motion was observed over a range of bleed air mass flows following the value producing a maximum level of base pressure. The high discharge rates caused formation of two different regimes of vortex formation, exhibited substantially high Strouhal numbers, on both sides of the trailing edge with significant reduction in base pressure. Such effect of cooling was more effectively observed for low supersonic range. However, the base pressure augmentation outcome of small amount of cooling was attenuated. Sieverding [20] experimentally showed that a higher base pressure and a variation in the trailing edge shock angle corresponded to a moderate coolant flow rate. The detailed measurement on both sides of the cooling slot exhibited a uniform distribution on the base pressure. Raffel and Kost [21] gathered similar results at supersonic conditions using PIV data over a narrower range of cooling rates. The pressure measurements pointed shock wave attenuation for low amount of cooling ejection. Saracoglu et al. [22] obtained analogous conclusions using numerical simulations on a blunt trailing edge at an outlet Mach equal to 1.5, the shock strength was mitigated 70% at moderate trailing edge cooling compared to the no blowing case.

Pulsating coolant has recently been investigated in turbomachinery to improve film cooling performance and control separation. Rutledge et al. [125, 126] experimentally investigated the effects of pulsating cooling on the heat transfer characteristic over a cylindrical leading edge model with flat after body, which mimics turbine blade leading edge. Pulsating cooling at low frequencies was found to be promising to improve the film effectiveness. Rutledge et al. [127] performed numerical simulations of a similar test setup with pulsating leading edge cooling. A small reduction in heat transfer coefficient was observed for lower frequencies. El-Gabry and Rivir [128] compared the continuous and pulsating (10 Hz with 50% duty cycle) cooling on a cylindrical leading edge model. The film effectiveness was halved for the pulsed flow. Nevertheless, Ekkad et al. [129] obtained promising results in their experiments performed on a bluff body equipped with leading edge pulse cooling at several frequencies and duty cycles. The film effectiveness was improved regardless of pulsating frequency. Whereas, higher cooling effectiveness and lower heat transfer coefficients were achieved with reduced duty cycles. No difference was detected for the frequencies below 20 Hz mainly due to experimental uncertainty.

Volino and Ibrahim [130] and Volino et al. [36] performed experiments on a LPT blade exposed to pulsed suction surface ejection with various duty cycles. The results verified superiority of the pulsed cooling on inhibiting separation and increasing the performance of the airfoils. Sondergaard et al. [30], Bons et al. [39, 131] and Woods et al.

[132] experimentally achieved the effective boundary layer separation control by using pulsed jets at various frequencies, duty cycles and orientation.

Published research has demonstrated that cooling ejection has significant effects on the base region and trailing edge shock patterns. The originality of this work lies in the use of pulsating coolant to control shocks for the first time in the literature. Experimental and numerical research have been performed to understand the base region flow topology depending on cooling ejection rates. Several correlations for the base pressure, shock angle and vortex shedding are presented. The final goal of the research is to improve turbine durability and efficiency in compact supersonic turbomachinery. This study may guide aerodynamic designers towards novel concepts to modulate shock waves.

4.2. Operating conditions

The tests were made for a range of high subsonic to low supersonic Mach numbers ($M_{2,is}$=0.8-1.2), while 2 Reynolds numbers have been selected (Re=$4x10^6$ & $6x10^6$). All conditions were tested for no blowing and continuous blowing at 1.1, 1.5 and 1.9 bars of coolant total pressures (P_{0cool}). A pulsating coolant stream was introduced for transonic and supersonic test cases at an average coolant total pressure of 1.9 bars with a frequency of 200 Hz resulting in a 12% fluctuation of the mean coolant mass flow.

4.3. Airfoil loading

The analysis of the time-averaged pressure was performed to characterize the flow field aerodynamics in the cascade passage and the downstream planes. The pressure values are represented in terms of isentropic Mach numbers ($M_{is} = \sqrt{\left(2/(\gamma-1)\right)\left(\left(P_{01}/P_s\right)^{(\gamma-1)/\gamma}-1\right)}$). Fig. 4.1 depicts the distributions with respect to normalized surface coordinate (S/S_{max} equals 0 at the leading edge and one at the trailing edge) on the upper flow passage for each test condition and for each coolant blowing pressure.

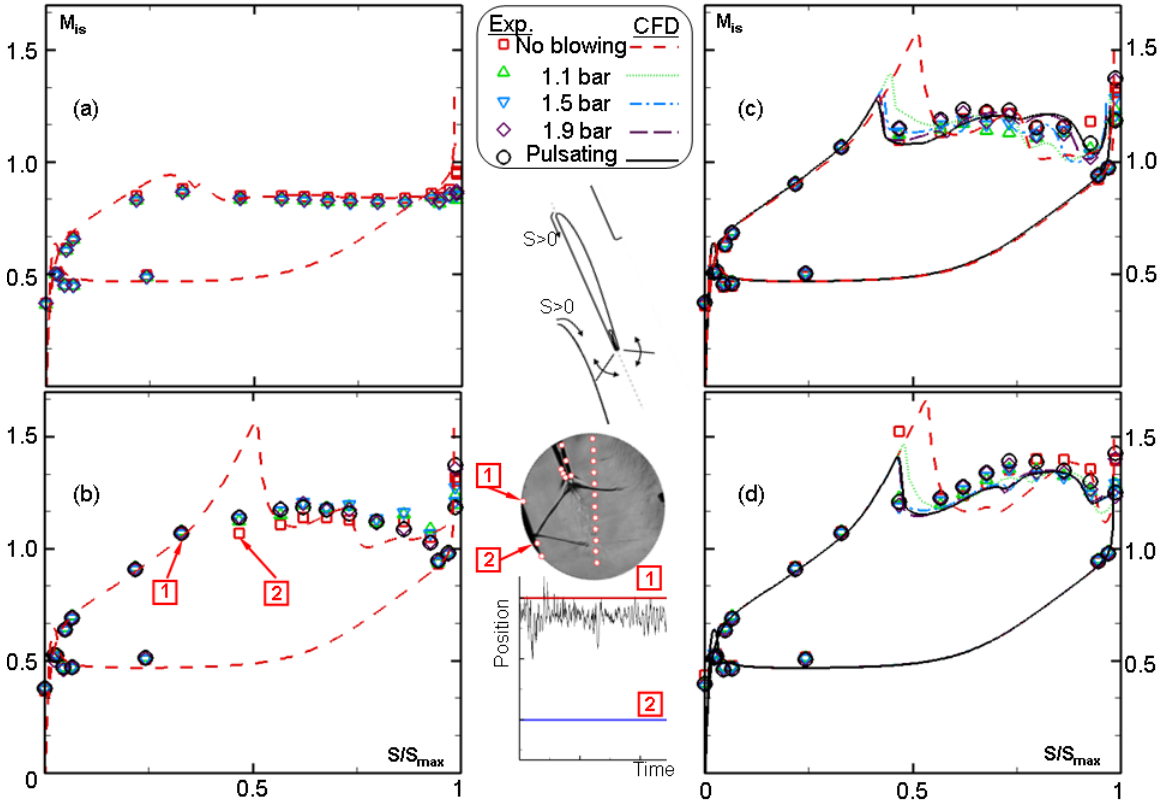

Fig. 4.1. The variation of velocity distribution of upper channel a) $M_{2,is}$=0.8, Re=4x10^6; b) $M_{2,is}$=1.1, Re=4x10^6; c) $M_{2,is}$=1.1, Re=6x10^6; d) $M_{2,is}$=1.2, Re=6x10^6

In Fig. 4.1-c we observe a large acceleration along the suction side in the leading edge region. From S/S_{max} 0.05 to 0.3 (throat), there is a constant acceleration. Downstream of the throat the flow overaccelerates due to the expansion fan until the impact of the right running shock. After the deceleration caused by the shock wave, the flow keeps on accelerating downstream. The cooling scheme does not alter the pressure distribution around the profile for the cases below sonic speed. For supersonic outlet conditions, the coolant affects only the region downstream of the shock impingement. The behavior is not visible in the experimental results due to the fact that the impingement location of the shock wave statistically lies between two measurement locations denoted as 1 and 2 in Fig. 4.1 as revealed from the processing of Schlieren pictures. The CFD reveals an upstream displacement of the shock impact with the coolant mass flow. The increase of Mach number to 1.2 results in a substantial increase in the passage loading. One can also observe that the pulsating cooling results in lower loading than the continuous blowing.

4.4. Downstream static pressure

The pressure distributions on downstream measurement plane provided an exact location of the left-running shock. Fig. 4.2 represents the downstream isentropic Mach numbers for supersonic conditions together with corresponding Schlieren images to illustrate the orientation of the left-running shock wave with respect to the measurement locations. The effect of the right running shock reflection from the adjacent suction side can be seen at pitch-wise locations between g/g*=1.35 and g/g*=1.5. For $M_{2,is}$=1.1 and Re=4x10^6, the pressure increase downstream of the right running shock reflection is reduced when the coolant is introduced. A similar effect is observed for the other cases as well. One can also notice that the shock wave is less oblique for $M_{2,is}$=1.2 and Re=6x10^6 when the coolant is introduced.

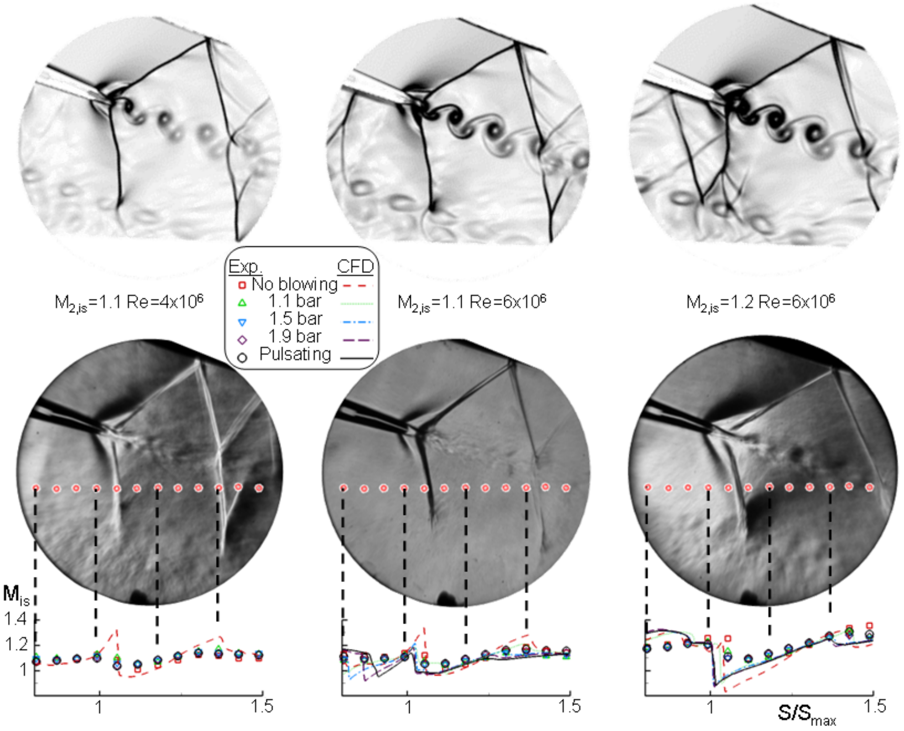

Fig. 4.2. Pitch-wise pressure distribution downstream of the cascade for all test conditions

4.5. Shock angle fluctuations

The analysis of the shock angle movement is based on the numerical and experimental Schlieren. Regarding the uncooled case, the shock angle varies between 55 to 60.5 deg. at the vortex shedding frequency (about 20 kHz). The use of pulsating cooling implies variations of about 5 degrees at the pulsating coolant frequency (about 200 Hz). Fig. 4.3 compares the power spectrum of the unsteady shock wave angle (α) with the valve encoder and the pressure sensor in the cooling slot (P_{scool}). It is clear in both figures that the pulsating cooling at 208 Hz is altering the shock angle at exactly the same frequency.

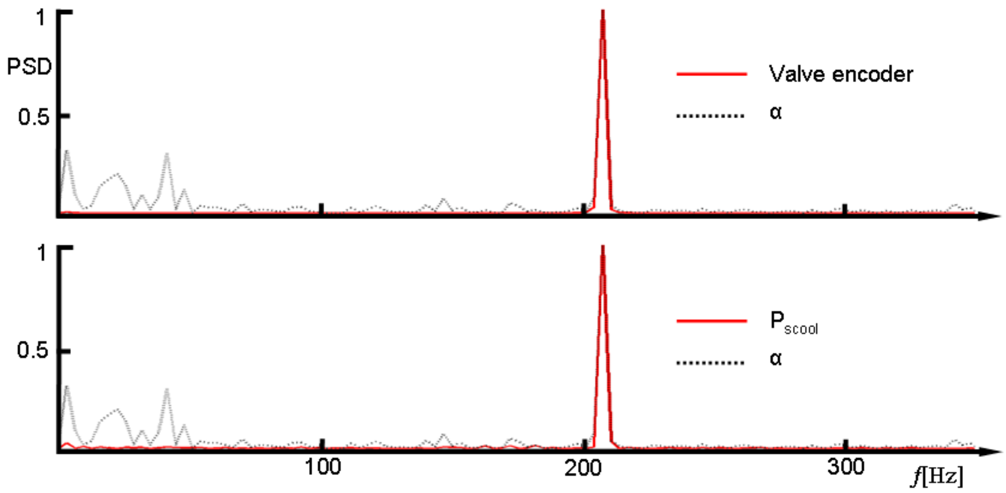

Fig. 4.3. Comparison of the experimental power spectrum of the shock wave angle variation with: Encoder delivering one pulse per revolution (top); high-frequency pressure sensor in the cooling slot (bottom)

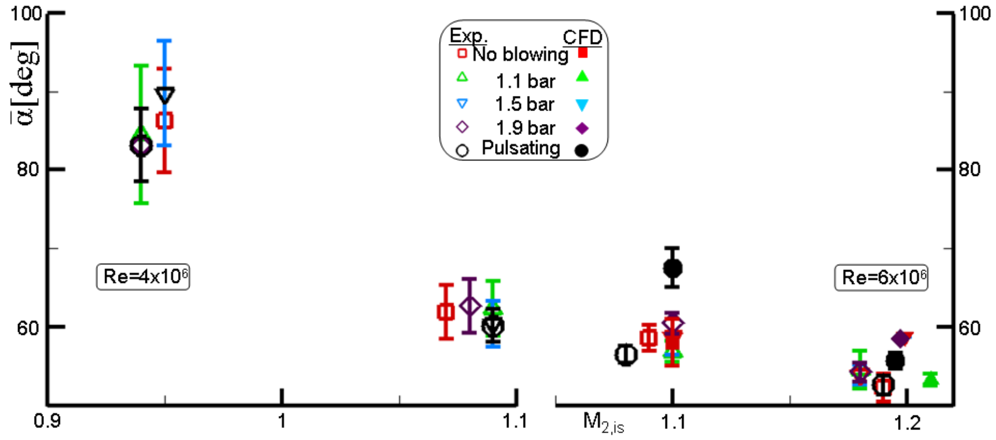

Fig. 4.4. Schlieren results: average angles with error bar (RMS) for all conditions

In Fig. 4.4, the average angle variation obtained by the Schlieren image analysis is presented together with the corresponding RMS values. The mean angle and the variability of the shock waves are reduced by increasing the Mach number. Furthermore, increasing Reynolds number provide a stabilizing effect, or reduction of RMS, on the shock angle. The average shock angle and the RMS are observed to be decreased by the pulsating cooling.

4.6. Boundary layer characterization

4.6.1. Steady wall temperature measurements

The Nusselt number distributions on the suction surface of the upper flow passage for various test conditions were calculated by using the time-averaged T_w, T_{01}, wall heat flux and calculated main stream heat conduction coefficient and illustrated by the middle plot sequence in Fig. 4.5. A reduction in Nu is observed towards the downstream location of geometrical throat regardless of test condition. While laminar boundary layer thickens, it isolates the surface from heat penetration coming from free stream flow thus Nu decreases. Further downstream an increase in Nu is noticed as an indication of initiation of boundary layer transition. Following a finite length of Nu gradient, relatively constant region of Nu is observed on the rear suction side where the turbulent boundary layer establishes. For low M and Re case, the location of transition is detected on half way of the surface which is far downstream of the shock wave impingement point. This indicates possible natural transition of the blade surface. Moreover, the transition is delayed by 5% S_{max} when the coolant is blown pulsating. When freestream Mach number is increased, transition is moved 5% S_{max} upstream coinciding with the shock impingement location for a longer length. On the other hand, the increase in Re results in delay in transition to a location between 46% and 67% S_{max} for low coolant mass flows. Finally, boundary layer of highest Mach number case gets transitional for all cooling cases between 46% and 51% S_{max} where the shock wave impinges for all cooling schemes and gets turbulent after 67% S_{max}.

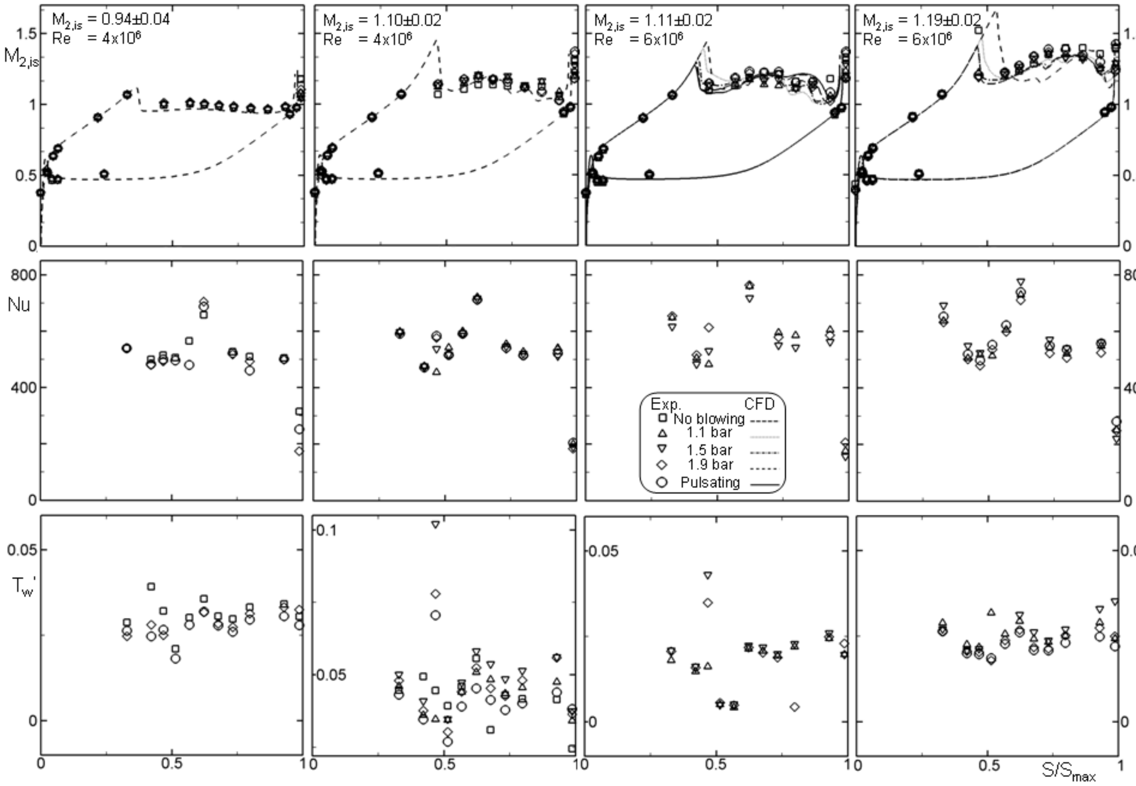

Fig. 4.5. Blade loading (top) together with suction side Nusselt number (middle) and RMS of wall temperature (bottom) distributions on the upper flow passage

4.6.2. Unsteady wall temperature measurements

The wall temperature signal can be split into a mean value and random fluctuations. The random component can be represented by the root mean square (RMS) of it throughout the time span. Consequently, the root mean squared value of the temperature represents the level of unsteadiness for each signal. Thus, the procedure was applied and resulted RMS distributions are represented in Fig. 4.5 bottom. A sudden increase in wall temperature unsteadiness was encountered at same location of the beginning of transition depicted on Nu distribution and shock impingement point on blade loading for both free stream Reynolds numbers due to the relative increase in unsteadiness by transition from laminar to turbulent boundary layer. This behavior not only confirm the consistency of the results inferred from different measurements but also indicates lowest RMS values for unsteady cooling cases which might be an indication of stabilizing effect of pulsating coolant blowing by reducing shock intensity.

The frequency spectrum of the wall temperature signal has also been analyzed in order to characterize unsteady phenomenon occurring in the boundary layer for different test conditions. An example of the low frequency content of the wall temperature signal is given in Fig. 4.6 (left). A distinct peak at around 500 Hz with a dispersion of 50 Hz has consistently been observed for all of the thin film gauges. Similar frequencies were also captured by cooling channel pressure sensor in the absence of trailing edge blowing (Fig. 4.6. right).

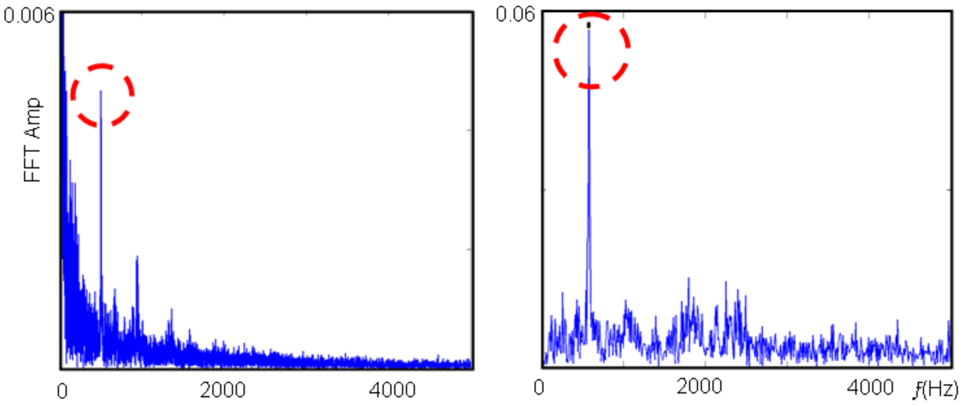

Fig. 4.6. FFT of wall temperature signal (left) edge and cooling channel pressure for no blowing case (right)

The unsteady numerical simulations performed on the complete test section setup demonstrated large recirculation bubbles located immediate downstream of top and bottom steps of the cascade (Fig. 4.7). The structures spanned as large as half chord length. Applying the Strouhal relationship by using the local flow velocity (220 m/s), the recirculation size and backward facing step Strouhal number (0.25) documented by Mehrez et al. [133], the forcing frequency was found around 550 Hz. Therefore, the persistent frequency peak found in the spectrum of wall temperature and the pressure gauge signals might the signature of the unsteadiness caused by the large recirculation bubbles which were present at all blow downs [134].

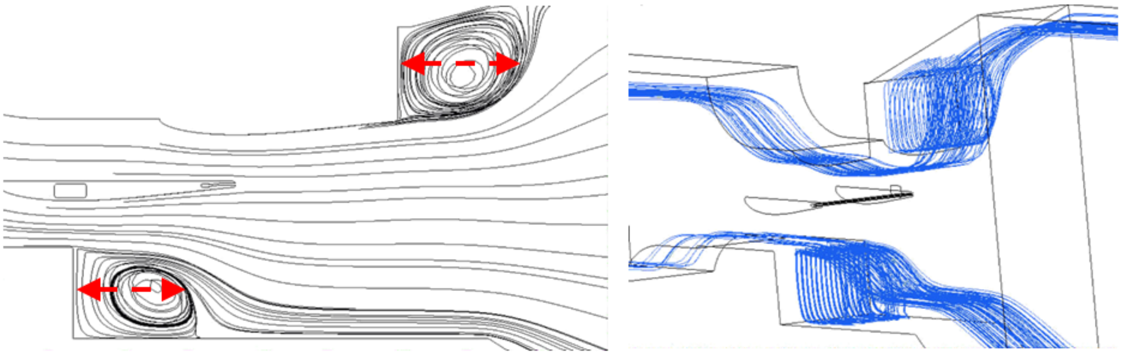

Fig. 4.7. Recirculation bubbles behind the steps by 2D (left) and 3D (right) streamlines

4.7. Base pressure

4.7.1. Base pressure, flow topology and vortex shedding

Trailing edge cooling alters significantly the behavior of the vortex shedding. In the uncooled case, the coherent structures of the von Karman vortex street are clearly visible for both investigated Reynolds numbers (Fig. 4.8). Gostelow [135] stated that for transonic flows the von Karman vortices become unstable and exotic shedding patterns may appear. The present numerical results demonstrate that the oblique shocks generated near the blade trailing edge oscillate at the same frequency of the vortices. In some cases the vortex shedding disappears. Trailing edge continuous cooling changes the vortex shedding pattern since the base region is separated into two different zones and two separated couples of vortices appear (Fig. 4.8). In both cases, the shedding of a single vortex on one side, and a pair of vortices on the other side of the trialing edge described by Williamson and Roshko [136] was identified. Frequency analysis of the base region demonstrated that both regions are tuned with each other but with a different energy distribution within the spectrum. Hence, the vortices have the same harmonics but the amplitudes of their fluctuations are different.

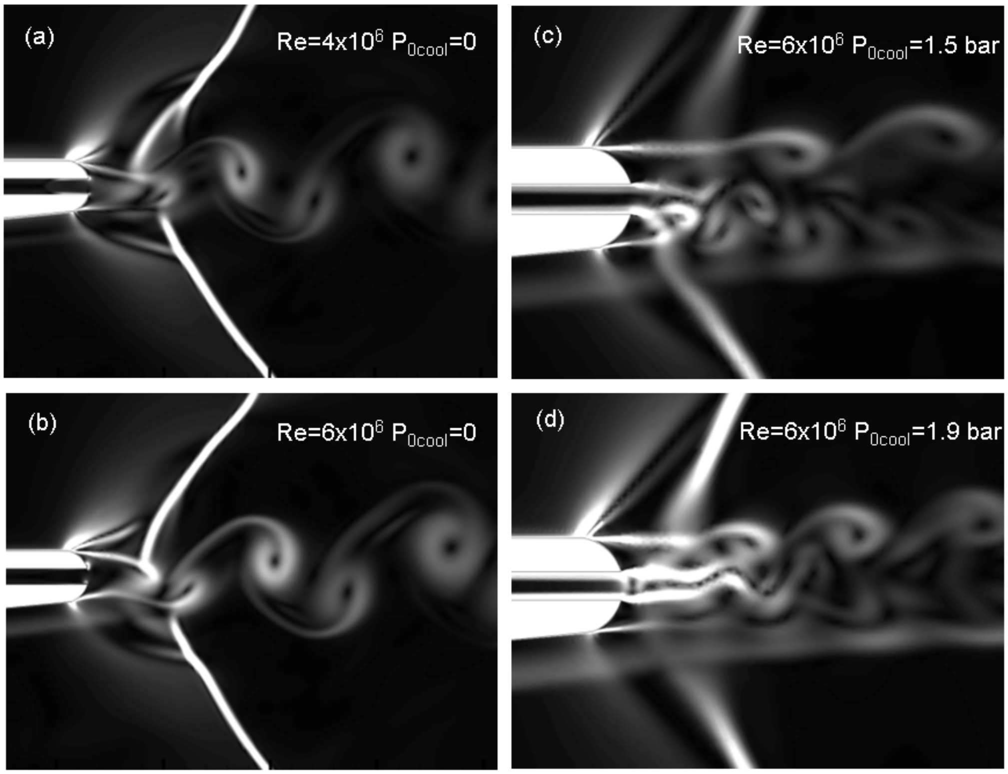

Fig. 4.8. Numerical Schlieren of the base region at $M_{2,is}$=1.1

Fig. 4.9 represents the FFT of the trailing edge pressure sensors, which reveal the resonance frequencies associated to the shedding frequency. One observes that as the flow velocity increases, the shedding frequency is greater. A decrease in the shedding frequency is encountered with increasing Reynolds number owing to the reduction in total temperature and thus on velocity.

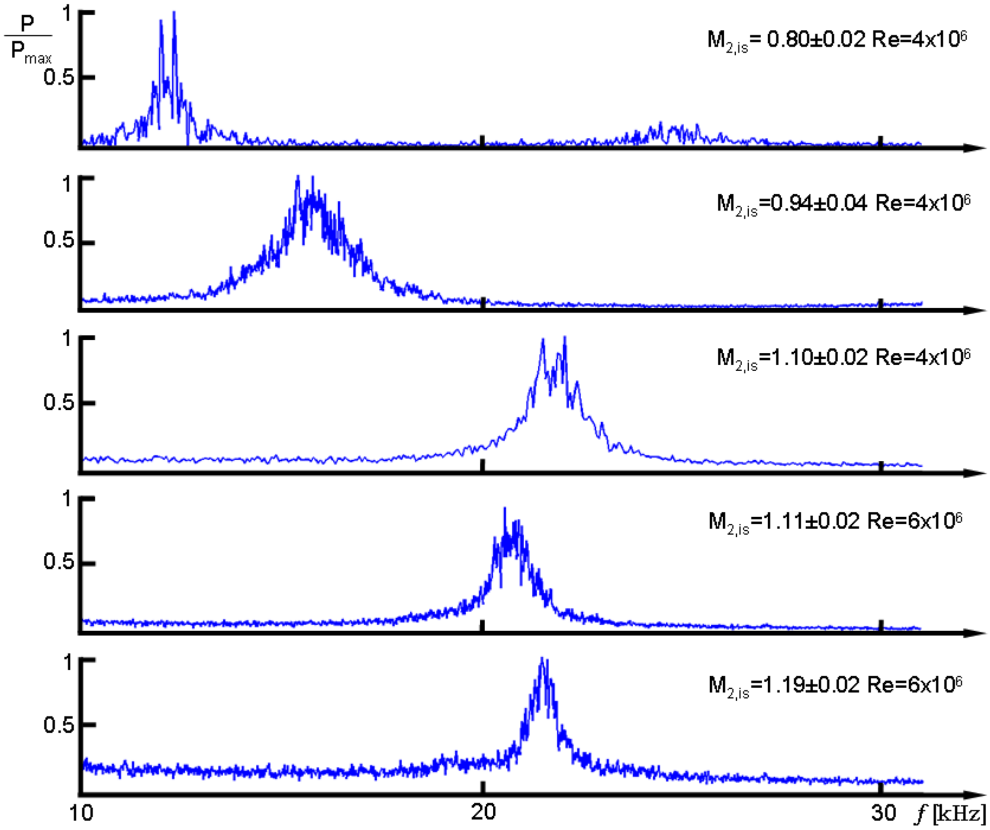

Fig. 4.9. Frequency spectrum of the unsteady base pressure signal for the uncooled case

The fluctuations in the base pressure, caused by the vortex shedding, are of the order of 5% in uncooled case and 13% for the pulsating cooling. Cicatelli and Sieverding [124] observed a 5% fluctuation in their uncooled geometry. URANS simulations in an uncooled transonic turbine stage [102] provided a 5% variability in the stator base pressure. Based on the experimental and numerical shedding frequencies let us define the Strouhal number: $St=fL/v$. Fig. 4.10 displays the evolution of the Strouhal number in function of the isentropic Mach number. The frequencies obtained from experimental and numerical analysis show good agreement with the tabulated data of Motallebi and

Norbury [23]. The Strouhal numbers, based on the real dimension of the upper/lower metal part of the trailing edge, are 0.23 and 0.18 for the $M_{2,is}$=1.2 case with continuous cooling of P_{0cool} = 1.1 bar and 1.5 bar respectively. At a certain distance from the trailing edge the structures coalesce into a single couple of vortices. An increase in Strouhal number is observed for low coolant blowing cases throughout the whole Mach number range. This is due to the displacement of the vortex formation location downstream when the highest base pressure is observed [23]. Augmentation in coolant ejection rates brakes down the base region into two separate parts on each side of the trailing edge and, consequently, leads formation of two distinct vortex structures with higher frequencies as visualized in Fig. 4.8-c. CFD allowed the identification of high Strouhal numbers for the case of high cooling rates (St~0.65).

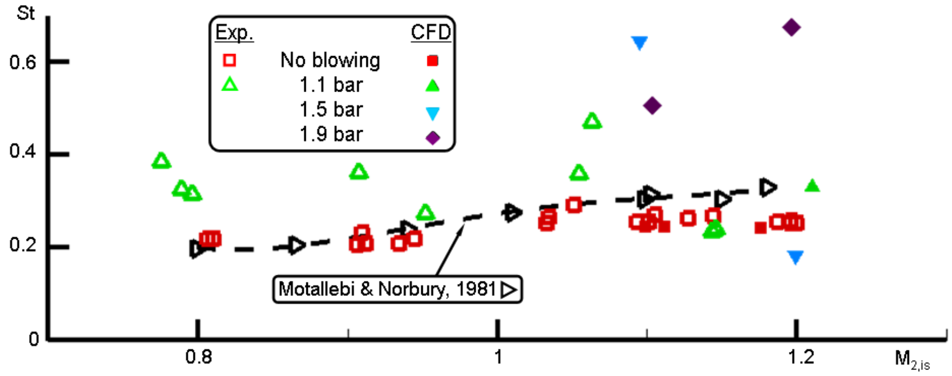

Fig. 4.10. Strouhal number evolution for various test conditions

4.7.2. Base pressure correlation

The base pressure values as a function of outlet Mach numbers are tabulated in Fig. 4.11. Lines represent the Sieverding's correlation [99]. In convergent designs, δ represents the trailing edge wedge angle, ε is the suction side curvature downstream of the throat. The results of the uncooled measurements fit quite well with the correlation belonging to converging-diverging passages. Data obtained with coolant blowing at 1.1 bars fits the Sieverding's correlation equivalent to a (ε+δ)/2=8. Coolant blowing results in an increase of base pressure. The highest increase in base pressure is achieved when the blowing ratio is the lowest. Hence, appropriate use of cooling is similar to morphing the airfoil. Slight changes in cooling rate results in base pressures of different airfoil geometries that one can predict using Fig. 4.11. Base pressure is observed to be maintained on the same level of the continuous cooling for the pulsating coolant ejection. This implies that the order of the accumulated losses is reduced by unsteady cooling.

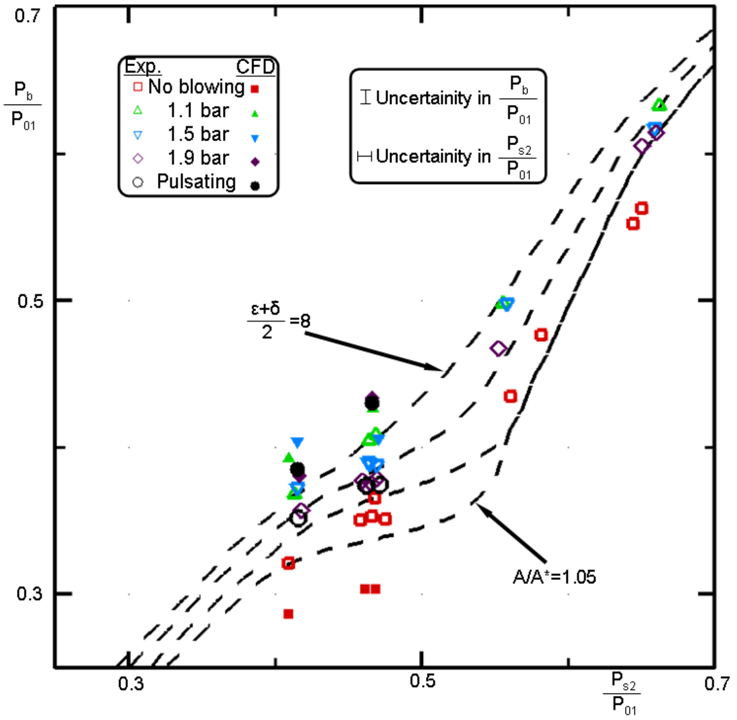

Fig. 4.11. Base pressure for all test cases together with Sieverding's correlation [99]

4.7.3. Trailing edge loss

Trailing edge loss is one of the most significant contributors to the two-dimensional losses in turbines. The mixing of the boundary layers coming from each side of the airfoil generates entropy and causes efficiency deduction. Traupel [137] proposed Eq. 4.1 to calculate the trailing edge loss in turbine cascades where C_{pb} is the base pressure coefficient, d is the trailing edge thickness, s is the chord of the vane and β_2 is the outlet flow angle. In order to achieve the level of loss due to the trailing edge, C_{pb} is obtained from Eq. 4.2 by considering the corresponding outlet conditions and the base pressure.

$$\zeta_{pb} = C_{pb}\frac{d}{s\cdot sin\beta_2} \tag{4.1}$$

$$C_{pb} = \frac{P_{s2}-P_b}{\rho\frac{V_2}{2}} \tag{4.2}$$

Fig. 4.12 presents the calculated base pressure loss variation with respect to isentropic outlet Mach number for all experimental conditions. Trailing edge cooling unexceptionally improved the efficiency at all discharge rates. Besides, the highest decrease in the loss was observed for the lowest cooling pressure due to substantial increase in the base pressure from the null blowing value. Further augmentation in cooling results in reduction in efficiency at all flow condition except the highest Mach number where the range of variation in loss was the minimum. The drop in trailing edge loss was increased from 0.5% to 1.5% with decreasing Mach number. Therefore, the highest improvement by continuous cooling was achieved at high subsonic flow condition. The levels of loss attained by the pulsating coolant were remained at the similar levels, resulted with the steady cooling at the same average rate. Hence, the advantageous nature of pulsating cooling on shock control was not penalized by the trailing edge loss.

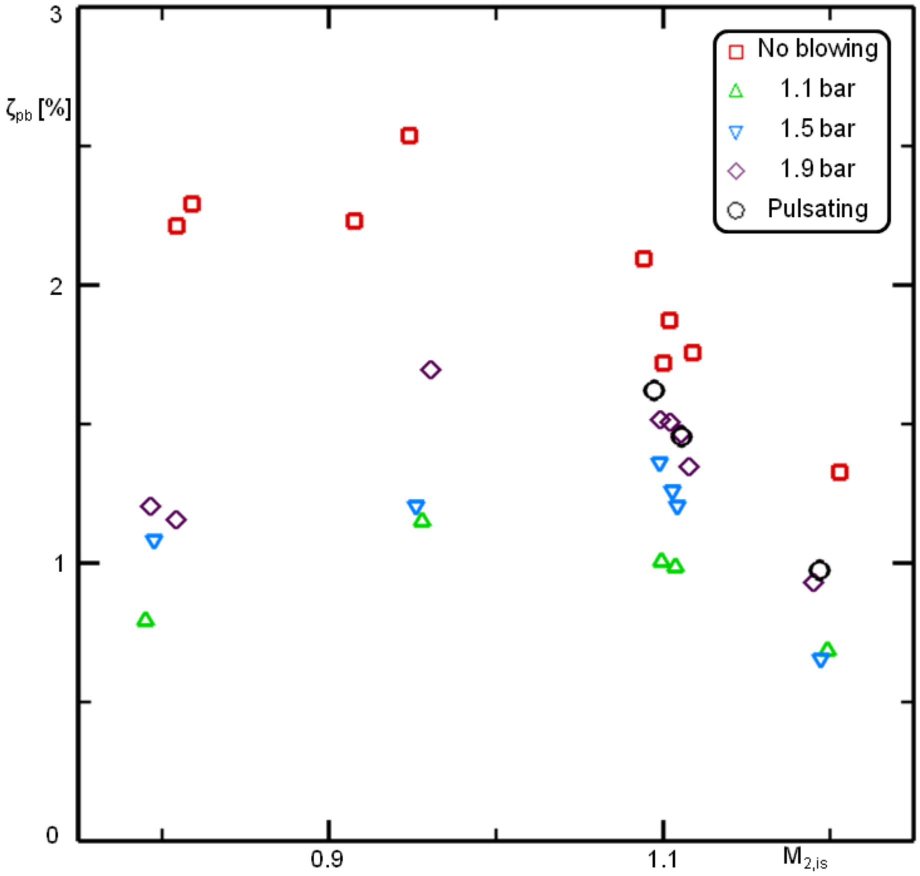

Fig. 4.12. Trailing edge loss vs. outlet Mach number for all test cases.

4.8. Statistical analysis

The statistical analysis of the experimental results has been performed to reveal the significance of the relationships between the design factors (outlet Mach number, Reynolds number and coolant ejection regime) and the response variable (base pressure) with adequate sample size for the analysis. In order to accomplish, the tools of the design of experiment were used. Such investigation not only shows the contribution of each factor on the variation of the responses but also divulges the interaction effects of multiple design factors on the response variable by revealing the statistical importance of each individual and cross interactions. Moreover, the model included the linear regression analysis, which quantifies the relationship between the responses and the design factors.

The statistical analysis software JMP was used as the tool for the investigation. Base pressure to inlet total pressure was selected as response of the system while isentropic outlet Mach number, Reynolds number (two levels: $4x10^6$ & $6x10^6$) and state of the cooling (five levels: no blowing (1), continuous low (2), mid (3), high blowing (4) and pulsating blowing (5)) were used as the design factors. During the analysis, the linear fit model of the JMP was used to statistically understand the relationship between the response variable and seven possible combinations of the design factors (M_{2is}, Re, Cooling, $M_{2,is}$*Re, $M_{2,is}$*Cooling, Re*Cooling and $M_{2,is}$*Re*Cooling).

The linear regression for the base pressure ratio resulted in the fit with the R^2 value of 0.99353. The effect test showed that the influence of M_{2is}, and the cooling scheme were the only significant factors with corresponding p values less than 0.0005 and 0.0001, respectively. None of the second or third order interactions between the design factors was found to be statistically significant. The analysis also revealed that Reynolds number has no significant effect on the level of the base pressure as observed on the scatter plot of the data in Fig. 4.11. Following the outcomes of the first analysis, a second linear fit analysis was performed for M_{2is} and the cooling. The new fit with R^2 value of 0.9629 emphasized the impact of low blowing on the base pressure by relatively lower p values as compared to the other cooling schemes.

CONCLUSIONS

This thesis contains the experimental and numerical efforts devoted to understand the utilization of trailing edge cooling as a control tool to modulate the shock waves. Attaining such objective requires a methodology that divides the problem to subcomponents in increasing complexity from a simplified environment to the realistic problem setup to accomplish the research objectives. Therefore, the research was mainly divided into two sections according to the complexity of the problem. First, the steady and unsteady cooling is numerically studied over simplified geometries. Subsequently an experimental and numerical campaign was carried out over a linear cascade test section.

The first part of the research numerically studied the effects of steady and unsteady cooling. The supersonic flow field over simplified blunt and circular trailing edge geometries were simulated to obtain a fundamental understanding of the main flow parameters being affected from coolant ejection. A blunt trailing edge was initially simulated for a large range of blowing to correlate the changes in the shock properties with the purge rate. The results of the numerical analysis indicated an optimum level of cooling to mitigate the shock waves. The low rate of blowing (ρ_c/ρ_f=1.3) effectively increased the base pressure and reducing the shock intensity (~80% reduction from the no blowing value). The intensive coolant purge resulted in a double shock system at the trailing edge. The simulations performed over the circular trailing edge demonstrated similar shock modulation and base pressure behavior. Further analysis on a lower free stream Mach number (M=1.2) exhibited similar levels of shock intensity reduction. Hence, the coolant discharge at small rates resulted in shock attenuation in low supersonic range.

Following the steady purge, pulsating coolant was tested to identify the unsteady characterization of the shock properties and the base pressure. Circular trailing edge was studied for unsteady cooling at various duty cycles to define the relevant cooling parameters used in the experiments. The base region flow field and pressure variations on the channel outlet showed that the down stroke of the duty cycle had a delayed stabilizing effect on the wake unsteadiness. Moreover, the maximum cooling period in each pulse promoted strong vortex shedding. The trends in unsteady base pressure and shock intensity also followed an unsteady variation with pulsating cooling.

The pulsating cooling effects on trailing edge shock waves were experimentally and numerically investigated over a range of free stream Mach and Reynolds numbers on a linear cascade in the second part of the research. Novel airfoil geometry was designed to provide downstream flow field similar to the vanes of modern high pressure turbines. A detailed characterization of the pulsating valve used for the experiments was carried out for a wide range of cooling rate and frequencies. The design of the test section allowing steady and unsteady pressure and temperature measurements together with Schlieren flow visualizations was accomplished. The time-averaged and time-resolved aerodynamic features of the flow field were identified. Downstream flow field and complex shock wave interactions on the free steam were detected owing to the high speed Schlieren images processed with an advanced pattern recognition algorithm developed. The numerical simulations provided a deeper insight on the base region flow topology and vortex shedding schemes changing with cooling properties. Von Karman shedding pattern was altered by coolant introduction. Hybrid modes of shedding were observed. Moreover, unsteady cooling prohibited the formation of coherent structures.

The major findings of the combined experimental and numerical study can be listed as follows. The passage loading and pitchwise downstream pressure measurements indicated that highest reduction in shock impact was achieved by pulsating cooling. The shock wave oscillations were altered by coolant pulsation frequency. Unsteady cooling minimized the variation in the shock wave angle. Hence, the shock wave stabilization was attained by pulsating purge. Base pressure and Strouhal number correlations for a wide range of test conditions and different blowing regimes were established in conjunction with the existing correlations in the literature. A significant reduction in trailing edge loss was obtained by minimum blowing. Besides, pulsating cooling maintained the same level of loss with steady cooling at the same rate while providing shock modulation.

Overall, the research provided a detailed collection of the unique experimental data to investigate the feasibility of pulsating trailing edge cooling on controlling the fish tail shock structure. New flow passage designs utilizing more sophisticated cooling systems might result in more efficient turbines with longer operational life.

REFERENCES

[1] J. Ortmanns, C. Pixberg, V. Gummer, Numerical investigation of vortex generators to reduce cross- passage flow phenomena in compressor stator end-walls, Proc. of the Inst. of Mech. Eng. Part A- J. of Power and Energy, 225 (2011) 877-885.

[2] A. Hergt, R. Meyer, K. Engel, Experimental investigation of flow control in compressor cascades, in: Proc. of ASME Turbo Expo 2006: Power for Land, Sea and Air, May 06-11, Barcelona, Spain, 2006.

[3] A. Hergt, R. Meyer, M.W. Muller, K. Engel, Loss Reduction In Compressor Cascades By Means Of Passive Flow Control, in: Proc. of ASME Turbo Expo 2008: Power for Land, Sea and Air, Jun 09-13, Berlin, Germany, 2008.

[4] A. Hergt, R. Meyer, K. Engel, Effects Of Vortex Generator Application On The Performance Of A Compressor Cascade, in: Proc. of ASME Turbo Expo 2010: Power for Land, Sea and Air, Jun 14-18, Glasgow, Scotland, 2010.

[5] C. Santner, E. Gottlich, A. Marn, J. Hubinka, B. Paradiso, The Application of Low-Profile Vortex Generators in an Intermediate Turbine Diffuser, ASME J. of Turbomach. 134 (2012) 011023.

[6] D. Lengani, D. Simoni, M. Ubaldi, P. Zunino, F. Bertini, Turbulent boundary layer separation control and loss evaluation of low profile vortex generators, Experimental Thermal and Fluid Science 35 (2011) 1505–1513.

[7] D.R. Carroll, P.I. King, Rutledge L. James, Flow Visualization Study Of Passive Flow Control Features On A Film-Cooled Turbine Blade Leading Edge, in: Proc. of ASME Turbo Expo 2010: Power for Land, Sea and Air, Jun 14-18, Glasgow, Scotland, 2010.

[8] J.P. Lake, P.I. King, R.B. Rivir, Low Reynolds Number Loss Reduction on Turbine Blades with Dimples and V-Grooves, AIAA 00-0738, in: Proc. of 38th Aerospace Sciences Meeting & Exhibit, Reno, Nevada, 2000.

[9] D.G. Bohl, R.J. Volino, Experiments with three-dimensional passive flow control devices on low-pressure turbine airfoils, ASME J. of Turbomach. 128 (2006) 251-260.

[10] O. Rodriguez, Base Drag Reduction By Control Of The 3-Dimensional Unsteady Vortical Structures, Exp. In Fluids. 11 (1991) 218-226.

[11] S.L. Gai, S.D. Sharma, Experiments On The Reduction Of Base Drag Of A Blunt Trailing Edge Aerofoil In Subsonic Flow, Aeronautical Journal, 85 (1981) 206-210.

[12] M. Zhou, J.Q. Zhu, X.G. Lu, Z.H. Ge, K.X. Yan, R. Huang, Study Of Flow Control Using A Slotted Blade For A Compressor Airfoil At Low Reynolds Numbers, in: Proc. of ASME Turbo Expo 2010: Power for Land, Sea and Air, Jun 14-18, Glasgow, Scotland, 2010.

[13] I. El-Gendi, M.K. Mohammed, K. Mori, Y. Nakamura, Novel Flow Control Method For Vortex Shedding Of Turbine Blade, Transactions of the Japan Soc. for Aeronautical and Space Sciences, 53 (2010) 122-129.

[14] Y.-L. Lin, M.J. Rimlinger, T.I-P. Shih, B. P. Willis, Control of Shock-Wave/Boundary-Layer Interactions with Passive Blowing and Bleeding, AIAA-1997-3002, in Proc. of 33rd AIAA/ASME/SAE&ASEE Joint Propulsion Conference & Exhibit, Jul. 6-9, Seattle, WA, 1997.

[15] F.H. Kost, A.T. Holmes, Aerodynamic Effect of Coolant Ejection in the Rear Part of Transonic Rotor Blades, AGARD CP 390 (1985) 41-1-12.

[16] D.E. Bohn, V.J. Becker, K.D. Behnke, B.F. Bonhoff, Experimental and Numerical Investigations of the Aerodynamical Effects of Coolant Injection through the Trailing Edge of a Guide Vane, ASME Paper No. 95-GT-26, in: Proc. of ASME International Gas Turbine and Aeroengine Congress and Exposition, June 5-8, Houston, TX, 1995.

[17] C.H. Sieverding, T. Arts, R. Denos, F. Martelli, Investigation of the Flow Field Downstream of a Turbine Trailing Edge Cooled Nozzle Guide Vane, ASME J. of Turbomach. 118 (1996) 291-300.

[18] C. Kapteijn, J. Amecke, V. Michelassi, Aerodynamic Performance of a Transonic Turbine Guide Vane with Trailing Edge Coolant Ejection: Part I-Experimental Approach, ASME J. of Turbomach. 118 (1996) 519-528.

[19] O. Uzol, C. Camci, Aerodynamic Loss Characteristics of a Turbine Blade with Trailing Edge Coolant Ejection: Part 2-External Aerodynamics, Total Pressure Losses, and Predictions, ASME J. of Turbomach. 123 (2001) 249-257.

[20] C.H. Sieverding, The influence of Trailing Edge Ejection on the Base Pressure in Transonic Turbine Cascades, ASME J. of Eng. for Power 105 (1983) 215-222.

[21] M. Raffel and F. Kost, Investigation of Aerodynamic Effects of Coolant Ejection at the Trailing Edge of a Turbine Blade Model by PIV and Pressure Measurements, Exp. in Fluids. 24 (1998) 447-461.

[22] B.H. Saracoglu, G. Paniagua, P. Rambaud, Blunt Trailing Edge Cooling Effects at Supersonic Regime, AIAA-2009-5105, in: Proc. of 45th AIAA/ASME/SAE&ASEE Joint Propulsion Conference, Aug. 2-5, Denver, CO, 2009.

[23] F. Motallebi, J.F. Norbury, The effect of base bleed on vortex shedding and base pressure in compressible flow, J. of Fluid Mech. 110 (1981) 273-292.

[24] J. Joo, P. Durbin, Simulation of Turbine Blade Trailing Edge Cooling, ASME J. of Fluids Eng. 131 (2009) 021102.

[25] G. Cicatelli, C.H. Sieverding, A Review of Research on Unsteady Turbine Blade Wake Characteristics, AGARD CP 571 (1995) 6-1-13.

[26] D.M. Feng, F. Chen, Y. Song, H. Chen, Z. Wang, Enhancing Aerodynamic Performances of Highly Loaded Compressor Cascades via Air Injection, Chinese Journal of Aeronautics 22(2009) 121-128.

[27] Y. Zhou, H. Liu, Z. Zou, J. Ye, Boundary layer separation control on a highly-loaded, low-solidity compressor cascade, Journal of Thermal Science 19 (2010) 97−104.

[28] S. Evans, J. Coull, I. Haneef, H. Hodson, Minimizing the Loss Produced by a Turbulent Separation Using Vortex Generator Jets, AIAA Journal 50 (2012) 778-787.

[29] R.A. Gomes, R. Niehuis, Aerothermodynamics of a High-Pressure Turbine Blade With Very High Loading and Vortex Generators, ASME J. of Turbomach. 134 (2012) 011020.

[30] R. Sondergaard, R.B. Rivir, J.P. Bons, Control of low-pressure turbine separation using vortex-generator jets, J. of Propuls. and Power 18 (2002) 889-895.

[31] R.K. Sullerey, A. Mishra, Active and Passive Flow Control in a Turbine Cascade, International Journal of Turbo & Jet-Engines, 25 (2008) 155-162.

[32] D.P. Rizzetta, R.M. Visbal, Numerical study of active flow control for a transitional highly loaded low-pressure turbine, J. of Fluids Eng. 128 (2006) 956-967.

[33] L. Hansen, J. Bons, Flow measurements of vortex generator jets in separating boundary layer, J. of Propuls. and Power, 22 (2006) 558-566.

[34] R.J. Volino, O. Kartuzova, M.B. Ibrahim, Experimental And Computational Investigations Of Low-Pressure Turbine Separation Control Using Vortex Generator Jets,

in: Proc. of ASME Turbo Expo 2009: Power for Land, Sea and Air, Jun 08-12, Orlando, Florida, 2009.

[35] X.M. Liu, H.Y. Zhou, Numerical Investigations Of Flow Separation Control For A Low Pressure Turbine Blade Using Steady And Pulsed Vortex Generator Jets, in: Proc. of ASME Turbo Expo 2010: Power for Land, Sea and Air, Jun 14-18, Glasgow, Scotland, 2010.

[36] R.J. Volino, O. Kartuzova, M.B. Ibrahim, Separation Control on a Very High Lift Low Pressure Turbine Airfoil Using Pulsed Vortex Generator Jets, ASME J. of Turbomach. 133 (2011) 041021.

[37] D. Postl, W. Balzer, H.F. Fasel, Control of laminar separation using pulsed vortex generator jets: direct numerical simulations, J. of Fuid Mech. 676 (2011) 81-109.

[38] W. Balzer, A. Gross, H.F. Fasel, Active flow control of low-pressure turbine separation, in: Proc. of Annual High Performance Computer Modernization Program Users Group Conference, Jun 19-21, Pittsburgh, Pennsylvania, 2007.

[39] J.P. Bons, R. Sondergaard, R.B. Rivir, The fluid dynamics of LPT blade separation control using pulsed jets, ASME J. of Turbomach. 124 (2002) 77-85.

[40] J.P. Bons, L.C. Hansen, J.P. Clark, P.J. Koch, R. Sondergaard, Designing low-pressure turbine blades with integrated flow control, in: Proc. of ASME Turbo Expo 2005: Power for Land, Sea and Air, Jun 06-09, Reno, Nevada, 2005.

[41] A. Gross, H.F. Fasel, Numerical investigation of low-pressure turbine blade separation control, AIAA J. 43 (2005) 2514-2525.

[42] D. Reimann, M. Bloxham, K.L. Crapo, J.D. Pluim, J.P. Bons, Influence of jet-induced transition on separating low-pressure turbine boundary layer, J. of Propuls. and Power, 23 (2007) 996-1006.

[43] D.P. Rizzetta, M.R. Visbal, Numerical simulation of separation control for transitional highly loaded low-pressure turbines, AIAA J. 43 (2005) 1958-1967.

[44] M. Matejka, L. Popelka, P. Safarik, J. Nozicka, Influence Of Active Methods Of Flow Control On Compressor Blade Cascade Flow, in: Proc. of ASME Turbo Expo 2008: Power for Land, Sea and Air, Jun 09-13, Berlin, Germany, 2008.

[45] X.Q. Zheng, S. Zhou, Y.J. Lu, A.P. Hou, Q.S. Li, Flow control of annular compressor cascade by synthetic jets, ASME J. of Turbomach. 130 (2008) 021018

[46] Y. Liu, T. Sun, C. Guan, B. Wang, The influence of synthetic jet excitation on secondary flow in compressor cascade, J. of Thermal Science 19 (2010) 500−504.

[47] C. Gmelin, M. Steger, F. Thiele, A. Huppertz, M. Swoboda, Unsteady Rans Simulations Of A Highly Loaded Low Aspect Ratio Compressor Stator Cascade With Active Flow Control, in: Proc. of ASME Turbo Expo 2010: Power for Land, Sea and Air, Jun 14-18, Glasgow, Scotland, 2010.

[48] V. Zander, M. Hecklau, W. Nitsche, A. Huppertz, M. Swoboda, Active flow control by means of synthetic jets on a highly loaded compressor cascade, Proc. of the Inst. of Mech. Eng. Part A-J. Power and Energy, 225 (2011) 897-906.

[49] X.M. Liu, X. Wang, Performance Improvement Of Low Pressure Turbine Blade By Using Synthetic Jets, Eng. Appl. of Comp. Fluid Mech. 5 (2011) 445-458.

[50] M. Marconcini, R. Pacciani, A. Arnone, Urans Predictions Of The Effects Of Synthetic Jets On The Separated, Transitional Flow Over A Low-Pressure-Turbine-Like Flat Plate, in: Proc. of ASME Turbo Expo 2010: Power for Land, Sea and Air, Jun 14-18, Glasgow, Scotland, 2010.

[51] M.C. Galbraith, A. Kasliwal, K. Ghia, U. Ghia, Numerical Simulation Of A Low Pressure Turbine Blade Employing Active Flow Control, in: Proc. of ASME Fluid Engineering Division Summer Conference, Jul 17-20, Miami, Florida, 2006.

[52] R.J. Volino, Separation control on low-pressure turbine airfoils using synthetic vortex generator jets, ASME J. of Turbomach. 125 (2003) 765-777.

[53] S. Poondru, U. Ghia, K. Ghia, Active Flow Control On Low-Pressure Turbine Blades Using Synthetic Jets, in: Proc. of ASME Fluid Engineering Division Summer Conference, Jul 17-20, Miami, Florida, 2006.

[54] D. Lengani, D. Simoni, M. Ubaldi, P. Zunino, F. Bertini, Application of a Synthetic Jet to Control Boundary Layer Separation under Ultra-High-Lift Turbine Pressure Distribution, Flow Turbulence Combust. 87 (2011) 597–616.

[55] C.Q. Nie, G. Li, J.Q. Zhu, Y. Zhang, Y.T. Li, Investigation of dielectric barrier discharge plasma flow control, Sci. China Ser. E-Tech. Sci. 51 (2008) 1064-1072.

[56] D.P. Rizzetta, M.R. Visbal, Numerical investigation of plasma-based flow control for transitional highly loaded low-pressure turbine, AIAA J. 45 (2007) 2554-2564.

[57] J.H. Huang, T.C. Corke, F.O. Thomas, Plasma actuators for separation control of low-pressure turbine blades, AIAA J. 44 (2006) 51-57.

[58] G. Li, C.Q. Nie, Y.M. Li, J.Q. Zhu, Y. Xu, Experimental Investigation of Flow Separation Control Using Dielectric Barrier Discharge Plasma Actuators.” Plasma Scie. and Tech, 10 (2008) 605-611.

[59] G. Li, Y. Xu, B. Lin, J.Q. Zhu, C.Q. Nie, H.W. Ma, Z.F. Wang, Control of endwall secondary flow in a compressor cascade with dielectric barrier discharge plasma actuation, Sci. China Ser. E-Tech. Sci., 52 (2009) 3715—3721, doi: 10.1007/s11431-009-0187-0

[60] Y.H. Li, Y. Wu, M. Zhou, C.B. Su, X.W. Zhang, J.Q. Zhu, Control of the corner separation in a compressor cascade by steady and unsteady plasma aerodynamic actuation, Exp Fluids 48 (2010) 1015–1023.

[61] J.E. Stephens, T. Corke, S. Morris, Blade-Mounted Single Dielectric Barrier Discharge Plasma Actuators in Turbine Cascade, , J. of Propuls. and Power, 27 (2011) 692-699.

[62] H. Perez-Blanco, R. Van Dyken, A. Byerley, T. McLaughlin, Turbine cascade flow control using a "wake filling" pulsed plasma actuator, in: Proc. of ASME Turbo Expo 2005: Power for Land, Sea and Air, Jun 06-09, Reno, Nevada, 2005.

[63] T.V. Jones, D.L. Shultz, A.D. Hendley, On the Flow in an Isentropic Free Piston Tunnel, ARC R&M 3731, 1973.

[64] D.L. Shultz, T.V. Jones, M.L.G. Oldfield, L.C. Daniels, A new transient facility for the measurement of heat transfer rates in “High Temperature Problems in Gas Turbine Engines”, AGARD CP-229, 1978.

[65] H. Consigny, B.E. Richards, Short Duration Measurements of Heat-Transfer Rate to a Gas Turbine Rotor Blade, J. of Eng. for Power, 104 (1982) 542-550.

[66] M. Gonzalez, G. Paniagua, B. Saracoglu, A. Tiseira, Pulsating cooling system for high-pressure turbine blades, AIAA-2010-4587, in: Proc. of the 5th AIAA Flow Control Conference, June 28-1, Chicago, IL, 2010.

[67] H. Nakamura, I. Asano, M. Adachi, and J. Senda. Analysis of Pulsating Flow Measurement of Engine Exhaust by a Pitot Tube Flowmeter. IMechE International Journal of Engine Research, 6(1):85-93, 2005.

[68] R.S. Benson. The Thremodynamics and Gas Dynamics of Internal Combustion Engines, volume 1. Clarendon, Oxford, UK, 1982.

[69] J. Galindo, J.R. Serrano, F.J. Arnau, P. Puqueras, Description of a semi-independent time discretization methodology for a one dimesinoal gas dynamics model, ASME J. of Eng. for Gas Turbines and Power, 131 (2009) 34504

[70] G.S. Settles, Schlieren and Shadowgraph Techniques: Visualizing Phenomena in Transparent Media, Springer-Verlag, Berlin, 2001.

[71] Otsu, N., A Threshold Selection Method from Gray-Level Histograms, IEEE Transactions on Systems, Man, and Cybernetics, Vol. 9, No. 1, 1979, pp.62-66.

[72] I. Bucher, Circle fit, Matlab Central File Exchange, 2004.

[73] Y Wu, M L Giger, K Doi, C J Vyborny, R A Schmidt, C.E.Metz. Artificial neural networks in mammography: application to decision making in the diagnosis of breast cancer. Radiology. 1993;187(1):81-87.

[74] Mahmud, S.M.; Alrabady AI. A new decision making algorithm for airbag control. IEE transaction on Vehicular Technology. 1995;44(3):690-697.

[75] Haralick, Robert M., and Linda G. Shapiro, Computer and Robot Vision, Volume I, Addison-Wesley, 1992, pp. 28-48.

[76] J.R. Carlson, N. Duquesne, C.L. Rumsey, T.B. Gatski, Computation of turbulent wake flows in variable pressure gradient, Comput. Fluids 30 (2001) 161-170.

[77] N. Mulvany, T.Y. Tu, L. Chen, B. Anderson, Assessment of two-equation turbulence modeling for high Reynolds number hydrofoil flow, Int. J. Numer. Methods Fluids 45 (2004) 275-299.

[78] T. Do, L. Chen, J. Tu, Numerical study of turbulent trailing-edge flow with base cavity effects using URANS, J. of Fluids and Struct. 26(2010) 1155-1173.

[79] H.E. Smith, Experimental and Theoretical Investigation of the Near Wake Behind a Rearward Facing Step in Supersonic Flow, PhD Dissertation, University of Cincinnati, 1969.

[80] L.F. Richardson, The approximate Arithmetical Solution by Finite Differences of Physical Problems Involving Differential Equations, with an Application to the Stresses in a Masonry Dam, Trans. R. Soc. London, Ser. A, 210 (1910) 307-357.

[81] F. Stern, R. Wilson, J. Shao, Quantitative V&V of CFD simulations and certification of CFD codes, Int. J. Numer. Methods in Fluids, 50 (2006) 1335-1355.

[82] G.E. Elsinga, B.W. van Oudheusden, F. Scarano, D.W. Watt, Assessment and application of quantitative schlieren methods: Calibrated color schlieren and background oriented schlieren, Exp. in Fluids 36 (2004) 309-325.

[83] M.J. Hargather, G.S. Settles, Recent Developments in Schlieren and Shadowgraphy, AIAA-2010-4206, in: Proc. of 27th AIAA Aerodynamic Measurement Technology and Ground Testing Conference, Jun. 28-Jul. 9, Chicago, IL, 2010

[84] B.H. Saracoglu, G. Paniagua, S. Salvadori, F. Tomasoni, S. Duni, A. Miranda, Trailing edge shock modulation by pulsating coolant ejection, Applied Thermal Engineering (2012), doi:10.1016/j.applthermaleng.2012.04.036

[85] P. Adami, F. Martelli, V. Michelassi, Three-Dimensional Investigations for Axial Turbines by an Implicit Unstructured Multi-Block Flow Solver, ASME 2000-GT-0636, in: Proc. ASME IGTI Turbo Expo, Munich, Germany, 2000

[86] M. Montomoli, M. Massini and S. Salvadori, Geometrical uncertainty in turbomachinery: Tip gap and fillet radius, Computers and Fluids 46 (2010) 362-368.

[87] P.L. Roe, Characteristic based scheme for Euler equations, Ann. Rev. Fluid Mech. (1), 1986.

[88] D.C. Wilcox, Turbulence Modeling for CFD, DCW Industries Inc., 1993.

[89] F.R. Menter, Zonal Two Equation k-ω Turbulence Models For Aerodynamic Flows, AIAA-1993-2906, in: Proc. of 23rd Fluid Dynamics, Plasmadynamics, and Lasers Conference, July 6-9, Orlando, FL, 1993.

[90] A. Ying, M. Narula, R. Hunt, M. Abdou, Y. Ando, I. Komada, Integrated thermo-fluid analysis towards helium flow path design for an ITER solid breeder blanket module Fusion Engineering and Design 82 (2007).

[91] Solver Reference of User's Guide of SC/Tetra Version 5.0.

[92] T. Matsushima, An automatic mesh generator based CFD system to be used as a Design Tool, SAE paper 2001-01-0037 (2001).

[93] Q. Fan, CFD simulation of pressure drop in line pipe, SAE paper 2006-01-1443 (2006).

[94] J. F. Nash, A Review of Research on Two-Dimensional Base Flow, ARC R&M. No. 3323 (1963) 1-25.

[95] J. F. Nash, A Discussion of Two-Dimensional Turbulent Base Flows, ARC R&M. No. 3468 (1967) 1-46.

[96] J.F. Nash, V.G. Quincey, J. Callinan, Experiments on Two-Dimensional Base Flow at Subsonic and Transonic Speeds, ARC R&M No. 3427 (1963) 1-34.

[97] F. Hama, Experimental Studies on the Lip Shock, AIAA J. 6 (1968) 212-219.

[98] S. Kawai, K. Fujii, Time-Series and Time-Averaged Characteristics of Subsonic to Supersonic Base Flows, AIAA J. 45 (2007) 289-301.

[99] C.H. Sieverding, M. Stanislas, J. Snoeck, The Base Pressure Problem in Transonic Turbine Cascades, J. of Eng. for Power, 102 (1980) 711-718.

[100] J. D. Denton, L. Xu, The Trailing Edge Loss of Transonic Turbine Blades, ASME J. of Turbomach. 112 (1990) 277-285.

[101] J. D. Denton, Loss Mechanisms in Turbomachines, ASME J. of Turbomach. 115 (1993) 621-656.

[102] G. Paniagua, T. Yasa, A. de la Loma, L. Castillon, T. Coton, Unsteady strong shock interactions in a transonic turbine: Experimental and numerical analysis, J. of Propuls. and Power 24 (2008) 722-731.

[103] V. I. Kornilov, Correlation of the separation region length in shock wave/channel boundary layer interaction, Exp. in Fluids. 23 (1997) 489-497.

[104] R.H. Tindell, B. P. Willis, Experimental Investigation of Blowing for Controlling Oblique Shock/Boundary Layer Interactions, AIAA-1997-2642, in: Proc. of 33rd AIAA/ASME/SAE/ASEE Joint Propulsion Conference & Exhibit, Jul. 6-9, Seattle, WA, 1997.

[105] D.D. Young, S.A. Jenkins, D.N. Miller, An investigation of Active Flowfield Control for Inlet Shock/Boundary Layer Interaction, AIAA-2005-4020, in: Proc. of 41st AIAA/ASME/SAE/ASEE Joint Propulsion Conference & Exhibit, Jul. 10-13, Tuscon, AZ, 2005.

[106] C. Kapteijn, Wake Development Downstream of a Transonic Turbine Inlet Guide Vane with Trailing Edge Ejection, AGARD CP 571 (1995) 14-1-7.

[107] F.E. Ames, J.D. Johnson, N.J. Fiala, Gill Slot Traililgn Edge Aerodynamics-Effects of Blowing Rate, Reynolds Number, and External Turbulence on Aerodynamics Losses and Pressure Distribution, ASME Paper No. GT2007-27399, in: Proc. of ASME Turbo Expo 2007: Power for Land, Sea and Air, May 14-17, Montreal, Canada, 2007.

[108] N. Kulasekharan, B.V.S.S.S. Prasad, Computational Investigation in the Trailing Edge Region of Cooled Turbine Vane-Comparison of Different Channel Shapes, ASME

Paper No. GT2007-27421, in: Proc. of ASME Turbo Expo 2007: Power for Land, Sea and Air, May 14-17, Montreal, Canada, 2007.

[109] S. Bernsdorf, M.G. Rose, R.S. Abhari, Experimental Validation of Quasisteady Assumption in Modeling of Unsteady Film-Cooling, ASME J. of Turbomach. 130 (2008) 011022.

[110] C. Allery, S. Guerin, A. Hamdouni, A. Sakout, Experimental and numerical POD study of the Coanda effect used to reduce self-sustained tones, Mech. Res. Commun. 31 (2004) 105–120

[111] N. Alleborn, K. Nandakumar, H. Raszillier, F. Durst, Further contributions on the two-dimensional flow in a sudden expansion, J. Fluid Mech. 330 (1997) 169-188.

[112] F. Durst, J.C.F. Pereira, C. Tropea, The plane symmetric sudden-expansion flow at low Reynolds numbers, J. Fluid Mech. 248 (1993) 567-581.

[113] R.M. Fearn, T. Mullin, K.A. Cliffe, Nonlinear flow phenomena in a symmetric sudden expansion, J. Fluid Mech. 211 (1990) 595-608.

[114] W. Cherdron, F. Durst, J.H. Whitelaw, Asymmetric flows and instabilities in symmetric ducts with sudden expansions, J. Fluid Mech. 84 (1978) 13-31.

[115] B.F. Carroll, J.C. Dutton, Characteristics of Multiple Shock Wave/Turbulent Boundary-Layer Interactions in Rectangular Ducts, J. Propuls. 6 (1990) 186-193.

[116] Gostelow, J.P., Mahallati, A., Carscallen, W. E. and Rona, A. “Encounters with Vortices in a Turbine Nozzle Passage,” ISROMAC-13 2010-37, 2010

[117] S. Djouimaa, L. Messaoudi, P.W. Giel, Transonic turbine blade loading calculations using different turbulence models – effects of reflecting and non-reflecting boundary conditions, Appl. Therm. Eng. 27 (2007) 779-787.

[118] J.P. Gostelow, A. Mahallati, S.A. Andrews, W.E. Carscallen, Measurement and Computation of Flowfield in Transonic Turbine Nozzle Blading With Blunt Trailing Edges, ASME Paper No. GT2009-59686, in: Proc. of ASME Turbo Expo 2009: Power for Land, Sea and Air, June 8-12, Orlando, FL, 2009.

[119] O. Uzol, C. Camci, B. Glezer, Aerodynamic Loss Characterization of a Turbine Blade With Trailing Edge Coolant Ejection: Part I – Effect of Cut-Back Length, Spanwise Rib Spacing, Free-Stream Reynolds Number and Chordwise Rib Length on Discharge Coefficients, ASME J. of Turbomach. 123 (2001) 238-248.

[120] M.T. Schobeiri, K. Pappu, Optimization of Trailing Edge Ejection Mixing Losses: A Theoretical and Experimental Study, J. of Fluid Eng. 121 (1999) 118-125.

[121] A. Rowe, A.L.A. Fry, F. Motallebi, Influence of Boundary Layer Thickness on Base Pressure and Vortex Shedding Frequency, AIAA J. 39 (2000) 754-756.

[122] C.H. Sieverding, H. Heinemann, The Influence of Boundary Layer State on Vortex Shedding From Flat Plates and Turbine Cascades, ASME J. of Turbomach. 112 (1990) 181-187.

[123] K. Vassilopoulos, S.L. Gai, Unsteady Base Flow – Vortex Shedding and Pressure Fluctuations, AIAA-1996-1957, in: Proc. of the 20th Congress of the International Council of the Aeronotical Sciences, Sep. 8-13, Napoli, Italy, 1996.

[124] G. Cicatelli, C.H. Sieverding, The Effect of Vortex Shedding on the Unsteady Pressure Distribution Around the Trailing Edge of a Turbine Blade, ASME J. of Turbomach. 119 (1997) 810-819.

[125] J.L. Rutledge, P.I. King, R. Rivir, Net Heat Flux Reduction for Pulsed Film Cooling on a Turbine Blade Leading Edge, AIAA-2009-5103, in: Proc. of 45th AIAA/ASME/SAE&ASEE Joint Propulsion Conference, Aug. 2-5, Denver, CO, 2009.

[126] J.L. Rutledge, P.I. King, R. Rivir, Experimental Flow Visualization of Pulsed Film Cooling on a Turbine Blade Leading Edge, AIAA-2009-5104, in: Proc. of 45th AIAA/ASME/SAE&ASEE Joint Propulsion Conference, Aug. 2-5, Denver, CO, 2009.

[127] J.L. Rutledge, P.I. King, R. Rivir, Time Averaged Net Heat Flux Reduction for Unsteady Film Cooling, ASME J. of Eng. for Gas Turbines and Power, 132 (2010) 121901.

[128] L.A. El-Gabry, R.B. Rivir, Effect of Pulsed Film Cooling on Leading Edge Film Effectiveness, ASME J. of Turbomach. 134 (2012) 041005.

[129] S.V. Ekkad, S. Ou, R.B. Rivir, Effect of Jet Puslation and Duty Cycle on Film Cooling From a Single Jet on a Leading Edge Model, ASME J. of Turbomach. 128 (2006) 564-571.

[130] R.J. Volino, M.B. Ibrahim, Separation control on high lift low-pressure turbine airfoils using pulsed vortex generator jets, Applied Thermal Engineering (2011) doi:10.1016/j.applthermaleng.2011.08.028

[131] J.P. Bons, R. Sondergaard, R.B. Rivir, Turbine Seeration Control Using ulsed Vortex Generator Jets, ASME J. of Turbomach. 123 (2001) 198-206.

[132] N. Woods, I. Boxx, R. Sondergaard, M. McQuilling, M. Wolff, Investigation of Separation Control in Low Pressure Turbine Using Pulsed Vortex Generator Jets, AIAA-2006-4450, in: Proc. of 42nd AIAA/ASME/SAE/ASEE Joint Propulsion Conference and Exhibit, July 9-12, Sacramento, California, 2006

[133] Z. Mehrez, M. Bouterra, A. El Cafsi, A. Belghith, P. Le Quere, Mass Transfer Control Of A Backward-Facing Step Flow By Local Forcing-Effect Of Reynolds Number, Thermal Science, 15 (2011) 367-378.

[134] B.H. Saracoglu, P.G. Huang, G. Paniagua, Numerical Study of a Transonic Linear Cascade for Pulsating Trailing Edge Cooling Research, in: Proc. of 10th International Symposium on Experimental Computational Aerodynamics of Internal Flows, July 4-7, Brussels, Belgium, 2011.

[135] J.P. Gostelow, M.F. Platzer, W.E. Carscallen, On Vortex Formation in the Wake Flows of Transonic Turbine Blades and Oscillating Airfoils, ASME J. of Turbomach. 128 (2006) 528-535.

[136] C.H.K. Williamson, A. Roshko, Vortex Formation in the Wake of an Oscillating Cylinder, J. Fluids and Struct. 2 (1988) 355–381.

[137] W. Traupel, Thermische Turbomachinen. Springer Verlag, 1966

A

Uncertainty Analysis

A.1. Pressure measurements

The total pressure levels upstream of the cascade, coolant total and static pressure measurements were accomplished by using pneumatic pressure transducers with a range of ±1100mbar. The sensors provided a voltage level of almost 3 V at the ambient pressure (zero relative pressure) and 5 V at the maximum pressure. The voltage range in the data acquisition system was set to be ±5 V. For the calibration of the transducer, a digital handheld differential pressure indicator was used. The transducers were connected to a 12 bit acquisition system to avoid drifts and error in pressure readings which might be experienced with the multi-meters. Hence, the uncertainty in the voltage readings on ±5 V span was $\delta V=2.4\times10^{-3}$V. The uncertainty of the pressure indicator provided by the manufacturer was $\delta P=0.5$ mbar. The linear correlation between the membrane of the sensor due to the applied pressure and the voltage output is interpreted by Eq. A.1 where S is the sensitivity and O is the offset. The sensitivity is the increase of pressure which produces a change of 1V in sensor output voltage. At the end of the calibration procedure, the sensitivities for inlet total pressure, coolant total and static pressure sensors were calculated as S=548.4mbar/V, S=549.3mbar/V, S=547.5mbar/V, respectively.

$$P = S \cdot V + O \tag{A.1}$$

The uncertainty of pressure measurements can be calculated by using the expression given in Eq. A.2.

$$\delta \mathrm{P} = \left[\left(\frac{\partial P}{\partial S}\delta \mathrm{S}\right)^2 + \left(\frac{\partial P}{\partial V}\delta \mathrm{V}\right)^2 + \left(\frac{\partial P}{\partial O}\delta \mathrm{O}\right)^2\right]^{\frac{1}{2}}$$

$$= [V^2 \delta S^2 + S^2 \delta V^2 + \delta O^2]^{\frac{1}{2}} \tag{A.2}$$

The uncertainty of the sensitivity (δS) and the uncertainty of the offset (δO) should be estimated in order to calculate the uncertainty in pressure measurements. The uncertainty of sensitivity can be calculated by the equation below.

$$\delta S = \left[\left(\frac{1}{\Delta V} \delta(\Delta P) \right)^2 + \left(\frac{-\Delta P}{\Delta V^2} \delta(\Delta V) \right)^2 \right]^{\frac{1}{2}} \tag{A.3}$$

The corresponding values for the variables for Eq. A.3 in this case are $\Delta V=2V$, $\Delta P=1100mbar$ for the spans. The uncertainties of the voltage reading in the acquisition and the pressure reading from the calibrator are 4.8×10^{-3}V and 1 mbar, respectively. The estimated uncertainty of the sensitivity calculated as 1.411 mbar/V. Considering the uncertainty of the offset equals to the uncertainty of the pressure indicator and putting the maximum voltage of 5V into Eq. A.2, the uncertainty of the upstream total pressure, the coolant total and static pressure measurements were found to be $\delta P=7.19mbar$ in 95% confidence interval.

The static pressure measurements in the test section and downstream were performed by using a ScaniValve pressure scanner whose uncertainty is provided as 0.1 mbar by the manufacturer. Therefore, the uncertainty of all the other pressure measurements were assumed to be $\delta P=1$ mbar.

A.2. Temperature measurements

The variation in the inlet total temperature was measured by a thermocouple probe with 25µm junction size. The calibration of the thermocouples was made in an oil bath. The temperature of the bath was controlled by electronic circuit and measured by a mercury thermometer whose uncertainty was $\delta T_{mer}=0.1K$. As the relationship between the thermocouple voltage output and the temperature is also linear, the procedure used to calculate the uncertainty of total pressure measurements can be utilized for this analysis. The sensitivity was found to be 99.3 K/V by applying the calibration law.

$$T = S \cdot V + O \tag{A.4}$$

$$\delta T_{01} = \left[\left(\frac{\partial T}{\partial S} \delta S \right)^2 + \left(\frac{\partial T}{\partial V} \delta V \right)^2 + \left(\frac{\partial T}{\partial O} \delta O \right)^2 \right]^{\frac{1}{2}}$$

$$= [V^2 \delta S^2 + S^2 \delta V^2 + \delta O^2]^{\frac{1}{2}} \tag{A.5}$$

The uncertainty in the sensitivity was calculated in the same fashion of the pressure uncertainties. For this case, the variables in the sensitivity equation were taken as $\delta(\Delta T)$=0.2K and with ±5 V span, $\delta(\Delta V)$= 4.8x10^{-3}V. The maximum temperature and voltage drifts were ΔT=37K and ΔV=0.372V.

$$\delta S=\left[\left(\frac{1}{\Delta V}\delta(\Delta T)\right)^2+\left(\frac{-\Delta T}{\Delta V^2}\delta(\Delta V)\right)^2\right]^{\frac{1}{2}}=1.4\frac{K}{V} \tag{A.6}$$

The uncertainty of total temperature measurement was found as δT_{01}=0.95K (95% confidence interval) by plugging the offset uncertainty of 0.1K (the thermometer uncertainty) and the maximum voltage output of 0.59V in to Eq. A.5.

A.3. Pulsating valve rotational speed drift

The pulsating coolant generator is driven by a low-voltage DC engine, whose velocity is controlled increasing or decreasing the power supply voltage according to the requirements for each test. The unavailability of a feedback control unit might have led to important fluctuations on the rotational speed, affecting the investigated fluid dynamic phenomena. However, taking advantage of the rpm counter signal, it was possible to find out the severity of the problem. The rpm counter was provided by a ferromagnetic detector located in the front casing of the valve aligned with the holes. Every time a hole passes in front of the sensor a high level signal was generated and recorded by the acquisition system. The rotational speed was directly derived either counting the number of raising pulses of the signal during a determined period of time or calculating the FFT and locating the fundamental frequency.

Once the rpm signal has been recorded, a processing routine was used to compute the rotational speed drift in such a way that first, the raising edges of the signal were located in time and then the elapsed time between each pair was calculated. In order to separate the velocity drift and the error introduced by machining defects of the holes (due to small differences in size or shape), only one pulse out of four was considered, ensuring that always the same angular position was accounted for. Finally to compute the drift, the standard deviation of the resulting signal containing one value of velocity per revolution was compared to its mean. **Fig. A.1** shows the percentage speed drift at several velocities.

The fluctuation was found lower than 0.5%, sufficient to neglect its effects for the present application.

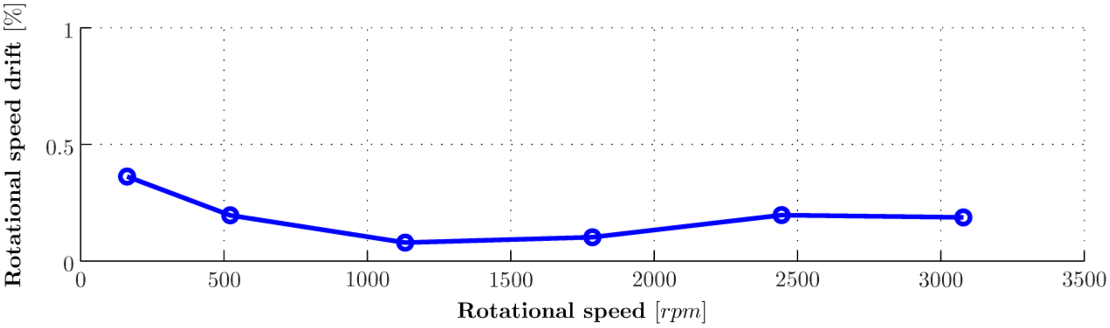

Fig. A.1. Rotational speed drift for tested pulsation frequencies

A.4. Uncertainty propagation

The measurements performed on the test section were used to calculate other flow variable like isentropic Mach numbers or pressure ratios. Under such circumstances, when two or more measured variables are used to calculate another derived value, the uncertainty of the measured quantities propagates through the calculation and creates a new uncertainty on the final value.

In current research, the uncertainty of the total and static pressure measurements propagated in to the uncertainty of isentropic Mach numbers, the base pressure to inlet total pressure and outlet static pressure to inlet total pressure ratios. In order to calculate the propagated uncertainty, the contribution of the uncertainty of two measured variables used to calculate Mach numbers should be considered. As depicted in the equation below, the calculation procedure is similar to the uncertainty of pressure and temperature measurements.

$$\delta \mathrm{M} = \left[\left(\frac{\partial M}{\partial \mathrm{P}_0}\delta \mathrm{P}_0\right)^2 + \left(\frac{\partial M}{\partial \mathrm{P}}\delta \mathrm{P}\right)^2\right]^{\frac{1}{2}} \tag{A.7}$$

The uncertainty in the Mach number was calculated over the range of total and static pressures observed in the experiments. The maximum calculated value (δM=0.5%) was assumed to be the propagated uncertainty in the Mach number. The same exercise was repeated to estimate the uncertainties of P_2/P_{01} and P_b/P_{01}. The uncertainties of both pressure ratios were found as 0.4%.